Alma Mater Studiorum · Università di Bologna

Scuola di Scienze
Corso di Laurea Magistrale in Fisica

Multicentre study for a robust protocol in single-voxel spectroscopy: quantification of MRS signals by time-domain fitting algorithms

Relatore:
Prof.ssa Paola Fantazzini

Presentata da:
Nicola Mordini

Correlatori:
Dott.ssa Paola Berardi
Dott.ssa Emma Fabbri

Sessione II
Anno Accademico 2013/2014

Questa tesi è dedicata a mio zio Renato.
Il tuo ricordo rimane impresso nel libro della mia memoria.

Abstract

La Spettroscopia di Risonanza Magnetica (MRS) è un'applicazione avanzata clinica e di ricerca che consente una specifica caratterizzazione biochimica e metabolica dei tessuti tramite l'identificazione e la quantificazione di metaboliti chiave per la diagnosi e la stadiazione della malattia.

L' "Associazione Italiana di Fisica Medica (AIFM)" ha promosso l'attivitá del gruppo di lavoro "Interconfronto di spettroscopia in RM". Lo scopo dello studio è il confronto e l'analisi dei risultati ottenuti dall'esecuzione di MRS su scanner di diversi ospedali per redigere un protocollo robusto per esami spettroscopici per la pratica clinica. Questa tesi s'inserisce nel progetto tramite l'utilizzo dello scanner GE Signa HDxt 1.5 T presso il Padiglione 11 dell'Ospedale S.Orsola-Malpighi di Bologna.

Le analisi degli spettri, acquisiti su due distinti fantocci, sono state eseguite con il pacchetto jMRUI, che offre una vasta gamma di algoritmi di preprocessing e quantificazione per l'analisi di segnali nel dominio del tempo. Dopo il controllo di qualitá con metodi standard e innovativi, sono stati acquisiti spettri con e senza soppressione dell'acqua sul fantoccio di prova GE. Il confronto fra i rapporti delle ampiezze dei metaboliti rispetto alla Creatina calcolati dal software della workstation, che opera sulle frequenze, e da jMRUI mostrano un buon accordo, suggerendo che le quantificazioni in entrambi i domini possano condurre a risultati consistenti.

La caratterizzazione di un secondo fantoccio, fornito dal gruppo di lavoro, ha raggiunto il proprio obiettivo, cioé la valutazione del contenuto della soluzione e delle concentrazioni dei metaboliti con buona accuratezza. La bontá della procedura sperimentale e dell'analisi dati è stata dimostrata dalla corretta stima del T_2 dell'acqua, dall'osservazione della curva di rilassamento biesponenziale della Creatina e dal corretto valore del TE in corrispondenza del quale la modulazione del J coupling causa l'inversione del doppietto del Lattato nello spettro.

Il lavoro di questa tesi ha dimostrato che è possibile eseguire misure e pianificare protocolli per l'analisi dati, basati sui principi NMR, che possano fornire valori robusti per i parametri dello spettro di uso clinico.

Abstract

Magnetic Resonance Spectroscopy (MRS) is an advanced clinical and research application which guarantees a specific biochemical and metabolic characterization of tissues by the detection and quantification of key metabolites for diagnosis and disease staging.

The "Associazione Italiana di Fisica Medica (AIFM)" has promoted the activity of the "Interconfronto di spettroscopia in RM" working group. The purpose of the study is to compare and analyze results obtained by perfoming MRS on scanners of different manufacturing in order to compile a robust protocol for spectroscopic examinations in clinical routines. This thesis takes part into this project by using the GE Signa HDxt 1.5 T at the Pavillion no. 11 of the S.Orsola-Malpighi hospital in Bologna.

The spectral analyses have been performed with the jMRUI package, which includes a wide range of preprocessing and quantification algorithms for signal analysis in the time domain. After the quality assurance on the scanner with standard and innovative methods, both spectra with and without suppression of the water peak have been acquired on the GE test phantom. The comparison of the ratios of the metabolite amplitudes over Creatine computed by the workstation software, which works on the frequencies, and jMRUI shows good agreement, suggesting that quantifications in both domains may lead to consistent results.

The characterization of an in-house phantom provided by the working group has achieved its goal of assessing the solution content and the metabolite concentrations with good accuracy. The goodness of the experimental procedure and data analysis has been demonstrated by the correct estimation of the T_2 of water, the observed biexponential relaxation curve of Creatine and the correct TE value at which the modulation by J coupling causes the Lactate doublet to be inverted in the spectrum.

The work of this thesis has demonstrated that it is possible to perform measurements and establish protocols for data analysis, based on the physical principles of NMR, which are able to provide robust values for the spectral parameters of clinical use.

Contents

List of Figures

List of Tables

Introduction

Magnetic Resonance Spectroscopy (MRS) is an advanced clinical and research application which guarantees a specific biochemical and metabolic characterization of tissues. Its usefulness has led to successful results in the examination of several pathologies in soft tissues, most notably in the brain, for which conventional Magnetic Resonance Imaging (MRI) is not sufficiently discriminating.

Basically, this technique is based on the chemical shift phenomenon: nuclei in different chemical environments experience shielding of the static magnetic field by the electron clouds of the neighbouring atoms. Consequently, these nuclei will exhibit different resonance frequencies, which can be identified by the peaks in the spectrum after the Fourier transform of the time-domain signal.

The clinical power of MRS is based on the detection and quantification of key metabolites for diagnosis and disease staging, e.g. Creatine, Choline, N-Acetyl Aspartate, myo-Inositol and Lactate. For example, the anomalous reduction of the N-Acetyl Aspartate peak in cortical areas is a marker for the Alzheimer's disease.

An important feature of this application is the possibility of analyzing spectra in well-defined areas in the tissues (especially in the brain), using MRI techniques. In particular, the single-voxel MRS technique applied in this work is able to acquire NMR signals from $10\times10\times10$ mm^3 to $30\times30\times30$ mm^3 volumes of interest. A special characteristic of the employed sequences is the possibility of analyzing the signal in the frequency domain, obtained after

the spatial localization.

The MR spectra acquired at static field strengths in clinical use require discerning observation of the detected peaks. Several experimental factors and physical phenomena contribute to the spectrum formation, making the correct identification of peaks in the spectrum more complicated.

The "Associazione Italiana di Fisica Medica (AIFM)" has promoted the activity of the "Interconfronto di spettroscopia in RM" working group, in which several Medical Physics units from Italian hospitals are involved. A participant is the Medical Physics unit of the S.Orsola-Malpighi hospital in Bologna. The purpose of the study is to compare and analyze results obtained by perfoming MRS on scanners of different manufacturing in order to compile a robust and accurate protocol for spectroscopic examinations in clinical routines. This research aims to establish the experimental conditions which ensure the most accurate, unbiased and artifact-free spectra as achievable to allow the clinician to formulate an efficient diagnosis.

This thesis takes part into this project by using the GE Signa HDxt 1.5 T at the Pavillion no. 11 of the S.Orsola-Malpighi hospital in Bologna. The experiments have been carried out on the GE MRS test phantom and on an in-house phantom provided by the AIFM group, whose content has been determined by dedicated spectroscopic acquisitions. These phantoms contain different concentrations (already known in the GE MRS test phantom, not known in the in-house phantom) of metabolites that are markers of specific brain pathologies. The results of these measurements will be included in a database in which measurements from all the other units will come together.

The spectral analyses have been performed with the jMRUI package. This software includes a wide range of preprocessing and quantification algorithms for signal analysis in the time domain. The most renowned method for spectral quantification is the integration of the area below the peak of interest in the frequency domain. This approach is prone to inaccurate results because of the difficulty of disentangling the peaks from the noise baseline. On the contrary, quantification of MRS data in the time domain leads to better

results in terms of preprocessing and fitting of signal components by directly analyzing the acquired NMR signal.

This thesis is organized as follows. The first chapter introduces the physical basis of MRS: the phenomena which take part into the spectrum formation and the specific pulse sequences applied for signal acquisition are described. The second chapter discusses the clinical applications of MRS in medicine and their diagnostic added value. In the third one, the characteristics of the experimental acquisition system are presented.

The fourth chapter focuses on the results of the analysis of the spectroscopic quality assurance on the MR scanner, evaluated by standard and advanced methods. The fifth chapter discusses the time-domain algorithms which have been used for spectral quantification. In the sixth chapter, the results of the quantification of parameters of interest in non-water-suppressed spectra of the GE phantom are reported. The seventh lists the quantification results of the analyses of metabolite spectra in the GE test phantom. The eighth chapter discusses the experimental trials for the characterization of the in-house phantom content.

Chapter 1

Magnetic Resonance Spectroscopy

1.1 The physical basis

1.1.1 A brief history

Nuclear Magnetic Resonance (NMR) is a physical phenomenon in which a nucleus with a non-zero spin placed in a magnetic field B_0 absorbs and emits electromagnetic radiation. This phenomenon, which is quantum in nature, occurs if the nucleus is submitted to a radio frequency (RF) field B_1 with a characteristic frequency depending both on the strength of the magnetic field B_0 and the nature of the nucleus. Since its discovery in 1946 by Bloch and Purcell (Nobel Prize in 1952), this phenomenon has led to several applications which are still relevant nowadays, the most famous of which is the possibility to acquire tomographic images of human body (Magnetic Resonance Imaging, MRI).

One of these applications is Magnetic Resonance Spectroscopy (MRS), which is capable of determining the physical, chemical, electronic and structural properties of the atoms and the molecules in which they are contained. Thanks to the studies of Richard Ernst (Nobel Prize in 1991), who con-

tributed to the development of high-resolution NMR spectroscopy, this technique has become relevant in chemistry and biochemistry for the analysis of the properties of organic molecules of interest and retrieve structural information.

The first MRS experiments in biology were carried out on cell cultures and micro-organisms. Later on, researches were conducted on test animals in laboratory to retrieve information on tissues. More recently, MR Spectroscopy has proven its usefulness in medicine to offer valuable information about living tissues and their metabolism for diagnosis and prognosis of several pathologies (often as a complementary adjunct to MRI). Nowadays MRS (or better "In vivo MRS") has become a clinical method to assess the alterations in neurodegenerative diseases [1] and metabolic functions of organs such as muscles or heart.

1.1.2 The Larmor resonance frequency

According to the physical principles of NMR, each nucleus at a particular magnetic field intensity absorbs and emits electromagnetic radiation at the typical **Larmor resonance frequency** ν_0:

$$\nu_0 = \frac{\gamma}{2\pi} B_0 \tag{1.1}$$

where γ is the magnetogyric ratio, which is typical of the nuclear isotope under investigation, and B_0 is the applied magnetic field. Thus, the corresponding pulsation ω_0 is:

$$\omega_0 = \gamma B_0 \tag{1.2}$$

In NMR research field it is customary to refer to the pulsation ω_0 as the "Larmor frequency", therefore this expression will be used at times in this thesis when there is no ambiguity. In Table 1.1 the Larmor frequencies ν_0 of different nuclear isotopes used in MR Spectroscopy at various values of B_0 are given.

Applied field	$\mathbf{B_0 = 1T}$	$\mathbf{B_0 = 1.5T}$	$\mathbf{B_0 = 3T}$
Isotopic species	$\nu_\mathbf{0}$**(MHz)**		
${}^{1}_{1}H$	42.58	63.87	127.74
${}^{2}_{1}H$	6.54	9.81	19.62
${}^{13}_{6}C$	10.71	16.07	32.13
${}^{19}_{9}F$	40.08	60.12	120.24
${}^{31}_{15}P$	17.25	25.88	51.75

Table 1.1: Larmor frequencies of different isotopes at various values of B_0.

It is important to mention that, given B_0, the nuclei with the higher intensity in the resonance frequency also provide the more intense NMR signal. Indeed, the advantages of using higher field strength are a linear increase in the signal-to-noise ratio (SNR) and better separation of peaks in the spectrum. More specifically, in clinical applications the most interesting nuclei are ${}^{1}_{1}$H, ${}^{13}_{6}$C and ${}^{31}_{15}$P:

- ${}^{1}_{1}$H-MRS is the more diffuse type of investigation, especially in brain spectroscopy, mostly because of the natural abundance of protons both in the human body ($\sim$ 62 %) and in organic compounds and also because the proton is the most NMR-sensitive nucleus [2].

- ${}^{13}_{1}$C-MRS is interesting in the study of the carbon-containing compound metabolism (e.g. carbohydrates), even though it occurs at a low average abundance (1,1 %) in relation to the major isotope ${}^{12}_{1}$C, which has a null spin value and therefore is NMR-inactive.

- ${}^{31}_{15}$P-MRS is important in the analysis of Adenosine TriPhosphate (ATP) functions and other energetically important metabolites, especially in muscles, and has a moderate NMR-sensitivity.

1.1.3 Chemical shift

Indeed, if all the protons in a mixture of molecules resonated at the same Larmor frequency, magnetic resonance spectra would be limited to a single peak centred on that particular frequency value. However, the resonance frequency is highly dependent on the surrounding chemical environment, which is locally variable. In fact, the electronic cloud has a shielding effect on the nucleus, since electrons generate a secondary induced magnetic field which opposes the external field B_0. This is because electrons rotate about B_0 in the opposite sense to nucleus spin precession and consequently their magnetic moment μ_e is aligned against B_0, as Figure 1.1 illustrates.

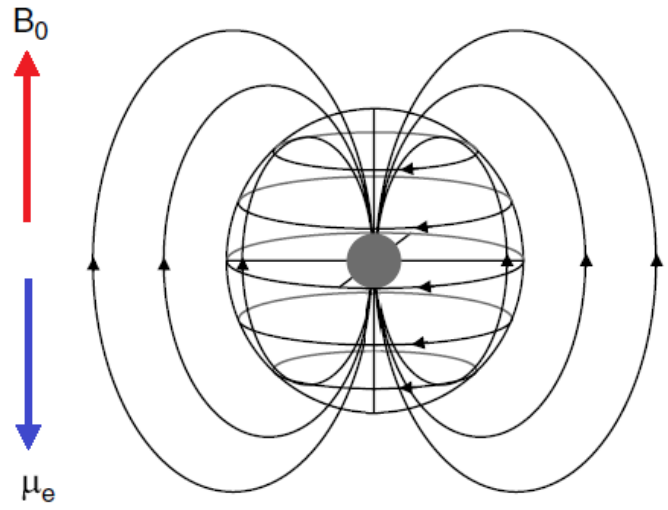

Figure 1.1: Electron shielding of the nucleus.

Therefore, the outcome is that the nucleus senses a magnetic field B_0 with reduced intensity because of the shielding given by the electronic cloud. This behaviour, called "**chemical shift**", is expressed as:

$$B_{eff} = B_0(1 - \sigma) \tag{1.3}$$

where B_{eff} is the effective field, B_0 is the applied field and σ is a dimensionless

number ($\sigma < 1$), shielding or screening constant, which is dependent on the chemical environment of the nucleus and its relative position within the molecule. Typical values for σ are 10^{-5} for protons and 10^{-2} for heavier nuclei. Thus, the frequency at which the nucleus resonates becomes:

$$\nu_{eff} = \frac{\gamma}{2\pi} B_0(1 - \sigma) \tag{1.4}$$

As the equation above indicates, the Larmor precession frequency of the nucleus under investigation is slightly displaced. The outcome of the reduction of the magnetic field strength sensed by the nucleus is that the energy difference ΔE of two adjacent Zeeman levels is reduced. Thus, the photon energy required for a transition is lower than in absence of chemical shift.

$$\Delta E = -\hbar\gamma B_{eff} \tag{1.5}$$

Different effective magnetic field will lead to different energies required for the nucleus to flip between Zeeman levels.

It should be outlined that each atom contained in the molecule influences to a certain extent the sensed shielding because it contributes to the overall electronic density. For instance, if the molecule contains one or more **electronegative atoms** (e.g. Nitrogen, Oxygen, Fluorine, Clorine), the electrons will be pulled away from atoms with less electronegativity (e.g. Hydrogen). Therefore, this resulting electron withdrawal will make the protons deshielded. This phenomenon occurs in molecules in which covalent bonds between atomic electrons are established. A graphical representation can be viewed in Figure 1.2.

The electronegativity of oxygen in the acetaldehyde molecule is such intense that it attracts much of the electron cloud. Therefore, protons closer to oxygen are unshielded, while the more distant ones are more shielded [3].

It is common practice not to express chemical shifts in Hertz units since this choice would make chemical shifts dependent on the applied magnetic field strength. Therefore, chemical shift δ are conventionally expressed in

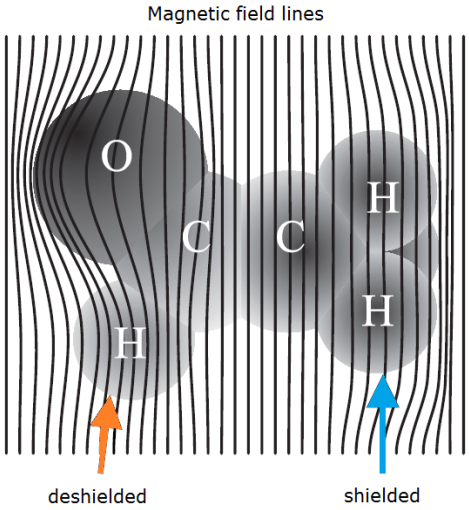

Figure 1.2: Different shielding in the acetaldehyde molecule.

terms of ppm in function of the displacement from the frequency of a **reference compound** ν_{ref} measured by the spectrometer [4].

$$\delta(\text{ppm}) = \frac{\nu - \nu_{ref}}{\nu_{ref}} \cdot 10^6 \tag{1.6}$$

Indeed, the reference compound should be chemically inert and the position of its chemical shift should not fluctuate remarkably because of external variables such as temperature and should produce an evident resonance peak well separated from the other ones. The reference compound is conventionally assigned a 0.00 ppm chemical shift δ. For in vivo applications, compounds whose concentrations do not vary significantly in pathological patients are used. Commonly used reference compounds for different investigations are given in Table 1.2. It is important to underline that in vivo $^1_1$H-MRS does not make use of tetramethylsilane, $(CH_3)_4Si$, because of its toxicity.

1.1.4 J coupling

A common phenomenon which is observed in spectroscopic analysis is the splitting of resonance peaks into several smaller peaks. This is due to an effect

${}^{A}_{Z}X - MRS$	**Reference compound**
${}^{1}_{1}H - MRS$	tetramethylsilane (TMS)
in vivo ${}^{1}_{1}H - MRS$	creatine (Cr) CH_3 peak of N-acetyl aspartate (NAA) water
${}^{13}_{6}C - MRS$	tetramethylsilane (TMS)
in vivo ${}^{31}_{15}P - MRS$	phosphocreatine (PCr) ATP

Table 1.2: Reference compounds for different MRS investigations.

called "**J coupling**" (or "spin-spin coupling"). The interactions of magnetic moments of the nuclei can occur through space (dipolar coupling) or indirectly through electron shared in chemical bonds (scalar coupling). Indeed, even though dipolar interactions between nuclei are important for the relaxation process in liquids, there is no net contribution to the spectrum thanks to the rapid molecular tumbling which averages these interactions to zero [2]. Meanwhile, overall scalar coupling interactions are not null since they do not depend on the relative distance of the nuclei, but on the intramolecular distance. Therefore, the nearest chemical groups strongly determine the peak displacement observed in the spectrum.

J coupling is established between nuclei with magnetic moments both parallel or antiparallel to the magnetic field and can be homonuclear or heteronuclear [5]. In addition, scalar coupling is an intramolecular phenomenon since it requires a molecular orbital as a medium for interaction [6]. This characteristic can be exploited to identify the molecular species and their covalent structure.

The hyperfine interaction between nuclear and electron spins is governed by the Fermi contact, which energetically favours an antiparallel spin orientation. Meanwhile, the Pauli exclusion principle implies that electron spins in the molecular orbital are antiparallel, forcing nuclear and electron spins in

an energetically higher orientation. The relative orientation of spins under J coupling is represented in Figure 1.3.

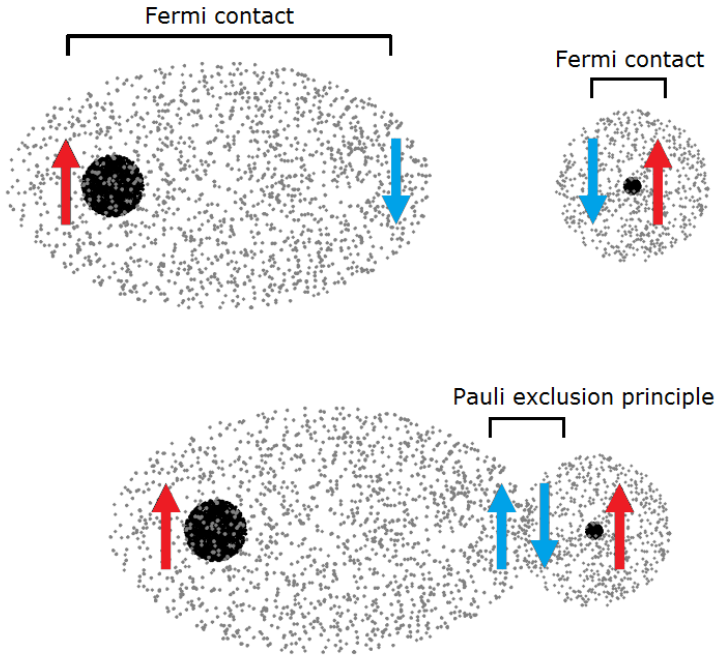

Figure 1.3: Rearrangement of nuclear and electronic spins through J coupling.

As Figure 1.3 displays, one of the two electron spins is parallel to the nuclear spins because of Pauli exclusion principle. This setting leads to an energetically less favourable state.

Because of scalar coupling, a new term must be added to the spin-spin hamiltonian H_0, H_{scalar}:

$$H = H_0 + H_{scalar} = H_0 + 2\pi J \mathbf{I_1} \cdot \mathbf{I_2} \tag{1.7}$$

where J is the coupling constant, which is independent on the applied magnetic field and is proportional to the proximity of the coupled nuclei. This is an especially interesting feature at high-field MRS since J-coupled multiplets will stay at the same separation, but displaying them in a ppm scale they

will appear closer, thus leading to a more accurate discrimination from the other compounds. Furthermore, the intensity of scalar coupling constants rapidly decrease as the number of bonds increases and can be negligible for more than four bounds [2]. Coupling constant values for chemical bonds commonly found in biomolecules studied in MRS are listed in Table 1.3 [2].

Chemical bond	**Coupling constant (Hz)**
${}^{1}_{1}\mathrm{H} - {}^{1}_{1}\mathrm{H}$	1 - 15
${}^{1}_{1}\mathrm{H} - {}^{13}_{6}\mathrm{C}$	100 - 200
${}^{1}_{1}\mathrm{H} - {}^{31}_{15}\mathrm{P}$	10 - 20
${}^{13}_{6}\mathrm{C} - {}^{13}_{6}\mathrm{C}$	30 - 80
${}^{31}_{15}\mathrm{P} - {}^{16}_{8}\mathrm{O} - {}^{31}_{15}\mathrm{P}$	15 - 20

Table 1.3: Scalar coupling constant values for different chemical bonds.

Taking into account spin-half nuclei for which there are a low energy spin-up state α ($m = +\frac{1}{2}$) and a high energy spin-down state β ($m = -\frac{1}{2}$), the spin-spin coupling gives rise to four energy levels ($\alpha\alpha$, $\alpha\beta$, $\beta\alpha$, $\beta\beta$) [7]. The expressions for energies (listed in Table 1.4) depend on the effective resonance frequencies of both nuclei ($\omega_{eff,1}$, $\omega_{eff,2}$) and the correspondent coupling constant $J_{1,2}$.

Spin state	$\mathbf{\lvert m1, m2 \rangle}$	**Energy**
$\alpha\alpha$	$\lvert +\frac{1}{2}, +\frac{1}{2} \rangle$	$(-\frac{1}{2}\omega_{eff,1} - \frac{1}{2}\omega_{eff,2} + \frac{1}{4}J_{1,2})\hbar$
$\alpha\beta$	$\lvert +\frac{1}{2}, -\frac{1}{2} \rangle$	$(-\frac{1}{2}\omega_{eff,1} + \frac{1}{2}\omega_{eff,2} - \frac{1}{4}J_{1,2})\hbar$
$\beta\alpha$	$\lvert -\frac{1}{2}, +\frac{1}{2} \rangle$	$(+\frac{1}{2}\omega_{eff,1} - \frac{1}{2}\omega_{eff,2} - \frac{1}{4}J_{1,2})\hbar$
$\beta\beta$	$\lvert -\frac{1}{2}, -\frac{1}{2} \rangle$	$(+\frac{1}{2}\omega_{eff,1} + \frac{1}{2}\omega_{eff,2} + \frac{1}{4}J_{1,2})\hbar$

Table 1.4: Energies for a two coupled spin system.

The spectrum of two coupled spins $1, 2$ is composed of two doublets each split by the same amount, $J_{1,2}$, centred at the chemical shift frequencies of both spins, as Figure 1.4 illustrates.

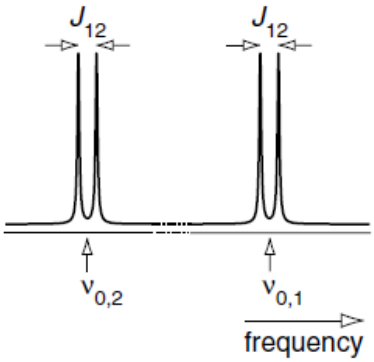

Figure 1.4: Resonance peaks of two coupled spins.

The spectrum shown in Figure 1.4 is a first-order spectrum, which correspond to a spin system with $|\nu_2 - \nu_1| \gg J_{1,2}$ and is considered a weakly coupled spin system. On the other hand, when $|\nu_2 - \nu_1| \sim J_{1,2}$, the system is strongly coupled, i.e. the $\alpha\beta$ and $\beta\alpha$ states become mixed, and the result is a second-order spectrum. The appearance of the peaks is commonly referred to as the "**roof effect**", which is common in multiplets belonging to the same molecule [7]. This behaviour is represented in Figure 1.5. The inner lines are higher, while the outer are shorter. When the two Larmor frequencies are identical, there is only one peak in the spectrum located at that frequency.

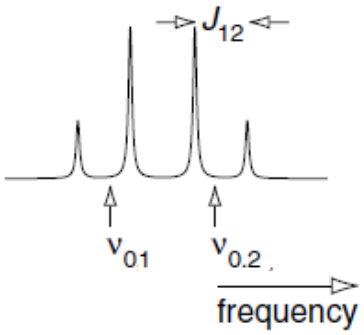

Figure 1.5: Roof effect in strongly-coupled spins.

For nuclei with $I > \frac{1}{2}$ the description becomes more complex and higher

rank terms must be taken into account. For instance, the deuteron has $I = 1$, thus a triplet centred on the effective resonance frequency will be observed in its spectrum.

1.1.5 Nuclear Overhauser effect

According to NMR theory, the strength of a signal is highly dependent on the difference in the Boltzmann level populations. After a perturbating pulse, the magnetization returns back to alignment with B_0 through T_1 relaxation, in which nuclei make transitions to reestablish the equilibrium. In uncoupled spins it may occur that an increase in the signal is observed thanks to a polarization transfer from one nuclear spin population to another saturated one via cross-relaxation. This is known as the "**nuclear Overhauser effect**" (nOe). This phenomenon is established through intramolecular dipolar interactions in space, not through chemical bonds as in spin-spin coupling. Therefore, nOe depends on:

- the nature of the nuclei
- the distance between nuclei (the proximity favours dipolar interactions)
- the correlation time τ_C, i.e. the time between two relative consecutive orientations of the dipoles (if it is too long, other effects, such as intermolecular dipolar interactions, will hinder intramolecular dipolar alignment)

Taking into account two uncoupled nuclei A and X with significant dipolar interaction, there will be four possible combinations of energy levels (Figure 1.6), with $\alpha\alpha$ corresponding to both nuclei in their ground state, $\alpha\beta$ and $\beta\alpha$ representing the cases of only one nucleus in the excited state and $\beta\beta$ being both nuclei in the excited states.

Assuming that $\alpha\beta$ and $\beta\alpha$ are equally populated, at the equilibrium $\beta\beta$ is less populated than $\alpha\alpha$. If the equilibrium population is altered, the system tends to restore it through relaxation whether by $\beta\beta \rightarrow \alpha\alpha$ transition, which

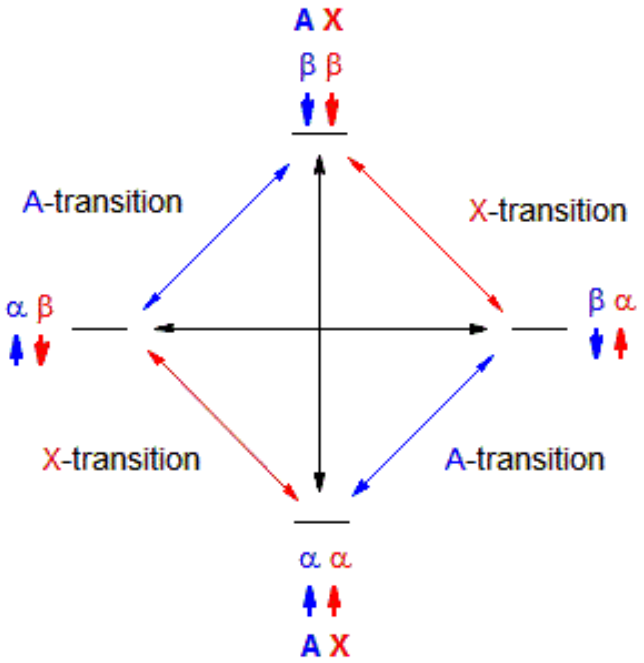

Figure 1.6: Energetic level and transition diagram for two uncoupled spins exhibiting nuclear Overhauser effect.

determines a positive nOe for nucleus A (NMR signal enhancement), or by $\beta\beta \rightarrow \beta\alpha$, which implies a negative nOe (NMR signal reduction).

The outcome of positive nOe is an observed increase in the peak amplitudes in the spectrum depending on the magnetogyric ratios of nuclei, as expressed the following formula, which is valid for short τ_C:

$$\eta = \frac{\gamma_X}{2\gamma_A} \tag{1.8}$$

where η is the nuclear Overhauser enhancement. This represents a gain factor in the peak amplitude. Values for η under usual in vivo MRS nuclei are reported in Table 1.5 [8].

A-X	η
$^{13}C - {}^{1}H$	$1.3 - 2.9$
$^{31}P - {}^{1}H$	$1.4 - 1.8$

Table 1.5: Values for nuclear Overhauser enhancement for typical in vivo MRS nuclei.

1.1.6 Spectrum formation

As it was previously mentioned, in NMR spectroscopy the nuclei do not resonate at the same frequency. Therefore, it is impossible to be on resonance with all the lines in the spectrum since the RF pulse frequency ω_{RF} slightly differs from the Larmor frequency of the nucleus ω_0.

$$\omega_{RF} \neq \omega_0 \tag{1.9}$$

This mismatch implies that the perturbed magnetization in the rotating frame preceeds both around the RF magnetic field B_1 and an apparent magnetic field B_{app} resulting from the imperfect resonance.

$$B_{app} = B_0 - \frac{\omega_{RF}}{\gamma} \tag{1.10}$$

The combination of these two precessions implies that the nuclear spin rotates around an effective field B_{eff}, as Figure 1.7 displays.

To a certain extent, if the amplitude of B_1 is greater than B_{app}, we can assume that the nuclei are on resonance to a first approximation. Therefore, the size of B_1 should be as great as the transmitting power of the coils permits. Such transmitted pulses are referred to as "**hard pulses**" and they determine bandwidths up to hundred of kHz. The allowed frequency window is important in MRS because it determines the range of detectable compounds.

In NMR investigations the signal coming from the nuclear magnetization can be detected by perturbating the spin population in the Boltzmann en-

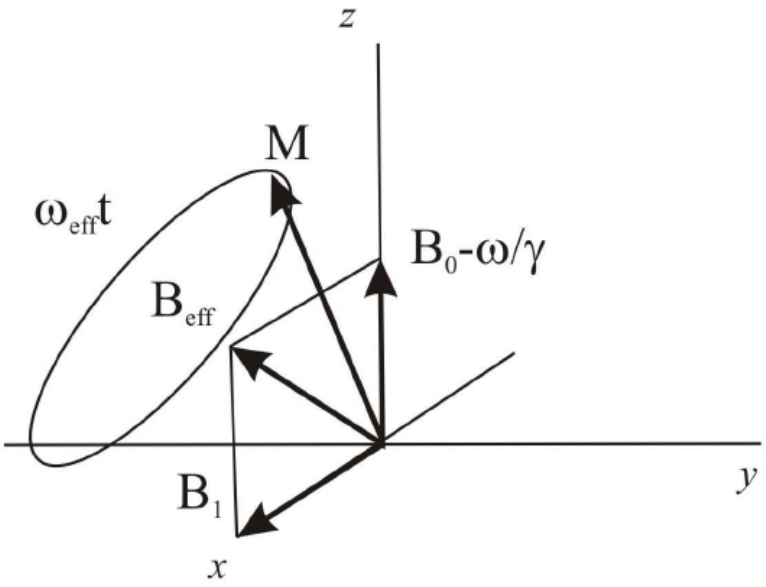

Figure 1.7: Precession of magnetization in the rotating frame when the RF pulse is off-resonant.

ergy level distribution. By applying a 90° excitation RF pulse orthogonal to B_0, the magnetization vector flips onto the transverse plane. Following the pulse, the spin precession on the transverse plane induces an oscillatory electromotive force in the receiving coil by electromagnetic induction, originating thus an induced current in the probe. The detected signal is called "**Free induction decay**" (FID), which has an oscillating and exponentially decaying trend, as in Figure 1.8 [9], and it is originated by the photons in the radio-wave range emitted by the nuclei returning to the equilibrium.

$$M_{xy}(t) = M_{xy}(0)e^{-\frac{t}{T_2^*}} \tag{1.11}$$

The components of the magnetization are:

$$\begin{cases} M_x(t) = M_0 \cos[(\omega_0 - \omega)t + \phi]e^{-\frac{t}{T_2^*}} \\ M_y(t) = M_0 \sin[(\omega_0 - \omega)t + \phi]e^{-\frac{t}{T_2^*}} \end{cases} \tag{1.12}$$

In the expressions above the decay is enhanced by T_2^*, which leads to a faster

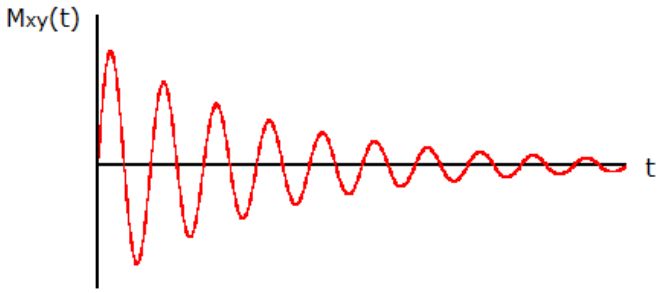

Figure 1.8: Free induction decay following an excitation pulse.

transverse relaxation because of the inhomogeneities of the magnetic field and to a multi-exponential decay. The detected signal $s(t)$ is proportional to the magnetization.

$$s(t) = s_0 e^{i\phi} e^{i\omega t} e^{-\frac{t}{T_2^*}} \tag{1.13}$$

This signal in the time domain can be represented in the frequency domain through **Fourier transform**. The returning FID is a composite signal of many different contributions from metabolites in the volume of interest (VOI), which is resolved into individual resonance frequencies and their relative amplitudes by the Fourier transform.

$$F(\omega) = \int_{-\infty}^{+\infty} s(t) e^{-i\omega t} dt \tag{1.14}$$

It is possible to gain a spectrum from one of the two components of the FID, but it is customary to measure both (quadrature detection) to be able to discriminate between positive and negative frequencies in relation to the reference compound. The real and imaginary components of the Fourier transform are:

$$\begin{cases} R(\omega) = A(\omega)\cos\phi - D(\omega)\sin\phi \\ I(\omega) = A(\omega)\sin\phi + D(\omega)\cos\phi \end{cases} \tag{1.15}$$

where

$$\begin{cases} A(\omega) = \frac{M_0 T_2^*}{1+(\omega_0-\omega)^2 T_2^{*2}} \\ D(\omega) = \frac{M_0(\omega_0-\omega) T_2^{*2}}{1+(\omega_0-\omega)^2 T_2^{*2}} \end{cases} \tag{1.16}$$

$A(\omega)$ and $D(\omega)$ are the absorption and the dispersion components respectively. $A(\omega)$ is characterized by a **Lorentzian lineshape** (Figure 1.9). whose

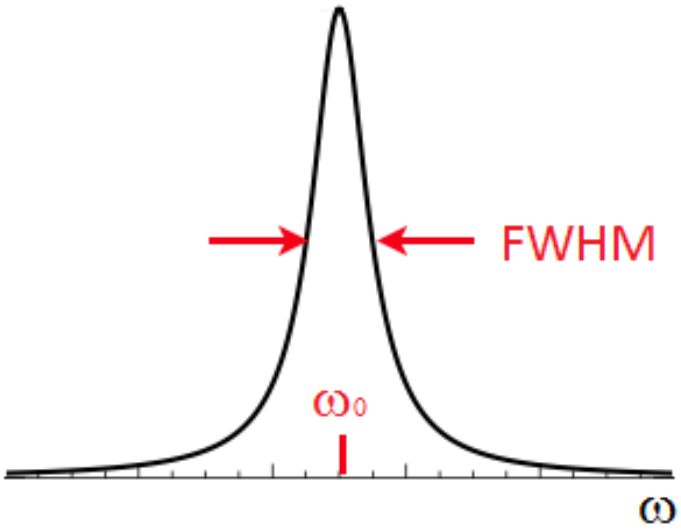

Figure 1.9: Lorentzian lineshape in the frequency domain.

full width at half maximum (FWHM) is:

$$FWHM = \frac{1}{\pi T_2^*} \tag{1.17}$$

where

$$\frac{1}{T_2^*} = \frac{1}{T_2} + \gamma \Delta B_0 \tag{1.18}$$

ΔB_0 represents the local field inhomogeneity.

Considering the FWHM of the Lorentzian, it is deducible that the shorter the T_2^* is (i.e. the faster the decay of the FID), the broader the distribution is. This is a major drawback if low-quality scanners with inhomogeneous field are used, where T_2^* is considerably short [5]. The area Σ under the peak (with height h_{peak}) is:

$$\Sigma = \frac{\pi}{2} FWHM \cdot h_{peak} \tag{1.19}$$

The area is proportional to the concentration of the substance resonating at that particular frequency under unsaturated conditions. Since the area under a peak is constant for a given number of nuclei, the peak height decreases with increasing FWHM [3]. Furthermore, if the size of the signal in the time domain increases, the height of the lorentzian curve will be boosted proportionally too. Consequently, it is possible to assess the relative number of nuclei contributing to the signal formation [7].

Actually, a single peak will be observed only in a sample with the same nuclei resonating at the same Larmor frequency. It is more common to notice several peaks in the spectrum. Frequencies which are higher than the value of the reference resonance peak (down-field) are on the left side, whereas lower frequencies (up-field) are on the right, as in Figure 1.10. This convention is due to the fact that more unshielded nuclei give resonance lines at the beginning of the scan. It is customary practice to express the frequencies in ppm or Hertz units and peak heights in arbitrary units. The spectrum and the covalent structure of Lactate, $C_3H_6O_3$, are given in Figure 1.10 as an example.

The electronic shielding becomes more prominent reading the spectrum from left to right coherently with the reduction of both the sensed magnetic field and the resonance frequency. In fact, the methine peak ($-$CH) is centred on a higher frequency (4.10 ppm) because of the deshielding of the corresponding proton by oxygen atoms, while the three methyl proton peak ($-CH_3$) is located at a lower frequency value (1.31 ppm).

In addition, it should be mentioned that the acquisition of the FID inevitably records noise in conjunction with the signal from nuclei. This disturbance comes from the electronics in the spectrometer, but the major contribution is due to thermal noise from the detection coil. At the beginning of the acquisition the signal strength is strongest, but it progressively gets weaker until it is mistakable with noise. To reduce the amount of noise that is

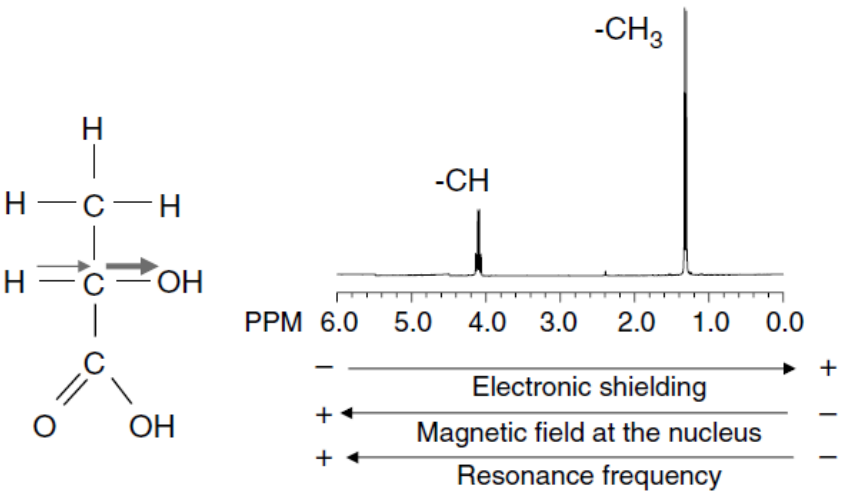

Figure 1.10: Spectrum and covalent structure of Lactate.

present in the signal, the FID is multiplied by a weighting function $w_{SNR}(t)$ that decreases exponentially with time, suppresses the long tail of the signal curve (where the noise in more intense in relation to the signal) and causes the signal to decay more faster:

$$w_{SNR}(t) = e^{-\alpha t} \tag{1.20}$$

where α is a sortable constant value which determines the strength of the decay. As it is displayed in Figure 1.11, the multiplication of the signal for a weighting function evidently reduces the amount of noise both in the acquired FID and the relative spectrum (avoiding an abrupt truncation of the signal, which would lead to artefacts in the spectrum), by almost doubling the signal-to-noise ratio (S/N).

Furthermore, it is common practice to convert the Lorentzian lineshape of peaks to a Gaussian one through the multiplication of the signal for a further weighting function. This method makes peaks more narrow and enhances resolution, as it can be seen in Figure 1.12.

$$w_{LG}(t) = e^{\beta_L t} e^{-\beta_G t^2} \tag{1.21}$$

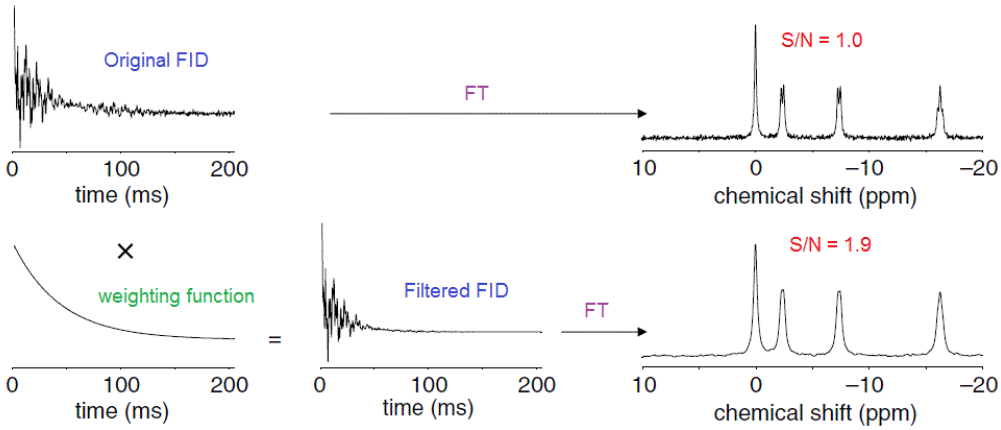

Figure 1.11: Filtering of the FID through weighting function for noise reduction.

where β_L and β_G are constants required for the lineshape conversion.

However, since resolution enhancement generally results in an increase of noise in a spectrum because of the contribution of the rising exponential [10], optimal outcomes are a compromise which is reached by multiplying the FID with both weighting functions. This overall procedure is called "**apodization**" and it is essential in MRS to prevent the spectrum from being too noisy and to enhance the resolution.

$$s'(t) = s(t)e^{-\alpha t}e^{\beta_L t}e^{-\beta_G t^2} \tag{1.22}$$

The FID processing must be preceeded first by a digitization procedure through an Analog-to-Digital Converter (ADC) to enable data to be analyzed and stored in a computer memory. The digitization process samples the signal as a sequence of samples at regular intervals. According to Nyquist-Shannon theorem, in order to avoid aliasing effects, the sampling rate $\nu_{sampling}$ must be at least twice as intense as the higher frequency contained in the analog signal as the following expression indicates:

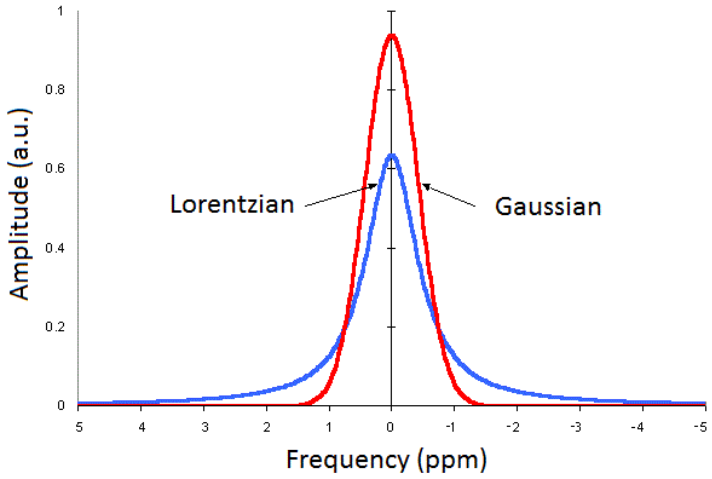

Figure 1.12: Lorentzian and Gaussian resonance lines of equal FWHM and integrated amplitude.

$$\nu_{sampling} = \frac{1}{\Delta t} > 2\nu_{max} \tag{1.23}$$

where Δt is the sampling interval. Consequently, the spectral resolution $\Delta\nu$ is given by:

$$\Delta\nu = \frac{1}{T_{acquistion}} = \frac{1}{N\Delta t} \tag{1.24}$$

It is clear that an increase in the acquisition time will lead to a better spectral resolution, although this implies extended data storage and more relative noise. It is customary to lengthen the acquisition time by adding a series of zero amplitude samples after the decay of the FID before applying the Fourier transform. Such a procedure is called "**zero filling**" [11].

1.2 Magnetic field gradients in MRI and MRS

1.2.1 Field gradients in MRI

The versatility of NMR tecniques is reflected in the enormous variety of sequences and parameters that are adjustable to retrieve different information extracted from the detected signal. Generally, both MRI and MRS sequences consist of applications of RF pulses with or without field gradients which have specific durations and timings [12]. Indeed, different types of sequences are characterized by two timing values, echo time TE, which is the time between the 90° RF pulse and NMR signal sampling, corresponding to maximum amplitude of echo, and repetition time TR, i.e. the time between two consecutive 90° RF excitations pulses, whose duration influences the percentage of longitudinal magnetization recovery.

The signals acquired through MRI scans from each pixel in the image are processed with the aim of discriminating the intrinsic nuclear relaxation properties at different locations in body tissues. This difference in relaxation times leads to different signal intensities, which is explicited in a wide range of contrast in the images, especially in soft tissues. In a simplified expression, the **subjective contrast** C_s between two points in a T_2-weighted image is determined by the difference in the transverse relaxation times and the echo time TE used in the sequence [13].

$$C_s \propto 1 - e^{-\frac{TE}{T_2' - T_2''}} \tag{1.25}$$

Another important feature in MRI is **space-encoding**. The main purpose is to make the resonance frequency ω_0 position-dependent such that after Fourier transformation different frequencies correspond to different space positions rather than different chemical shift values. This procedure makes use of **field gradients** by specially designed coils:

- slice-selective gradients applied along z-axis (at the centre of the bore of the magnet) in concomitance with the RF excitation pulses. Each z position is characterized by a specific resonance frequency $\omega_0(z)$.

$$\omega_0(z) = \gamma(B_z(0) + G_z z) \tag{1.26}$$

Therefore, the corrisponding z position is:

$$z = \frac{\omega_0(z) - \gamma B_z(0)}{\gamma G_z} \tag{1.27}$$

Only a selected range of frequencies $\Delta\omega$ (i.e. positions Δz) are excited by the RF pulse, as Figure 1.13 displays.

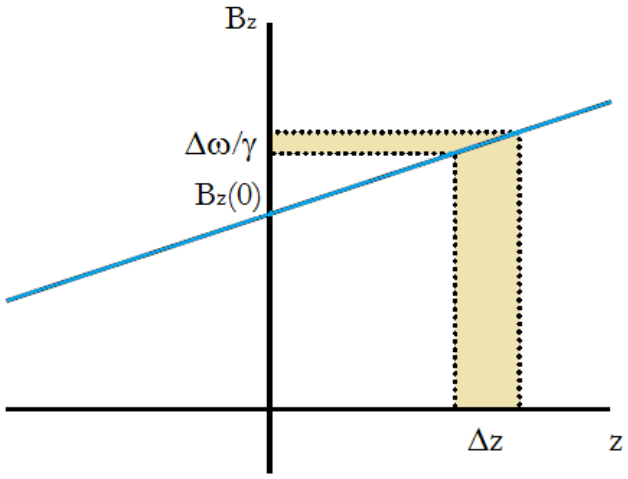

Figure 1.13: Position and frequency ranges excited through slice-selective gradient.

- frequency or read gradients make spins along x-axis resonate ad different frequencies
- phase gradients make spins along y-axis acquire different phases

The latter two gradients are the basis for k-space sampling, which allows the transformation of the selected slice into a raster grid, in which spins belonging to different matrix elements differ whether in frequency or in phase. Mansfield introduced the concept of the space vectors k_x and k_y, which allow to move through k-space either by varying time or gradient amplitude [14]:

$$\begin{cases} k_x = \gamma G_x t \\ k_y = \gamma G_y t \end{cases} \tag{1.28}$$

The signal from each location in the mapping relative to a slice with thickness $2a$ is dependent on the space vector:

$$s(k_x, k_y) = \int_{-a}^{a} [\int \int \rho(x, y, z) e^{i(k_x x + k_y y)} dx dy] dz \tag{1.29}$$

The **field of view** (FOV) in both directions is determined by the gradient intensity and the sampling time (contained in the expressions for space vectors).

$$\begin{cases} FOV_x = \frac{2\pi}{\gamma G_x t} \\ FOV_y = \frac{2\pi}{\gamma G_y t} \end{cases} \tag{1.30}$$

However, the space-encoding procedure basically erases the chemical shift information of nuclei since the spin frequencies are modulated by the gradients (possible residual chemical shifts would be interpreted as noise artifacts), therefore it is not included in the spectroscopic sequences themselves. Indeed, gradients are used in MRS with different purposes.

1.2.2 Field gradients in MRS

The main concerns in MRS are the acquisition of the spectrum with a lineshape as well-resolved and not distorted as it can be achieved and the spatial assignment of the detected signal which is generally accomplished through a MRI acquisition prior to the MRS sequence. Actually, there are two types of localization procedures (single- or multi-voxel techniques), which will be discussed in detail in later sections.

Spectroscopic sequences generally use **slice-selective RF pulses** with orthogonal field gradients in order to define the volume of interest from the intersection of the excited slices, thus restricting the signal detection to a specific region (**spatial localization**).

In addition, MRS sequences make use of field gradients as a means to suppress unwanted signals and to guarantee a more homogeneous field in the area of interest. These are called "**crusher** or **spoiler gradients**", which dephase the transverse component of the magnetization such that coherences and consequently the signal are cancelled. However, the effects of gradients can be partially reversed by the application of a subsequent gradient which undoes the dephasing. Since dephasing proceeds at a different rate for different spins, gradient pulses of different strengths and durations are applied to restore most of the overall coherence.

The outcome of the switch of gradients during the MRS acquisition is a net enhancement in spatial resolution. These matters are of the utmost importance for in vivo characterizations, since they allow an accurate examination of a tissue of interest without the signal contamination from other tissues.

Ideal **magnetic field homogeneity** is a condition which is difficult to achieve since the static field is inherently nonuniform because of design constraints of the magnet. However, it is considered a fundamental parameter to assess the quality of the magnet in use and is more crucial in spectroscopic rather than imaging investigations since poor field homogeneity results in both a lower SNR and broadening of the width of the peaks. Frequently the inhomogeneity ι of two systems (often expressed in ppm units) is estimated by measuring the ratio of the maximum fluctuation measured in a specific spherical volume (e.g. corresponding to the volume of a dedicated spherical phantom) and the nominal value of the static field.

$$\iota(\text{ppm}) = \frac{\Delta B_0}{B_0} \cdot 10^6 \tag{1.31}$$

Indeed, a fundamental preliminary procedure in MRS is **shimming**, which is the adjustment of field gradients to optimize the magnetic homogeneity over the volume of interest (VOI). This is accomplished through regulation of currents in dedicated gradient coils. Fluctuations in the magnetic field cause line broadening and distortions in the spectrum together with

reduced SNR. In particular, this procedure becomes more relevant at higher fields where good local shimming prevents peaks from overlapping, in spite of the increase in sensitivity. Indeed, a major problem in high-field MRS is that T_2^* relaxation times become shorter because of the greater magnetic susceptibilities, especially when sequences are applied in vivo [15]. When a magnetic field is applied, small magnetic field gradients are originated between tissue interfaces with different values of susceptibility. These local gradients enhance the dephasing between spins, thus degrading the spectral resolution. This setback is reduced thanks to improved shimming systems [16].

Furthermore, the field homogeneity is also needed to reduce signal contaminations from the surroundings, a problem known as "**voxel bleed**" [12]. This effect is due to displacements in the slice selection for compounds with different relative chemical shifts or imperfect slice-selective pulses. In addition, the excited VOI should be as sharp as possible in the edges. It is common practice to perform an imaging sequence prior to the spectrum acquisition in order to correctly identify the VOI. Figure 1.14 depicts the relative displacement of the fat and water voxels.

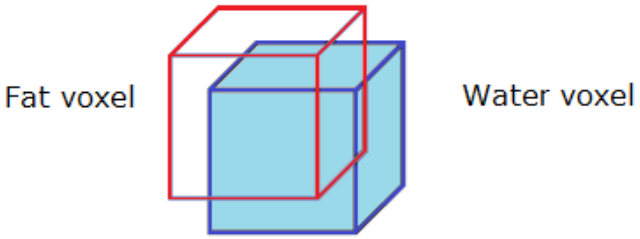

Figure 1.14: Fat voxel offset location with respect to the water voxel.

Another matter of concern is represented by **eddy currents** $i_{eddy}(t)$ which are induced in the magnet by the variation of the magnetic flux of fluctuating fields (e.g. switching on gradient pulses), as Faraday's law states:

$$i_{eddy}(t) = -\frac{1}{R}\frac{\partial\Phi(B_{eddy})}{\partial t} \tag{1.32}$$

where R is the electrical resistance of the medium and $\Phi(B_{eddy})$ is the magnetic flux.

Since these parasite currents cause further distortions in the peak shapes and signal dephasing and they can last for hundreds of milliseconds, it is essential that electronic hardware is unaffected by low levels of eddy currents especially when sequences with short TEs are applied [17]. This is due to the fact that eddy currents with time constants comparable to echo times are difficult to differentiate from the actual signal currents [18].

The reduction of these effects is achieved by applying corrective currents in the gradient coils whose amplitudes and decay characteristics are set in order to offset the eddy currents [19] by a phase factor $\Delta\phi(r)$. For instance, after a 90° pulse followed by a gradient the phase of these currents must be adjusted according to the amplitude of the gradient and the echo time. Another technological advance is represented by **shielded gradient coils**, which do not produce significant magnetic fields outside the sample volume and minimize the generation of eddy currents. They are composed of an inner main coil and an outer shield coil connected in series together with cooling cladding. The outer coil produces a field which opposes the one from the inner coil with such amplitude that net field outside the coils (fringe field), which creates disturbances and is useless for experiments, is almost null, leading to reduced effects of eddy currents [20].

$$\Delta\phi(r) \propto \gamma[B_0 + G(t)r]TE \tag{1.33}$$

In conclusion, it should be mentioned that the introduction of many field gradients into the spectroscopic sequences inevitably determines a delay between the application of RF pulses and the signal recording by the receiver. This is the reason why sequence developers aim to reach a balance between sequence timing values and the expected outcomes.

1.3 Single-volume localization sequences

1.3.1 Selective pulses and relaxation times

All single-volume localization sequences consist essentially of the selection of a spatially selective slice by the application of frequency-selective RF pulses in conjunction with B_0 magnetic field gradients. The final outcome is the investigation of the signal from one volume at a time [21]. Usually the VOI is defined by the intersection of three orthogonal slices selected by three applied RF pulses, as represented in Figure 1.15. For instance, a typical VOI size for brain spectroscopy is 8 cm^3.

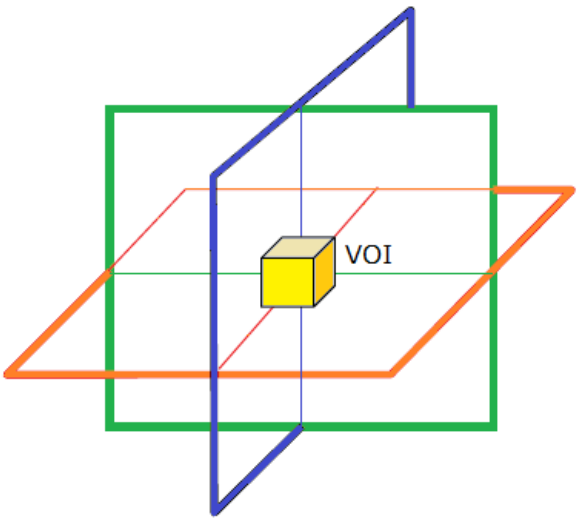

Figure 1.15: Defined VOI from intersection of the three slice-selective RF pulses applied in orthogonal directions.

The contribution of magnetization from spins outside the VOI must be suppressed as efficiently as possible by using pulses with good excitation profile and crusher gradients. There are several combinations of RF pulses and fields gradients which may be chosen to select a 3D volume. The VOI is previously selected through a MRI scan ("image-guided spectroscopy"). Anyway, it is important to be aware that the results of the application of

different sequences lead to different parameters in the spectra, therefore a critical spectral analysis requires an accurate discussion of the most commonly used acquisition methods (ISIS, STEAM and PRESS).

Furthermore, it is worth to mention that MRS sequences must avoid influences of relaxation times on signal intensity. This is because the NMR signal is proportional to concentrations only if T_1 saturation and T_2 decay effects are negligible [3]. To avoid T_1 saturation of the compounds of interest, the repetition time for the acquisition should be 5 times greater than the longitudinal relaxation time. However, for clinical purposes scans are repeated after:

$$TR > 3T_1 \tag{1.34}$$

In clinical studies shorter TR values are commonly used in practice and partial saturation is consented not to increase the total acquisition time (especially in clinical routines). Effects due to T_2 relaxation are more evident if long-TE sequences are used, nevertheless short-TE sequences have become more diffuse.

1.3.2 ISIS

The ISIS sequence (Image Selected In vivo Spectroscopy) leads to a complete 3D volume localization in eight scans [22]. Basically, it consists of three frequency-selective on/off 180° pulses in concomitance with three orthogonal magnetic field gradients, followed by a 90° pulse, which originates the acquired FID. The pulse sequence for ISIS is depicted in Figure 1.16.

After zero or an even number of 180° pulses, the magnetization ends up along the positive longitudinal axis and flips onto the positive y axis thanks to a 90° pulse, whereas after an odd number of 180° pulses, the magnetization is aligned with the negative longitudinal axis and is excited to the negative y axis by a 90° pulse [2]. Inversion 180° pulses are switched on or off depending on the current acquisition scan S_i $(i = 1, ...8)$, as represented in Table 1.6.

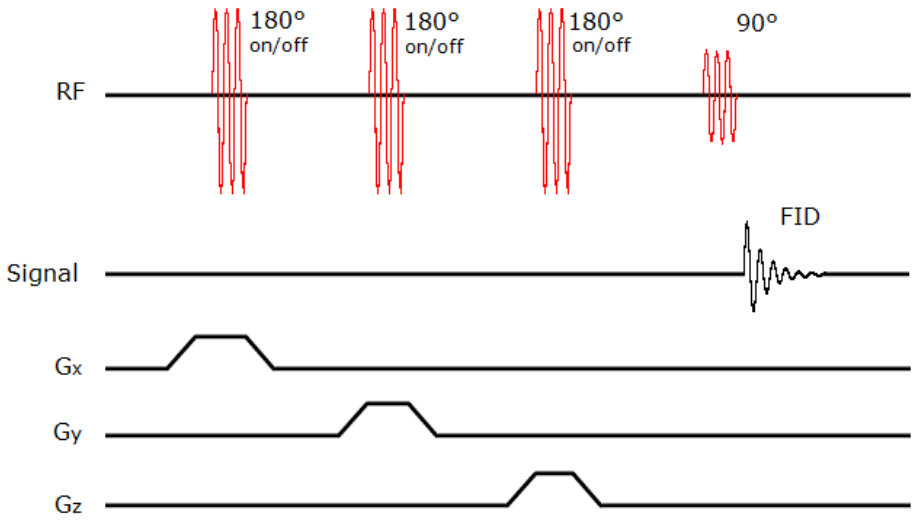

Figure 1.16: Pulse sequence for ISIS.

The volume selection is based on the sum and subtraction of the scans S_i to accumulate the signal in the desired VOI and erase the signal coming from other locations.

$$S_{VOI} = S_1 - S_2 - S_3 + S_4 - S_5 + S_6 + S_7 - S_8 \tag{1.35}$$

However, ISIS is a sequence whose accuracy is poor because it is highly sensitive to movements of the sample under investigation, which may lead to displacements of the VOI and thus artifacts due to signal contamination. The algebraic operations on the acquired scan would lead to systematic errors. In addition, the more inhomogeneous the magnetic field is, the lower the signal intensity is. Although ISIS is frequently used in the investigations of short T_2 species, transverse relaxation during 180° pulse may cause further degradation in the localization. Therefore, an accurate shimming is difficult because of the number of scans.

Another major setback in ISIS is the so-called "**T_1 smearing**", which causes further signal loss. This inconvenience occurs when the longitudinal relaxation is incomplete between two of the eight subsequent scans [23]. The

Scan	1st 180° pulse	2nd 180° pulse	3rd 180° pulse
S_1	off	off	off
S_2	on	off	on
S_3	off	on	off
S_4	on	on	off
S_5	off	off	on
S_6	on	off	on
S_7	off	on	on
S_8	on	on	on

Table 1.6: Switching of the inversion pulses in ISIS scans.

amplitude of the longitudinal magnetization is progressively reduced as the scans are acquired and the cancellation of the unwanted signals is incomplete. T_1 smearing is dependent on the field inhomogeneity and the repetion time duration relative to T_1 relaxation time. However, T_1 smearing can be contained if signal averaging of each individual ISIS scan is performed.

1.3.3 STEAM

STEAM (STimulated Echo Acquisition Mode) is a single-shot localization sequence. The basic pulse sequence (Figure 1.17) consists of three 90° RF pulses together with field gradients, a combination which originates three FIDs, four spin echoes (SE) and a stimulated echo (STE), which is the one that is recorded. Since only 90° pulses, which have shorter duration than 180° pulses, are applied in this sequence, STEAM is the first choice when short TEs are needed. Short TEs (< 40 ms) permit a reduced signal loss and therefore high SNR, which allows the observation of some peaks that would not be detected at longer TEs, but on the other hand the noise is enhanced too.

A new parameter is introduced into the STEAM sequence, the mixing

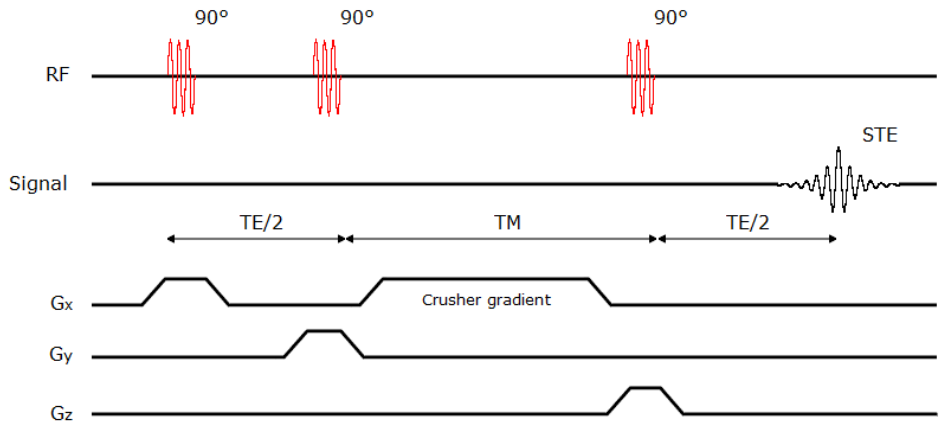

Figure 1.17: Pulse sequence for STEAM.

time (TM), a period during which magnetization transfer between the spin system is allowed through nOe cross-relaxation. As it can be viewed in Figure 1.17, the stimulated echo is formed after a TE + TM delay (or after TE/2 following the last 90° pulse). During TE period the magnetization is mainly affected by T_2 relaxation, whereas T_1 relaxation is prevailing in the TM period. Indeed, since the magnetization is not influenced by T_2 relaxation during TM, STEAM is frequently used for the analysis of species with short T_2 values and relatively long T_1 values.

It is important that STE be successfully isolated from SEs and FIDs. This is accomplished in two ways:

- phase cycling, i.e. the phases of the pulses and the receiver are systematically varied in order to cancel unwanted signals. This procedure is generally avoided since it requires to be applied iteratively, although STEAM is a single-scan method. However it can be used if scans are repeated to increase SNR.

- switch of crusher field gradients for a short period of time to dephase FIDs and SEs. This choice does not require repetition.

The amplitude of the stimulated echo is:

$$M_{xy} = \frac{1}{2} M_0 \sin\theta_1 \sin\theta_2 \sin\theta_3 e^{-\frac{TM}{T_1}} e^{-\frac{TE}{T_2}} e^{-\frac{16}{\pi^2}\gamma^2 G^2 \delta^2 (\Delta - \frac{\delta}{4}) D} \tag{1.36}$$

where θ_i $(i = 1, 2, 3)$ represents the nutation angle of RF pulse i, G is the amplitude of the gradient, Δ is the delay between two gradients in the two TE/2 periods, δ is their duration and D is the diffusion coefficient. As the equation above indicates, the amplitude of a STE is expected to be half of the equilibrium magnetization M_0, notwithstanding relaxation and diffusion effects. This is because the second 90° pulse only rotates half of the trasverse magnetization to the longitudinal plane, while the other one is dephased by a crusher gradient switched during TM duration. Consequently, this method implies a decreased SNR by a factor of 2 in relation to equilibrium magnetization (and PRESS sequence too, as it will be discussed in the following section) [5].

Actually, diffusion processes are disadvantageous for MRS investigations because if spins are given too much time between RF pulses, there will be an evident decrease in the amplitude of the magnetization and the SNR will drop. Therefore, echo times shorter than 30 ms are generally preferred in clinical STEAM. Even TE values from 1 to 6 ms have been used in research studies with faster excitation pulses and crusher gradients at ultra-high fields [24], even though there is incomplete magnetization recovery and overlapping of peaks is more pronounced [1].

1.3.4 PRESS

PRESS (Point RESolved Spectroscopy) is a single-scan sequence primarily composed of a 90° pulse followed by two refocusing 180° pulses, as represented in Figure 1.18. Therefore, the method is characterized by the formation of two spin echoes. The 90° pulse selects the plane of interest. Following the first 180° pulse the first echo forms after a delay TE_1 and contains signal from a column resulting from the intersection of two planes selected by both the 90°and the 180° pulses. The successive refocusing occurs during a delay

TE_2, such that the final echo forms at the following echo time:

$$TE = TE_1 + TE_2 \tag{1.37}$$

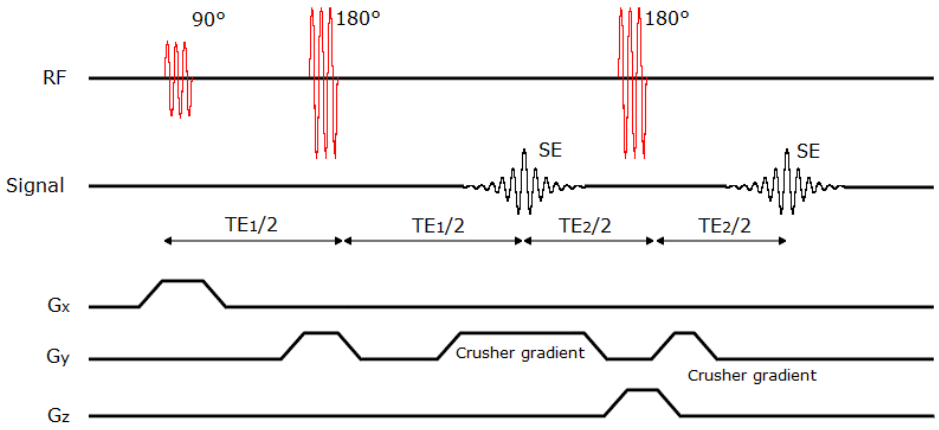

Figure 1.18: Pulse sequence for PRESS.

This echo only contains signal from the intersection of the three selected planes, i.e. precisely the volume of interest, depicted in Figure 1.19. Indeed, signal from outside the VOI is not excited and rapidly dephased by crusher gradients. Even the first echo needs to be dephased for the acquisition to be successful. If outer signal is recorded, this disturbance is due to incomplete removal of coherences, magnetic field inhomogeneities or partial suppression of other prevailing signals, as it will be discussed in the following section. All these matters of concern influence the spectral quality.

More scan accumulations are needed in order to gain a sufficient SNR (ordinarily 8 or 16 are sufficient) and reduce possible artifacts by sum of the detected signals. However, it should be stressed that PRESS is characterized by a SNR value approximately higher than STEAM by a factor of 2. This is the reason why PRESS is the most frequently used localization technique. Anyway, STEAM is a preferable sequence choice when short TEs are needed since PRESS requires inevitably longer TE values because of the longer duration of the 180° pulses [21]. When the first MRS scanners were

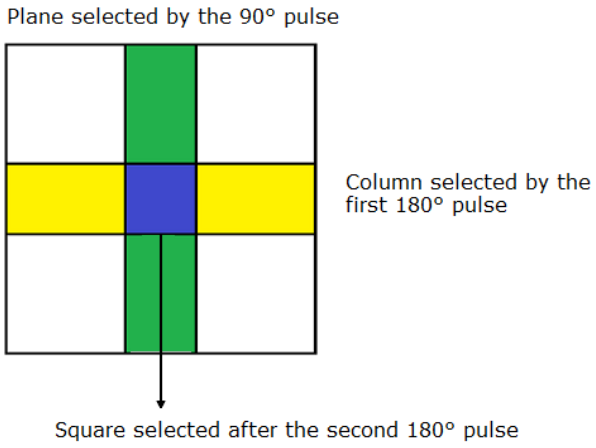

Figure 1.19: Spatial localization by PRESS pulses.

developed, the lower boundary for TEs in PRESS was 144 ms, but nowadays it is possible to reach even values of about 30 ms [12].

In addition, PRESS tends to underestimate T_2 values of some molecules, especially if long TEs are used [25]. This effect is due to J coupling interactions which accelerate the signal decay and enhance spin dephasing. The consequent outcome is the broadening of the spectral peaks. STEAM seems to be more insensitive to this drawback because of the shorter TEs, although it is affected anyway by such effect [26].

1.3.5 Imperfect RF pulses

The ideal result of any localization technique would be a perfectly sharp edge of the excited VOI, since it is evidence of high localization accuracy and volume definition. Anyway, it is a more realistic assumption that the selected VOI will be slightly smeared because of the finite length of the applied pulses. Each RF pulses is characterized by its **excitation profile**, i.e. its Fourier transform, which also includes a transition frequency range in which the flip angle between 0° and 90° or 180° of the magnetization is included. This

inherent imperfection in the applied pulses causes smoothness in the edge profile and contamination from the outer areas.

The application of STEAM leads to a more definite volume profile than PRESS because 90° pulses are generally produced with a sharper excitation profile. Therefore, STEAM is recommended for brain MRS applications where contamination from surroundings is to be avoided [21].

1.3.6 Signal suppression methods

Some compounds such as water and fat are found in greater abundance than others in human tissues and consequently the proton MRS spectrum is dominated by the higher signals originated by hydrogens contained in these molecules. Generally, the concentrations of metabolites are lower than those of water by more than 4 orders of magnitude. Typical metabolites concentrations are in the millimolar range ($1 - 10$mM), while water molar concentration is in the order of tens of molar concentrations [27]. The latest electronic acquisition systems are able to record the low metabolite peaks despite the greater amplitude of the water resonance. Anyway, the presence of such an overshot peak in the acquired spectrum might lead to baseline distortions and contaminated signals compromising a reliable detection of metabolite [28].

To overcome this difficulty and remove baseline alterations, suppression of water and/or fat signals is frequently performed. The removal of particular resonances in the spectrum is only allowed if the compound that is interfering with the detection possesses a property which discerns it from the other molecules (whether it may be chemical shift, scalar coupling, or T_1 or T_2 relaxation times). An additional benefit from the signal suppression is the reduction of the dynamic range, i.e. the ratio between the largest and smallest signal values that must be processed by the electronic systems, since the difference of the highest and the lowest NMR signal detected by the receiver is smaller. Anyway, this is not an overriding concern with recent electronic hardware.

Currently, several water suppression techniques have been developed, all of which are highly sensitive to T_1 recovery, which partially degrades their performance:

- **frequency selective excitation techniques** make use of RF selective pulses and crusher gradients in combination with the localization pulse sequence. The most renowned method is CHESS (CHEmical Shift Selective), which is composed of a 90° pulse followed by a spoiler gradient which dephases the excited magnetization, as Figure 1.20 depicts.

  CHESS is performed prior to the selected localization pulse sequence,

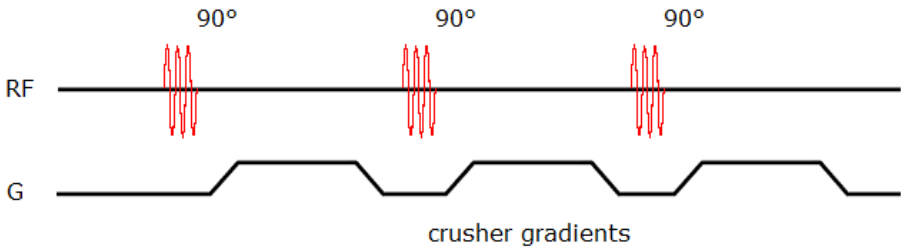

Figure 1.20: CHESS water suppression sequence repeated three times.

since metabolite resonances are left unperturbed. This method must be applied as close as possible to the Larmor resonance frequency of water to be successful. However, since some T_1 relaxation occurs between the suppression pulse and the localization sequence a flip angle slightly greater than 90° is needed.

The delay between CHESS and the excitation of metabolites should be as short as possible in order to avoid water signal recovery by T_1 relaxation. Field inhomogeneity is the major drawback since it might lead to imperfect suppression of water signal because of the broadening of the water resonance. Therefore, CHESS needs good spectral resolution, which is achieved through proper shimming. It is usual that CHESS is repeated three or more times prior to the sequence to improve water suppression. This iterative procedure reduces the sensitivity to

magnetic field inhomogeneity because the suppressed frequency range around the water resonance is broadened, thus removing possible residual magnetization. Additionally, it is essential that the flip angles are equal in each repetition to avoid further residual magnetization.

- **relaxation based methods** exploit the difference in the relaxation times between water and metabolites. They lead to an incomplete water suppression because the discrepacy in the relaxation times for water and metabolites may be too small to allow a successful discrimination and also because relation times of water in human tissues are highly variable.
  An example among such suppression techniques is WEFT (Water Eliminated Fourier Transform), which is similar to an IR (Inversion Recovery) sequence, as depicted in Figure 1.21. Following a 180° pulse, which

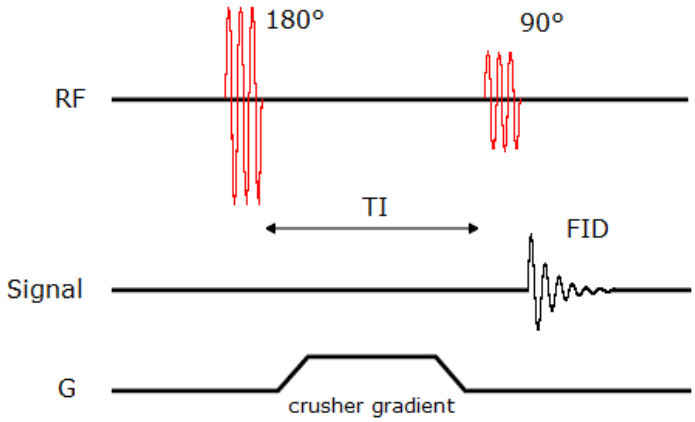

Figure 1.21: Pulse sequence for WEFT.

inverts the magnetization, a field gradient is switched on during a delay time called inversion time TI to dephase transverse magnetization. After the inversion time, a 90° pulse is applied with the aim of bringing the magnetization onto the transverse plane where it is detected by a RF coil. The TI value is chosen so that the water magnetization

has recovered to its null point (represented in Figure 1.22), while the metabolite one has only partially recovered.

$$M_{water}(TI) = M_0(1 - 2e^{-\frac{TI}{T_{1,water}}}) = 0 \tag{1.38}$$

with

$$TI = T_{1,water} \ln 2 \tag{1.39}$$

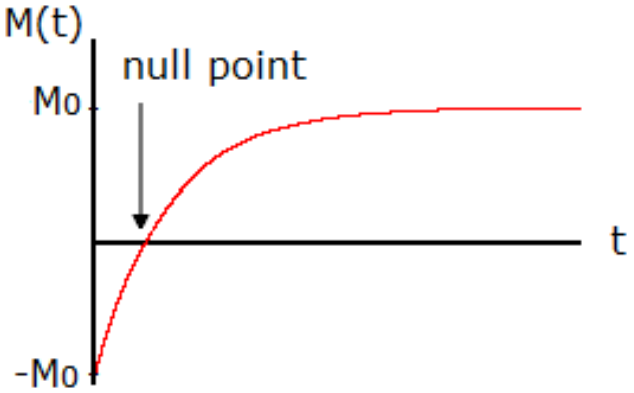

Figure 1.22: Null point for water magnetization after the application of a 180° pulse.

Actually, in order to allow the complete recovery of the magnetization the repetition time TR between consecutive scans should be chosen to be:

$$TR \simeq 5T_{1,water} \tag{1.40}$$

This choice would imply excessively long measurement times, hence shorter values are frequently used in clinical examinations.

1.3.7 Non-water-suppressed MRS

MRS acquisition do not necessarily need a prior signal suppression performance. Indeed, imperfect water suppression might lead to evident distortions in the acquired spectra, especially for resonances close to the water peak. For instance, detection of the water resonance may be useful for the following purposes:

- internal concentration referencing (bearing in mind that water concentrations are highly fluctuating for in vivo examination depending on the pathologies).

- evaluation and subsequent correction of possible magnetic field fluctuations.

- correction of eddy current effects and baseline artifacts.

In water-suppressed MRS, the selected bandwidth for water suppression must be narrow, a requirement which demands high field homogeneity. The measurement of the water signal is needed as a quantitative phase reference. Although the water signal is typically prevalent over the one of metabolite, anyway modern digital receivers are able to evaluate and process this difference in the dynamic range [29]. The problem is that the set gain of the amplification devices needs to be lowered, thus determining a reduced SNR value for metabolites [28].

Non-water-suppressed MRS provides initial estimate of the resonance frequency and linewidth for spectral fitting purposes. Furthermore, it is useful as a normalization reference to remove fluctuations due to field inhomogeneity in iterative scans [28].

1.4 Chemical shift imaging

1.4.1 Multi-voxel techniques

Localization techniques only allow the detection of signal from a single volume. The main disadvantage of this approach is that no signal is acquired from the surrounding areas of interest, which might lead to miss relevant information. Chemical shift imaging (CSI), or Magnetic Resonance Spectroscopic Imaging (MRSI), is a multi-voxel advanced application of MRS which allows the measurement of metabolite information in extended regions simultaneously and the addition of chemical analysis of body tissues to MRI investigations.

CSI makes use of the space-encoding to form a grid in the acquired image. The spectroscopic information is evaluated in a defined matrix of areas of interest, since the relative spectra are recorded at each phase-encoding step. The outcome is an accurate mapping of chemical shifts. CSI can be performed in two or three dimensions, although usually 3D examinations are avoided because of the excessively long scan times in relation to clinical necessities.

Phase encoding gradients are applied in MRSI to encode spatial information. Combined with k-space sampling, STEAM or PRESS are performed to acquire spectra from multiple voxels in the areas of interest. It is common practice to display **metabolic maps** of concentrations of biochemical compounds superposed on the image in gray-scale colours.

Excitation by spectroscopic sequences is restricted to the region of interest in the field of view to optimize:

- the achievable field homogeneity, which facilitates signal suppression from outer regions
- acquisition times
- containment of contamination from strong signals nearby, which leads to chemical shift displacement and distorted metabolite ratios [21].

It is important to mention that the spatial resolution Δi is determined by the FOV and the number of phase-encoding steps N_i, where i = x, y, z.

$$\Delta i = \frac{FOV_i}{N_i} \tag{1.41}$$

Consequently, the dimensions of the voxels excited by localization sequences must be consistent with the spatial resolution of the imaging scan.

1.4.2 Comparison of single-voxel and CSI techniques

Single-voxel techniques are widely diffuse in clinical examinations because they exhibit desirable advantages in relation to CSI. Meanwhile, these methods possess great limitations:

- impossibility to determine the spatial heterogeneity of spectral patterns (MRSI allows an overall evaluation of chemical content).
- only a short number of VOIs can be examined in the duration of a clinical exam.
- voxel sizes tend to be relatively large with no information regarding the spatial distribution of metabolites or the regional variations [30].

The reasons why single-voxel acquisitions (SVA) may be prefable to MRSI are the following:

- shorter acquisition times. The total scan time T_{scan} in 3D-MRSI is:

$$T_{scan} = TR \cdot N_x N_y N_z \cdot N_{avg} \tag{1.42}$$

  where N_i (i = x, y, z) are the number of phase-encoding increments and N_{avg} are the number of averages. Scan times can be shortened by using reduced FOVs and hence smaller N_is, for a given spatial resolution. Anyway, it is evident that the acquisition times become longer than in SVA [2].

- better SNR values. MRSI is characterized by poorer SNR since extremely long scan times are not acceptable in clinical examinations and the shortening of T_{scan} (especially by reducing N_{avg}) leads to the reduction of SNR.

- easier to process because of the smaller amount of data to analyze (MRSI is computationally more demanding).

- they provide optimal field homogeneity since shimming is focused and optimized on a particular VOI. In fact, in MRSI it is more difficult to shim properly an entire slice with the aim of gaining as well-resolved spectra as in SVA in each voxel in the matrix [31].

- VOI is affected by minimal contamination thanks to the optimal voxel selection and shimming. This make the detection of metabolites more accurate and reliable.

- they can be performed at shorter TEs, while MRSI is usually performed at longer TEs since field homogeneity is less stringent because there are less overlapping resonances [21].

- spectra are characterized by better spectral resolution and water suppression. In MRSI residual field inhomogeneities across the field of view may cause imperfect water suppression, thus degrading the quality of the spectra.

Therefore, MRSI seems like a more suitable option when the analysis of more VOIs is required or the biochemical content in extensive tissues needs to be thoroughly characterized, since it does not permit the detection of the same high quality spectra as SVA [5].

Chapter 2

MRS applications in diagnostic medicine

2.1 MRS clinical studies

2.1.1 Diagnostic utility of MRS

MRS is an advanced clinical study to reveal physiological fluctuations in several diseases and monitor the progression of pathologies. This in vivo diagnostic technique allows to retrieve reliable and accurate metabolic and histopathological information related to the tissues under examination. Indeed MRS is valuable and determining in cases when conventional MRI and the clinical history of the patient are not sufficient to formulate a diagnosis.

The biochemical information content provided by spectra depends on the echo time, the type of pulse sequence and the field strength, all factors which influence the detectability of compounds. For instance, some peaks will be more prominent than others at different echo times or they will appear spectrally resolved with more accuracy at higher fields, if the magnetic field homogeneity is preserved [21].

Early studies conducted on biological tissues made use of the ^{31}P nucleus, since the main focus was on bioenergetic characterization. There was also an

interest in the ^{13}C nucleus, but its NMR-sensitivity is even lower than ^{31}P. Later on, it was evident that the ^{1}H nucleus is characterized by the following advantages:

- the highest magnetogyric ratio among biochemically relevant nuclei, therefore the highest NMR-sensitivity
- high natural in vivo abundance
- fundamental brain metabolites are identified by resonance peaks resulting from functional groups with multiple protons (e.g. methyl groups).

^{1}H MRS is particularly important in human brain studies aimed to examining neurodegenerative diseases, tumours, strokes and genetic or acquired metabolic alterations, with the signal being recorded from specific structures or lesions within the brain. Currently ^{1}H MRS is the most widespread clinical examination because of the high sensitivity and natural abundance of the proton, but also because this is the nucleus used for MRI, which means that both MRI and MRS can be performed basically with the same hardware (RF coils, amplifiers, preamplifiers, receivers, etc.).

Skeletal muscles can be investigated through multinuclear spectroscopy (^{1}H MRS to study lipid metabolism, ^{13}C MRS for carbohydrate metabolism and ^{31}P MRS for a wider analysis of energy metabolism).

2.1.2 Clinical relevance of ^{1}H MRS studies

As previously mentioned, the proton is the most NMR-sensitive nucleus with high natural abundance. Since most of metabolites contain hydrogen nuclei, ^{1}H MRS is an efficient investigation to detect and quantify a large number of biomolecules. Despite the fact that the water resonance is usually orders of magnitude larger than metabolite peaks, the intrinsic limitation of ^{1}H MRS is the narrow chemical shift window inferior to 5 ppm. This causes metabolite resonances to overlap, thus making difficult to discern their

positions in the spectrum and quantify their concentrations. An example of an in vivo proton spectrum is reported in Figure 2.1.

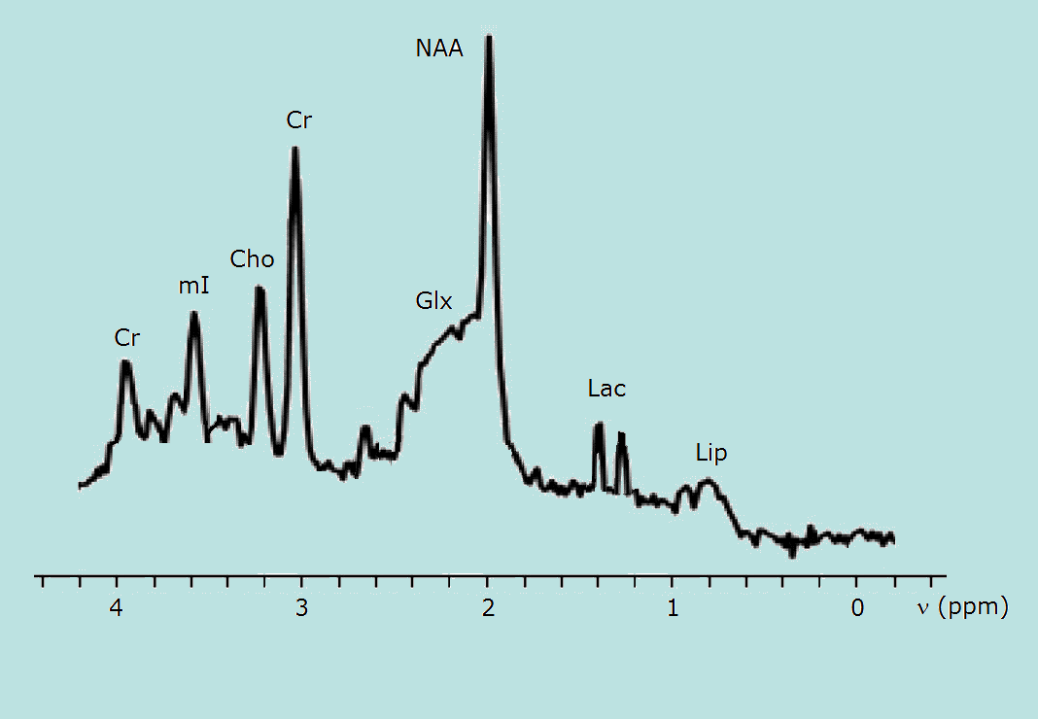

Figure 2.1: In vivo proton spectrum of the main metabolites with frequency range of 4 ppm.

Proton brain MRS has become a conventional clinical examination which is performed using head coils in MR scanners. ^{1}H MRS allows the **evaluation and staging of brain pathologies** such as neurodegenerative diseases and multiple sclerosis. These illnesses lead to reduced recognition (e.g. Alzheimer's disease) or dementia, difficult motor performance or both (e.g. Parkinson's disease) [1]. They all have in common the decrease in neuronal function and the induction of neuronal cell death due to the triggering of apoptotic pathways and other mechanisms. The progression of these diseases can be assessed through the calculation of the variations in the concentrations of key metabolites. For instance, decreased NAA and increased mI levels in cortical areas are clear markers of the presence of Alzheimer's disease [1].

Additionally ^{1}H MRS can be useful to retrieve information related to the metabolic characterization of brain tumours in vivo, differentiate types and estimate the staging, the proliferation or the density of the tumour cells. For instance, it is possible to detect the transformation of the tumour to a more malignant subtype.

Furthermore, the **oxygenation status of a neoplasm** may be monitored through MRS. As the progression and proliferation of a tumour continues, the oxygen supply given by bloodstream becomes insufficient, thus determining that the oxygen concentration is significantly lower than in healthy tissues. This point may be relevant for treatment planning purposes since tumour hypoxia (i.e. low availability of oxygen in cancerous areas) has been widely associated with increased resistance to radiation therapy and chemotherapy [32]. Specifically, the key marker for nonoxidative glycolysis is Lactate.

Even though ^{1}H MRS examinations have been conducted mostly in the human brain, there is a growing interest in applying this kind of studies to other soft tissue organs, such as prostate and breast (with different metabolites in the relative spectrum) [32].

It is a clinical routine that MRS is performed for histological grading of tumours alongside other examinations, e.g. MRI, after the administration of a gadolinium-containing **contrast agent** to provide a better and more accurate volume localization thanks to contrast enhancement in the acquired images [1]. Apparently, no significant differences have been found between the performances of MRS before and after the injection of the contrast agent. The paramagnetic effects of contrast materials, which are supposed to damp the relaxation times, are mediated through dipole-dipole interactions between the protons of the metabolite and the unpaired electrons of the gadolinium ion. Anyway, this distance-dependent interaction falls off as $1/r^6$, thus making this effect rather unlikely. Furthermore, since the gadolinium-containing compound is characterized by elevated molecular weight, it does not pass freely through the membranes of healthy cells. Consequently, it has been

inferred that contrast agents do not considerably affect the interpretation of spectra [33].

Water is the most abundant hydrogen-containing compound with concentrations on the order of tens of M (approximate values are in the 30-60 M range depending on the regions of the brain [28]) giving rise to a prominent peak which hides metabolites in the spectrum. Therefore it is of crucial importance to suppress its resonance in order to be able to discern metabolite peaks. Typical values for water concentration in different regions of a healthy human brain are listed in Table 2.1.

Brain area	**Water concentrations (M)**
Cerebrospinal Fluid (CSF)	55.6
Grey Matter (GM)	43.4
White Matter (WM)	36.2

Table 2.1: Average concentrations of metabolites revealed in ^{1}H brain MRS in healthy subjects.

Despite the overshot height of water peak, most of the biomolecules which are involved in cerebral metabolism go undetected whether because their peaks are too small (therefore mistakable with background noise) or because they are hidden by more prominent resonances. Making use of high-field magnets allows the detection of several elusive metabolites, such as glucose, branched amino acids and others, thus extending the metabolic information of spectra, provided that the field homogeneity is mantained [16]. Anyway, their peaks might be more clearly discernible under certain pathological conditions as their concentrations rise.

2.1.3 Principal metabolites in ^{1}H MRS

The detectability of biomolecules and the appearance of spectra are strongly related to echo times in ^{1}H MRS [1]. At short TEs (20-40 ms) the spectra

are characterized by a high SNR and the detectability of most of the peaks, although they tend to overlap. At intermediate TEs (135-144 ms) the Lactate doublet is inverted below the baseline. At longer TEs (270 ms or more) the SNR is lower but the identification of some metabolites (N-acetyl aspartate, Choline and Creatine) is clearer because the signals of others is lost into noise.

The most important metabolites detected in brain ^{1}H MRS are listed below (note that the chemical shift displacement of each compound is relative to TMS as the reference peak, even though it is absent in spectra obtained in vivo):

- **N-acetyl aspartate** (NAA) is found in neurons and it is synthetized in the mitocondria. Its most prominent resonance originates from the methyl group at 2.01 ppm, although other lower peaks appear at 2.49, 2.67 and 4.38 ppm respectively corresponding to other chemical groups. Generally, the NAA resonance at 2.01 ppm is the highest peak in ^{1}MRS with prior water suppression. Chemical structure of NAA is depicted in Figure 2.2 [34].

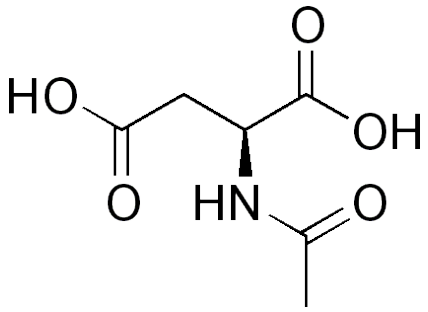

Figure 2.2: Chemical structure of N-acetyl aspartate.

Even though its function in the human brain has not yet fully understood [2], the NAA resonance is used as a marker of neuronal density and integrity, since a decrease in the intensity of the peak is observed in disorders characterized by neuronal dysfunction. In fact, most of neurodegenerative diseases (e.g. Alzheimer's and Parkinson's diseases)

typically exhibit decreased NAA concentration in cortical areas, as clinical studies indicate [35].

- **Choline** (Cho) signal is a composite peak essentially consisting of contribution from trimethyl amine groups of Choline-containing compounds, specifically glycerophosphocholine (GPC) and phosphocholine (PC), located at 3.20 ppm. These two contributions cannot be separated because of their smallest relative chemical shift. Basic structure of Choline is represented in Figure 2.3 [36].

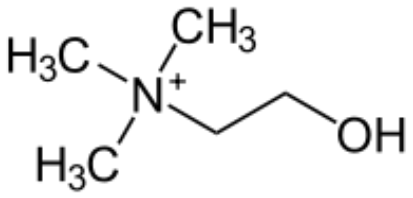

Figure 2.3: Chemical structure of Choline.

These two molecules take part into the membrane synthesis and degradation (i.e. phoshpolipids in the cellular membrane). Cho concentrations are expected to be higher when increased membrane turnover is triggered (e.g. tumours) or when pathologies induce active demyelination. Consistently, glial cells are characterized by high levels of Choline. Anyway it should be mentioned that Cho levels highly fluctuate in different regions of the brain.

- **Creatine** (Cr) is identified by two composite resonances at 3.03 ppm and 3.93 ppm originated by the methyl and methylene hydrogens respectively. The peaks arise from to the contribution of both Creatine and Phosphorylated Creatine (PCr), which are present in neuronal and glial cells. These two molecules cannot be distinguished because of the small chemical shift. The separation is achievable only at ultra-high fields.

  Cr plays a major role in the energy metabolism of tissues, specifically in the reversible creatine kinase reaction consuming ATP to produce

ADP and PCr (the reaction is depicted in Figure 2.4 [37]).

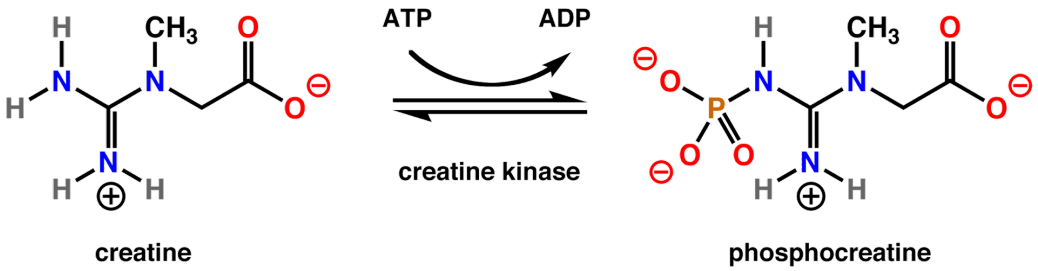

Figure 2.4: Creatine kinase reaction.

Furthermore, since the concentration of total creatine is relatively constant regardless of fifferent diseases or the age of the patients, its peak at 3.03 ppm is frequently used as an internal concentration reference, thus assuming the value of 0.00 ppm. Anyway, it should be stressed that this choice is not convenient in various illnesses, including tumours and stroke, in which a decrease in Cr concentrations is frequently observed [2].

- **Lactate** (Lac), or Lactic acid, is a compound which is difficult to detect in general because of its low abundance within the human brain under normal conditions. Its three methyl protons (shown in Figure 2.5 [38]) give rise to a doublet resonance located at 1.31 ppm thanks to weakly coupled interactions (scalar coupling constant for Lac is 7 Hz). Its methine proton resonates at 4.10 ppm (difficult to observe in vivo).

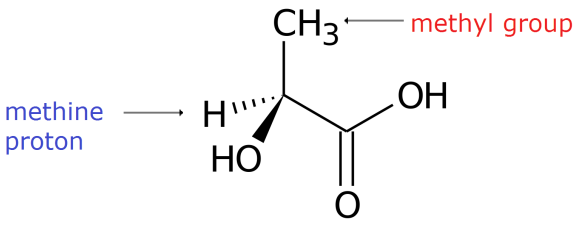

Figure 2.5: Chemical structure of Lactate.

The concentrations of Lactate are increased in pathological conditions, especially in cases where there is lack of oxygen (e.g. hypoxia or ischemia), since the metabolism of glucose through the Krebs cycle cannot be sustained and anaerobic glycolysis is activated. In fact, Lac concentration values might rise above 10 mM when oxygenation is insufficient [39].

In pathological conditions such as tumours or stroke, Lactate may be difficult to distinguish from possible overlapping lipid resonances originating from the brain itself or contamination from the very strong lipid signal from the scalp (it is always preferable to select a VOI farther from fat areas). Moreover, lipid resonances (Lip), which are distributed around 1.5 ppm, are prominent in skeletal muscle spectroscopy. The inversion of Lac peak at echo times close to 144 ms can be exploited for a more accurate identification [21].

The Lac inversion is clearly evident performing PRESS because it makes use of two spatially selective 180° pulses. At intermediate TEs of about 144 ms, Lac spins are 180° out of phase because of the relative chemical shift displacement of the methyl group and the methine proton. This non-correspondence in the VOIs selected determines that not all the Lac spins are excited because of the application of the two inversion pulses [2]. The superposition of the two opposite signals lead to the cancellation of the peak from the spectrum. This effect is called "**anomalous J modulation**" [39]. The echo time at which Lac doublet is inverted $\mathrm{TE}_{\mathrm{inversion}}$ is related to the relative coupling constant:

$$TE_{inversion} = \frac{1}{J_{Lac}} = \frac{1}{7\mathrm{Hz}} = \ 144\mathrm{ms} \tag{2.1}$$

The relative signal loss $\frac{\Delta S}{S}$ is dependent on the chemical shift difference of the two proton groups $\Delta\omega_{CS}$ and the bandwidth of the RF pulse $\Delta\omega_{RF}$.

$$\frac{\Delta S}{S} = 2\frac{\Delta\omega_{CS}}{\Delta\omega_{RF}} \tag{2.2}$$

An example of the inversion of the Lac peak is depicted in Figure 2.6. The two spectra have been acquired using PRESS at TEs of 30 and 150 ms respectively.

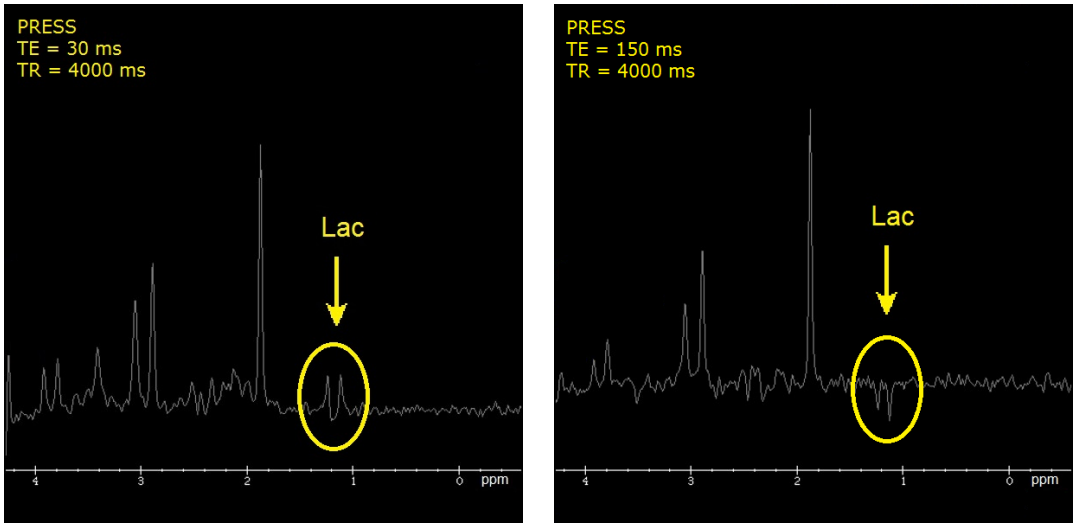

Figure 2.6: Proton spectra acquired using PRESS at 30 ms and 150 ms displaying the inversion of Lac doublet.

- **Myo-inositol** (mI) is a hexose sugar which gives rise to a strongly coupled multiplet in the spectrum. A doublet of doublets (originated by ^{1}CH and ^{3}CH protons) is centred at 3.52 ppm, a triplet (originated by ^{4}CH and ^{6}CH protons) is located at 3.61 ppm and minor resonances are also present at different frequencies. Its chemical structure is depicted in Figure 2.7 [40].

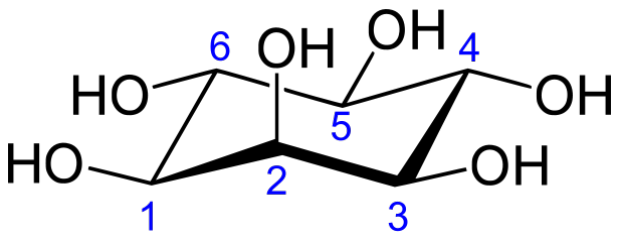

Figure 2.7: Chemical structure of Myo-Inositol.

Myo-inositol is considered a glial marker since typically higher concentrations are found in glial cells rather than in neurons and is involved in cellular signaling. Increased mI levels have been observed in Alzheimer's dementia and demyelinating diseases, such as multiple sclerosis [41], even though there is not yet a thorough comprehension of the pathophysiological role of mI.

- **Glutamate**(Glu), or Glutamic acid, and **Glutamine** (Gln) are amino acids which play a vital role in brain metabolism. Collectively they are referred to as a composite series of peaks named Glx because of the overlap of the two resonances, which are difficult to separate. This is because Glu and Gln are characterized by similar J coupling interactions and chemical shifts. The CH resonances are located around 3.7 ppm, while CH_2 multiplets are found between 2.1 and 2.4 ppm. Indeed, because of the superposition of the two peaks at 1.5 T, few studies take into account the variation of these compounds to evaluate disease status. Anyway, they can be spectrally resolved at fields of 7 T or higher. Their chemical structures are depicted in Figure 2.8 [42] [43].

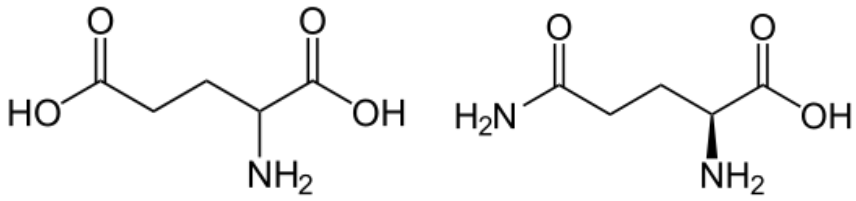

Figure 2.8: Chemical structures of Glutamate and Glutamine.

Glutamate is the most abundant amino acid in the brain and is an essential excitatory neurotransmitter, which is released during neuronal excitation and is taken up by astrocytes after diffusing across the synapse. These cells break down Glutamate to Glutamine, which is released and uptaken by neurons. The process repeats after Gln is converted back to Glu.

In conclusion, average concentrations of the main metabolites detected in ^{1}H brain MRS in healthy adult patients are listed in Table 2.2 [2].

Metabolite	**Concentrations** (mM)
NAA	8.0 - 12.0
Cho	1.0 - 2.0
Cr	4.0 - 5.5
PCr	4.5 - 6.0
Lac	0.5 - 1.0
mI	4.0 - 8.0
Glu	6.0 - 12.5
Gln	2.0 - 4.0

Table 2.2: Average concentrations of metabolites revealed in ^{1}H brain MRS in healthy subjects.

2.1.4 Temperature dependence of the water peak position

Water is the most abundant compound in human body. It is also the most prominent peak detected in ^{1}H MRS, such that it needs to be suppressed if metabolite peaks needs to be clearly viewed. However, its chemical shift position is highly dependent on local temperature. This should always be taken into consideration if water is the reference compound. Indeed, spectra acquired at different thermal conditions will possess slightly different internal referencing because of the displacement of the water peak. Basically, even though water concentrations do not fluctuate considerably among different pathologies, sometimes its peak is not considered an excellent reference choice because of its dependence on temperature [5].

In fact, adjacent water molecules form **hydrogen bonds** between hydrogen and oxygen nuclei, which cause a partial removal of the electron cloud

from the hydrogen, thus deshielding the nucleus, which resonates at a higher resonance frequency. When the temperature rises, the hydrogen bonds are more likely to bend, stretch and break because of the increased molecular tumbling. The outcome is that the hydrogen nuclei are more shielded, sense a lower local magnetic field and consequently they are characterized by a lower Larmor frequency [2]:

$$\omega_{water}(T) = \gamma(1 - \frac{2}{3}\chi(T) - \sigma(T))B_0 \tag{2.3}$$

where $\chi(T)$ is the water magnetic susceptibility at temperature T. However, the dominant contribution to the temperature dependence of the Larmor frequency of water is given by the variation of the electronic shielding constant $\sigma(T)$ of the proton nuclei.

Changes in the resonance frequency of pure water are approximately -0.01 ppm $^{\circ}C^{-1}$. Resonance frequencies of water in ppm units at typical temperatures of the human brain and room thermal equilibrium conditions are listed in Table 2.3 [5].

Temperature (°C)	**Frequency (ppm)**
37	4.70
22	4.85
20	4.87

Table 2.3: Resonance frequencies of water at different temperatures.

It is common practice to assess the fluctuations of the water peak due to temperature by estimating the chemical shift difference between water and a reference compound whose position in the spectrum is not affected by the thermal conditions. The typical choice is the methyl group of N-acetyl aspartate.

2.1.5 ^{31}P MRS studies

Even though ^{31}P is a nucleus with lower NMR-sensitivity and it is much less abundant than ^{1}H, this isotope has become more frequently used in clinical routines. This is beacuse phosphorous is contained in ATP, which is consumed and renewed in the conversion of glucose to energy. Phosphorous MRS allows a frequency window about 30 ppm large and no signal suppression is needed for a clear identification of peaks. However, the number of molecules detected by phosphorous MRS is lower in comparison with proton MRS, as it is depicted in Figure 2.9.

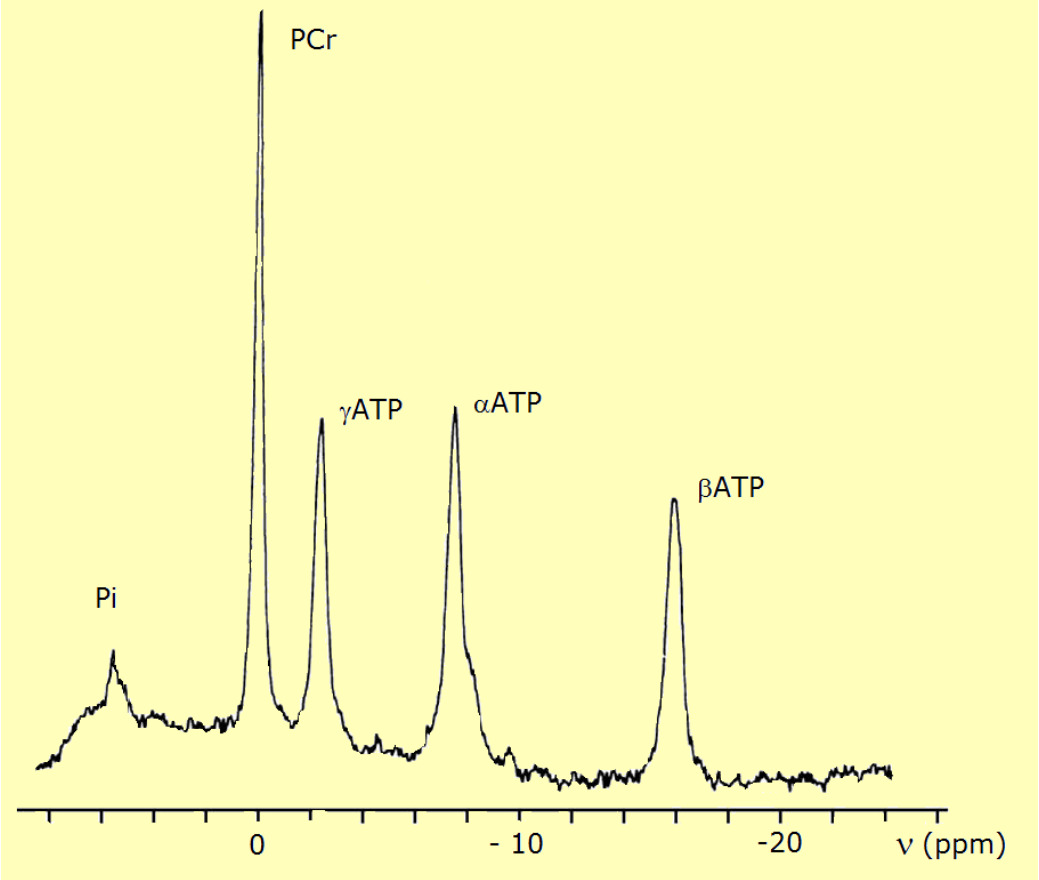

Figure 2.9: In vivo phosphorous spectrum of the main metabolites with frequency range of 30 ppm.

Additionally, even though phosphorous is less NMR-sensitive than hydro-

gen, which implies the need to excite larger VOIs than ^{1}H, the concentrations of the detected metabolites in muscles are higher than compounds in proton MRS (of the order of tens of mM) [21].

Furthermore, phosporous MRS requires modification in the acquisition hardware that must be adjusted to operate at the correspondent resonance frequency (25.88 MHz at 1.5 T). In vivo ^{31}P MRS is also characterized by shorter T_2 values, which makes preferable to use sequences with shorter TEs.

Performing phosporous spectroscopy at the typical static fields of clinical scanners, i.e. 1.5 or 3 T, is limited because of:

- low NMR sensitivy
- poor spectral resolution
- demand for large VOIs
- overlap of resonances

Anyway, optimization of ^{31}P MRS is achievable at ultra-high fields (e.g. 7 T or higher), which allow a more intense SNR [12]. In particular, the signal can be amplified through nuclear Overhauser effect. Water protons are continously irradiated at low power in the duration of the repetition time except for the ^{31}P signal sampling. Saturated protons will interact with phosphorous nuclei via dipolar cross-relaxation. In early studies, nOe enhancement has been observed in phosphorous spectra at 7 T [44]. This might be particularly useful to enhance the signal of low concentration compounds such as Inorganic Phosphate, which is often mistakable with the noise baseline.

The aim of this kind of investigation is to characterize the metabolites that are involved in the bioenergetics of tissues, thus providing information on oxidative metabolism and glycolysis. The main applications of ^{31}P MRS are directed towards the analysis of muscular tissues (e.g. neuromuscular disorders such as muscular dystrophy), the liver and the heart [45], also in relation to exercise-recovery paradigms.

The positions of resonances in ^{31}P spectra are variable and dependent on intracellular physiological parameters such as pH. The main phosphate-containing metabolites detected by MRS are listed below (with chemical shifts being given in relation to PCr as a reference):

- **PhosphoCreatine** (PCr) is placed at 0.00 ppm since it is used as internal concentration reference being the highest peak.
- **Inorganic Phosphate** (Pi) is the result of the breakdown of ATP to ADP. Its peak is located at 5.02 ppm.

$$ATP \underset{k_r}{\overset{k_f}{\rightleftharpoons}} ADP + Pi \tag{2.4}$$

- **Adenosine TriPhosphate** (ATP) plays a major role in transporting chemical energy within cells for metabolism. It is identified by three resonance at -7.52 ppm (α peak), -16.26 ppm (β peak) and -2.48 ppm (γ peak), each corresponding to each phosphorous atom in the molecule, labelled starting from the closest to ribose. Its chemical structure is displayed in Figure 2.10 [46].

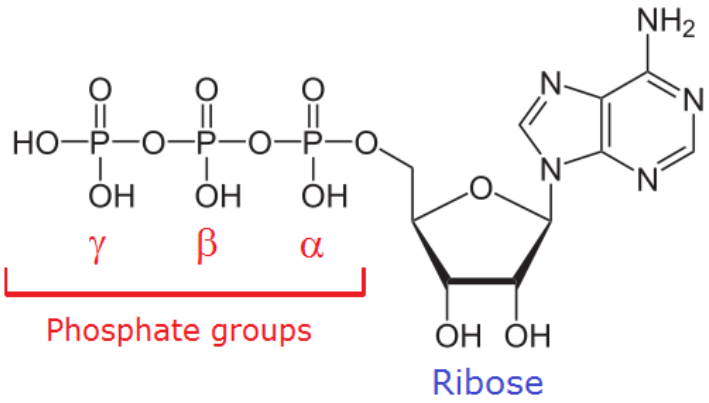

Figure 2.10: Chemical structure of ATP with its three phosphate groups.

Generally, other metabolites with typical concentrations lower than 1 mM go undetected [47].

2.1.6 ^{13}C MRS studies

Currently, ^{13}C MRS is not performed routinely in clinical examinations because of the hardware requirements which are typically not provided on clinical MR scanners, especially because of the low natural abundance of ^{13}C and the very low NMR-sensitivity, which demands for ultra-high fields. Consequently, carbon spectroscopy has been performed mostly in chemistry and industrial applications.

The appearance of ^{13}C spectra is characterized by several multiplet because of most of the carbon nuclei take part into covalent bonds with one or more protons. The carbon spectra allow a frequency window of about 200 ppm. However, despite the mentioned limitations, important studies have been carried out by research teams on brain ^{13}C MRS with the aim of analyzing the glucose cerebral uptake [12]. Metabolites related to proton spectroscopy such as Glutamate, Glutamine and Lactate are the main compounds detected.

2.2 Biological effects related to magnetic field exposure

2.2.1 Interactions of magnetic fields with human tissues and safety

There is no doubt that MRS and other NMR applications are relatively safer than other radiological examinations since they do not make use of ionizing radiations, which are proven to be harmful and impose risks to human health. Anyway, the debate regarding the potential risks caused by diagnostic MRI is still open and careful attention should be adopted in order to avoid unnecessary diagnostic examinations [48].

During a clinical MRS examination, a patient will be exposed to a static magnetic field B_0, gradients which vary with time and RF fields. Temporary

acute neurobehavioural effects such as eye-hand coordination speed and auditive working memory problems after the exposure to static fields between 1.5 and 3 T have been reported. Other studies discussed the possible effects related to fertility and pregnancy, but these have not been considered conclusive [48].

Staff members will be exposed to the **fringe field** (or stray field) from B_0, i.e. the boundary of the magnetic field of the magnet. The spatial extension of the fringe field depends on the magnet design and the amplitude of the static field; in particular the higher the field strength is, the larger the fringe field. Anyway the stray field decreases very rapidly with the distance r from the magnet:

$$B_{fringe}(r) \propto \frac{1}{r^2} \tag{2.5}$$

Generally, proper shielding is provided in the hospital facility to prevent the fringe field to extend to a considerable distance from the magnet [49]. Additionally, MR scanners are surrounded by a RF-shielding in copper, aluminium or steel, or Faraday cage, to avoid outer sources of radio frequencies from interfering with MR signals.

Anyway, it should be underlined that more evident effects are related to the switching of the gradients, which induces electric fields and flow of electric currents in conductive tissues. This effect may generate currents which might cause peripheral nerve stimulation (PNS), which is discomfortable for the patient but not harmful, stimulation of the cardiac muscle and magnetophosphenes, i.e. flashes of light caused by retinal stimulation.

On the other hand, the sensory effects related to static magnetic fields are vertigo, nausea and metallic taste sensations [48]. Headache, vomiting and numbness have also been reported by patients [12]. Other effects include the generation of electric potentials in moving and conducting tissues and the displacement and the malfunctioning of ferro-magnetic implants (clips, protheses, pacemakers, etc...).

2.2.2 Tissue heating

The principal effect and principal concern of RF exposure is tissue heating due to induced electric currents. Indeed, RF waves deposit energy leading to tissue heating with possible physiological effects, especially in heat-sensible organs such as the eyes and the testes. The power transmitted to a conductive medium of conductivity σ with induced electric field E can be estimated as:

$$P = \sigma E^2 \tag{2.6}$$

Therefore, the **Specific Absorption Ratio** (SAR) is introduced to measure the average rate at which energy is absorbed by the human body when exposed to a RF electromagnetic field [12]. It is defined as the power absorbed per mass of tissue and has units of Wm^{-1}.

$$SAR = \int_{sample} \frac{\sigma(r)|E(r)|^2}{\rho(r)} dr \tag{2.7}$$

where ρ is the density of the tissue. This is an average expression, SAR can also be evaluated locally taking into account that inhomogeneity of the RF field leads to a different local exposure. SAR values increase with the square of the field strength, RF power and the body size. Patients are weighted before the beginning of the examination to infer a rough estimate of an average SAR on the scanner monitor.

$$SAR \propto \frac{B_1^2}{\rho} \tag{2.8}$$

Thus, it is an immediate consequence that the frequency and the power of the radio frequency irradiation should be kept at the lowest possible levels to reduce the patient exposure. Some choices help to reduce SAR:

- use of quadrature coils for RF transmission
- avoidance of body coils for localized examinations (e.g. use of head coils in brain MRS)

- increasing TR

The International Electrotechnical Commission (IEC) has suggested that the temperature rise should be lower than 0.7 and 1 °C for normal and first-level controlled operations respectively (upper increases are avoided in most MR scanners). The corresponding SAR limits are listed in Table 2.4 [12].

Operating mode	**Temperature rise (°C)**	**Total body SAR** (W/m^{-1})	**Head SAR** (W/m^{-1})
Normal	0,7	2,0	3,2
First-level controlled	1,0	4,0	3,2
Second-level controlled	$> 1,0$	$> 4,0$	$> 3,2$

Table 2.4: Temperature rise and SAR limits at different operating modes (IEC values).

If higher fields are exploited in order to achieve better SNR and spectral resolution, careful calculations of SAR values must be performed not to exceed the suggested cautionary limits, especially if additional irradiation is applied to achieve nuclear Overhauser enhancement for resonances in the spectrum [44].

In addition, it should be mentioned that just as PRESS is characterized by a higher SNR than STEAM, so PRESS is associated approximately to twofold SAR values compared to STEAM [5].

Chapter 3

Data acquisition system and instrumentation

3.1 The MR scanner

3.1.1 Characteristics of GE Signa HDxt 1.5 T scanner

The MR scanner in the Magnetic Resonance examination room at Pavillion no. 11 of Policlinico S.Orsola-Malpighi in Bologna is a General Electric Signa HDxt 1.5 T [50], depicted in Figure 3.1. The apparatus is capable of performing both imaging and spectroscopic examinations. Its main characteristics are the following:

- a homogeneous superconductive 1.5 T magnet (CXK4 family) delivering a full 48 cm field of view and cooled to cryogenic temperatures by liquid helium.
- a 60 cm diameter bore: its dimension is a compromise between the comfort for the patient and good field homogeneity, which should require a narrow and long bore, unsuited for the patient.
- a 16-channel RF transmitter-receiver coil
- 18 shim coils to optimize and stabilize the magnet field homogeneity.

Figure 3.1: GE Signa HDxt 1.5 T.

- high-definition gradient coils engineered to produce high accuracy waveforms and reduce eddy currents.

The gradient coil performance is characterized by the values of gradient intensities and slew rates, i.e. the maximum rate of change of the gradient intensity per unit of time, which are listed in Table 3.1. Values refer both to calculations along the three axes, G_i and SR_i $(i = x, y, z)$, and along the diagonal direction, G_{eff} and SR_{eff}.

Gradient intensities along axes			**Gradient intensity along the diagonal**
G_x(mT/m)	G_y(mT/m)	G_z(mT/m)	G_{eff}(mT/m)
33	33	33	57
Slew rate along axes			**Slew rate along the diagonal**
SR_x(T/m · s)	SR_y(T/m · s)	SR_z(T/m · s)	SR_{eff}(T/m · s)
120	120	120	220

Table 3.1: Gradient intensity and slew rate values for GE Signa HDxt 1.5 T in the three directions.

3.1.2 GE Signa HDxt 1.5 T workstation

GE Signa HDxt 1.5 T workstation is located in the control room next to the examination room. All the commands to the MR scanner are given by the dedicated software provided by the manufacturer. The screen which appears when downloading the protocol is reported in Figure 3.2.

Several options and parameters can be selected by the operator. Only the ones concerning this study are listed below:

- pulse sequence: it is possible to choose between "Probe-P" and "Probe-S", which stand for PRESS and STEAM respectively, for single-voxel

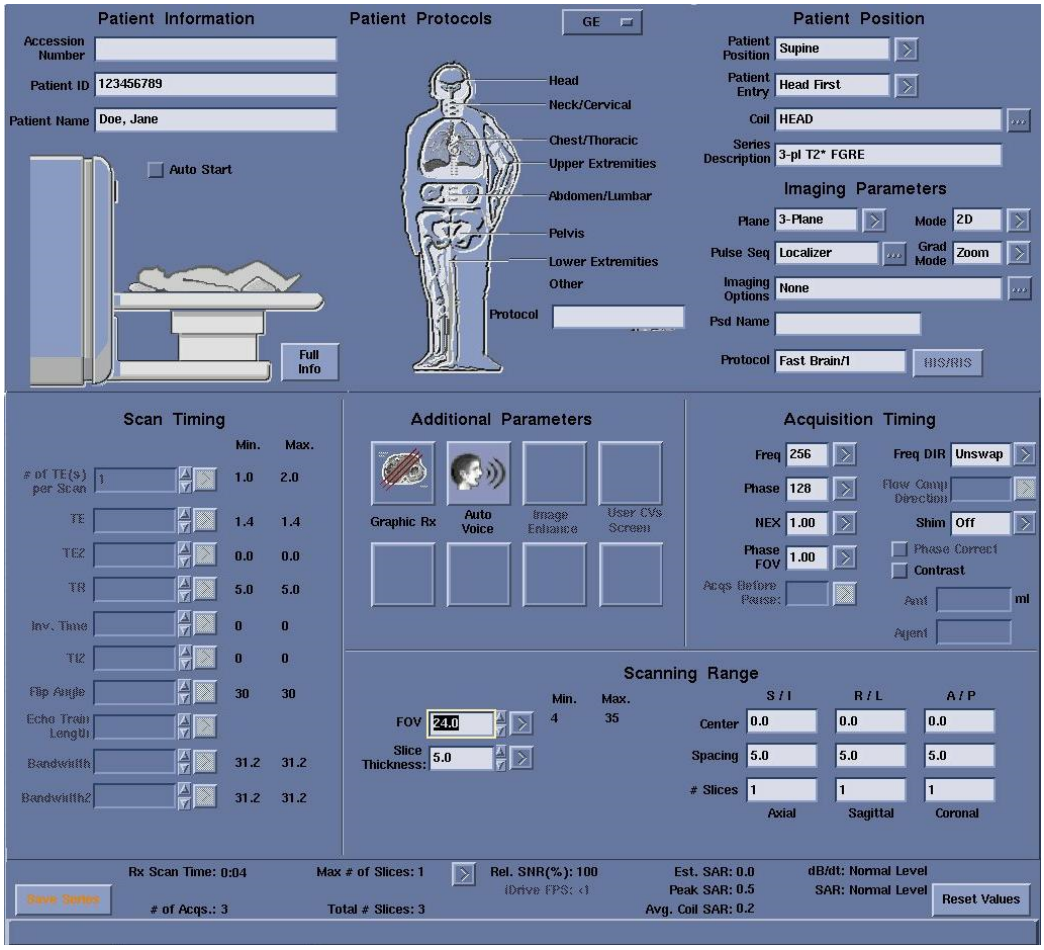

Figure 3.2: Monitor screen for protocol downloading.

spectroscopy. Three CHESS 90° pulses for water suppression are automatically included within the sequences for each excitation. It is possible to remove them manually if non-water-suppressed spectra are needed.

- echo time TE
- repetition time TR
- field of view
- number of excitations (NEX) for phase cycling. It can be set to 2 or 8.

- number of averages: it is the number of acquired FIDs in the sequence. It must be an integer multiple of NEX. The higher it is, the more improvement in SNR is observed despite the increase in the scan times.
- VOI selection and placement using scout images as guidance.

After the parameters have been selected, the sequence is downloaded. Now, a prescan step is needed for the system to accurately tune gains for power scaling and shimming gradients. This procedure can be done automatically or manually. The parameters of interest are:

- analog receiver gain (R1): it is the analog amplification factor. The allowed range lies between 1 and 13, where each unit corresponds to a 3 dB increment in the amplification of the detected signal.
- digital receiver gain (R2): it corresponds to the number of digital bits used by the receiver during data acquisition and digitalization and to the number of bits in each data word. Allowed values range from 1 to 30 with the selection of the extended dynamic range. Consequently, each data word occupies 32 bits of memory (two sign bits and 30 data bits).
- transmit gain (TG): this parameter can be adjusted in a range from 0 to 200, where each unit corresponds to a 0.1 dB change in the transmit gain. This is of utmost importance to adjust the transmitting RF power in order to obtain the correct flip angles. A correct transmit gain means that a 90° RF pulse flips the net magnetization vector on the transverse plane at best.
- centre frequency: its tuning is needed to match the transmitting frequency of the system to the precessional frequency of the nuclei in sample or patient under investigation. The closer these frequencies match, the more efficiently the resonance condition is achieved. The centre frequency for proton MRS with GE Signa HDxt 1.5 T is set close to 63.87 MHz.

- gradient shimming: it is possible to adjust the linear shims in the three directions by tuning the corresponding gradient currents.

After the completion of the prescan procedure, the scan itself can be lanched.

3.2 Additional instrumentation

3.2.1 Head coil

The measurements have been conducted with a standard GE 1.5 T MRI classic quad head coil no. 2384268, which is depicted in Figure 3.3. During examinations it has been placed on the table and centred by dedicated lasers. Being a surface coil, it is very sensitive thanks to its optimal size relative to the object under investigation.

In particular, this is a **quadrature coil**, which produces a RF field with circular polarization in transmission. The RF power received from the RF power amplifier comes into two signals (quadrature detection), which have a phase difference of $\pi/2$.

Before quadrature detection, the signal in the μV range must be amplified to the mV interval by a low-noise preamplier to make it less sensitive to noise. Since current ADCs are not fast enough to directly digitize the signal in the RF range, the NMR frequency ω_0 is down-sampled, i.e. mixed, with a generated receiver reference frequency ω_{ref} by a doubly balanced mixer (DBM). The procedure consists in the subtraction of the receiver reference frequency from the signal frequency.

$$\cos(\omega_0 t) \longrightarrow \cos(\omega_0 t)\cos(\omega_{ref} t) = \frac{1}{2}\{\cos[(\omega_0 + \omega_{ref})t] + \cos[(\omega_0 - \omega_{ref})t]\} \tag{3.1}$$

where the first term is a high-frequency component of the order of twice the Larmor frequency, which is removed by a low-pass filter, and the second one is a down-sampled term, which remains after filtering:

Figure 3.3: GE 1.5 T MRI classic quad head coil no. 2384268.

$$\frac{1}{2}\cos[(\omega_0 - \omega_{ref})t] = \frac{1}{2}\cos[(\omega_{IF})t] \tag{3.2}$$

where ω_{IF} is called the intermediate frequency. Thus, the signal is within the sampled bandwidth and is ready to be passed to the ADC.

In quadrature detection, if the receiver frequency is the same as the transmitter frequency, the offset frequencies may be both positive and negative in relation to the centre frequency. Directly applying Fourier transform to the signal, which displays a cosinusoidal behaviour, would lead to superposition of opposite frequencies because of the parity of the cosine function [7].

Therefore, the signal is decomposed into two counter-rotating components, only one of which will be rotating in the same sense as the magnetization. The signal is acquired along two perpendicular axes, after decomposition into its real and imaginary components in the rotating frame.

In fact, a quadrature coil can be used as both transmit and/or receive coil. When it is used as a transmitter coil, a power reduction of a factor of 2 results in comparison with a linear coil; on the other hand, when it is used as a receiver, an increase in SNR of up to a factor of $\sqrt{2}$ can be achieved [51].

3.2.2 GE spherical test phantom

GE manufacturers also provided a test phantom (depicted in Figure 3.4) which is suitable for spectroscopic quality assurance (QA) and the evaluation of the performance of the MR scanner. Another advantage of using phantoms as tools for testing is that they provide a common basis for the physicist and the vendor when discussing possible malfunctioning or flaws and the needed solutions.

Figure 3.4: GE spherical test phantom with its base.

GE phantom is a spherical phantom with diameter of 17 cm containing ^{1}H-MRS metabolites whose concentrations emulate in vivo brain concentrations. The temperature of the phantom can be read thanks to a built-in thermometer. Furthermore, other filling factors (e.g. paramagnetic metal ions) are added to obtain an **aqueous paramagnetic solution**. These compounds are introduced with the aim of reducing the T_1 and T_2 relaxation times to values on the order of hundreds of ms. Additionally, further compounds may be added to provide conductivities similar to those found in the human body. As a consequence, the phantom electrically loads the RF coil in a manner similar to human tissues [52]. The GE spherical phantom content is described in detail in Table 3.2.

Symbol	**Chemical name**	**Concentration**	**T_2(ms)**
KH_2PO_4	Potassium phosphate monobasic	50.0 mM	-
NaOH	Sodium hydroxyde	56.0 mM	-
NAA	N-acetyl aspartic acid	12.5 mM	400
Cr	Creatine	10.0 mM	265
Cho	Choline chloride	3.0 mM	175
mI	Myo-inositol	7.5 mM	75
Glu	Glutamic acid	12.5 mM	-
Lac	Lactic acid	5.0 mM	-
Azide	Sodium azide	0.10 %	-
GdDPTA	Gadopentetic acid	0.10 %	-

Table 3.2: Concentration and T_2 values for GE spherical phantom content.

It is important to underline that phantom spectra are typically well-resolved with flat baselines, thus facilitating the detection of MRS acquisition or post-processing issues. This is due to the fact that they lack several in vivo metabolites, lipids, macromolecules and susceptibility discontinuities. When considering single-voxel phantom spectra, the more homogeneous the static field is, the less contaminations from outer regions arise.

3.2.3 In-house phantom

The "Interconfronto di spettroscopia in RM" working group provided an in-house phantom for spectroscopic measurements containing an aqueous solution. It possesses a spherical shape with a 15 cm diameter and its content has not been specified intentionally. Therefore, appropriate test measurements will be performed to reach an assessment of the nature of the metabolites and their concentrations. The phantom and its measuring cylinder for filling are portrayed in Figure 3.5.

Figure 3.5: In-house phantom with its measuring cylinder for filling.

Chapter 4

Spectroscopic quality assurance

4.1 Concerns in MRS quality control

4.1.1 The compiling of the acceptance report

It is commonly established as a clinical routine the regular performance of Quality Assurance (QA), or Quality Control (QC), in order to evaluate and monitor the correct functioning of the MR scanner. Obviously, it is worth mentioning that the modalities of QAs must be a precise balance between spending an exceedingly large amount of time and resources checking all the parameters of interest and the necessity of not slowing down the regular course of the clinical work.

Each time a new or upgraded MR system is installed in the clinical facility, MR physicists carry out acceptance procedures to assess the equipment aspects of the scanner. Acceptance testing is needed for an accurate determination of whether the system delivered and installed corresponds to the requirements which were mutually agreed upon by both the buyer and the vendor in the contract. The specific measurements are listed in the **acceptance report**, which is the basic guideline for routine QAs. All the main trials which need to be performed and principal functional parameters are enlisted in this report.

Afterwards, the medical physicist can recommend relevant parameters for continuing quality assurance programs based on the information in the acceptance report. Furthermore, it must be pointed out that these operations must be performed at regular intervals of time to provide informations reliable in time. The QA operations are basically the same for systems working at different static fields. Anyway, at high fields increased susceptibility effects are expected because of the properties of the test object [12].

4.1.2 Image quality

Probably the main concern in MR QA is the assessment of parameters related to **image quality**. These measures are quantified by acquiring images of dedicated phantoms or test objects, which are usually provided by MR scanner manufacturers.

Since in vivo MRS is an image-guided application and since no direct spatial information per se is contained in the spectrum, it is crucial to quantify some of the parameters which are typically estimated during MRI QAs. In fact, even small movements in the midst of a clinical examination will lead to distortions in the acquired spectra. This kind of artifact is not recognizable by a simple observation of the spectrum and a parallel comparison with the relative image is needed.

Specifically, the principal quantities of interest and trends which are estimated both in MRI and MRS QAs are listed below:

- Signal-to-noise ratio (SNR) is fundamental in QA to assess the sensitivity of the imaging system, i.e. the prominence of the desired signal in relation to the level of background noise.
- image uniformity response in relation to field homogeneity.
- the increase of the signal proportional to the volume of interest.
- the regularity of the signal trend along the image axes.

All these quantities have been measured in the MRS quality assurance that has been performed on a spherical phantom.

4.1.3 Spectral quality

It is fundamental to examine the overall regularity and quality of the acquired spectra for MRS to be reliable. Most MR system manufacturers provide aqueous tissue-mimicking MRS phantoms that contain chemical compounds of interest in concentration ratios which approximate the in vivo values. They are useful to estimate the degree of water suppression that is reachable and determine the SNR of the metabolites in water-suppressed MRS scans.

It is common practice to perform a few spectral acquisitions (typically PRESS and/or STEAM) to monitor the system response periodically. For brain spectroscopy purposes, the phantom should be placed at the centre of the head coil. The following steps must be taken into account when placing the phantom:

- allowing the phantom fluid to settle before beginning the acquisition series
- letting the phantom fluid reach thermal equilibrium with the environment (the phantom may be left in advance in the magnet room to ensure this condition)
- minimization of mechanical vibrations and motions
- avoidance of bubble formation, which may cause artifacts in the image

Before the spectral acquisition, it is recommended to prescribe the VOI on a conventional MR image and then acquire an image of the VOI using the MRS localization sequence in the phantom. Thanks to this operation, the spatial positioning accuracy of the VOI can be easily assessed. This should be performed both for VOIs near the isocentre and far from it.

Given the short amount of time in QAs, it is a suitable choice to perform single-voxel sequences with short echo times ($\simeq$ 30 ms). The shorter TEs will employ higher gradient amplitudes and sometimes shorter slice-selective RF pulses that might cause eddy current and outer volume contamination artifacts in the spectra.

The basic estimation in spectral quality is the integration of the peak areas of the biochemical compounds in the phantom by fitting Lorentzian peaks to the metabolite ones in the water-suppressed spectrum. This calculus is generally performed by the workstation software. Minimal post processing procedures, such as zero filling, Fourier transformation, and spectrum phasing, are performed beforehand on the single-voxel time-domain data by the software, while no time-domain or frequency-domain filtering are applied.

The workstation software should be able to calculate **spectrum noise** as the root mean square noise (RMS noise) about the spectrum baseline in a region with no metabolite peaks. Consequently, the SNR of a peak of interest can be estimated as:

$$SNR_{peak} = \frac{\Sigma_{peak}}{RMS} \tag{4.1}$$

where Σ_{peak} is the area under the peak. The SNR may be also calculated as the ratio of the height of the peak and RMS noise, but this choice is less convenient because the height is more sensitive to voxel shimming than the integrated area, thus making this measurement less reliable.

Anyway, it should be mentioned that the peak area is highly sensitive to RF coils characteristics. Therefore, the phantom must be placed in the same location on each periodical trial to ensure the same coil loading. A proper base for the phantom should be mounted for this purpose. In addition, since the behaviour of the compounds within the phantom are sentitive to thermal conditions, it is highly recommendable to check its temperature in advance to ensure that the QA is performed in the same status each time [12].

4.2 Quality assurance on GE spherical phantom

4.2.1 Signal localization

The quality assurance measurements have been performed on the dedicated GE MRS spherical phantom, whose characteristics have been described in the previous chapter. The image analysis has been carried on using ImageJ as image processing software.

The phantom was positioned on the table with two head cushions to prevent it from moving. Later, laser focusing was performed for an accurate centring and alignment within the head coil before moving the table inside the bore of the magnet. A scout sequence was applied in advance.

The preliminary **scout sequence** guarantees quick, low-resolution and large FOV scans which are applied to accurately plan the longer high-resolution diagnostic scans in the region of interest and determine the slice position and saturation bands. Scout images are essential in order to plot out the locations for subsequent diagnostic MR images. The saturation bands are used to selectively remove any area of signals which may cause artifacts in the acquisitions. They are chosen with the same manner as image slices, but they are followed by strong crusher gradients to ensure dephasing. Examples of scout images acquired are reported in Figure 4.1.

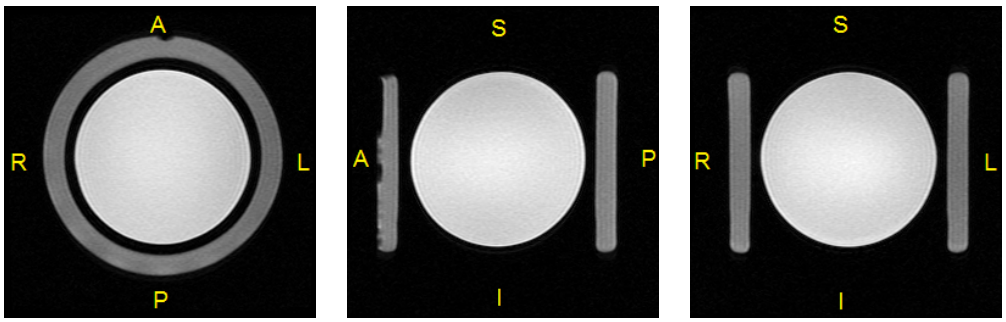

Figure 4.1: Examples of axial, sagittal and coronal scout images.

After the scout sequence, two spin echo sequences were applied in order

to acquire two scans of the whole phantom. A square-shaped 20 × 20 mm ROI was selected in both acquired images using the function ROI manager on ImageJ functions and the relative image was saved to view the ROI centring. Afterwards, the subtraction between the phantom image and the ROI image was performed in order to determine the position of the ROI within the phantom. The corresponding images are depicted in Figure 4.2.

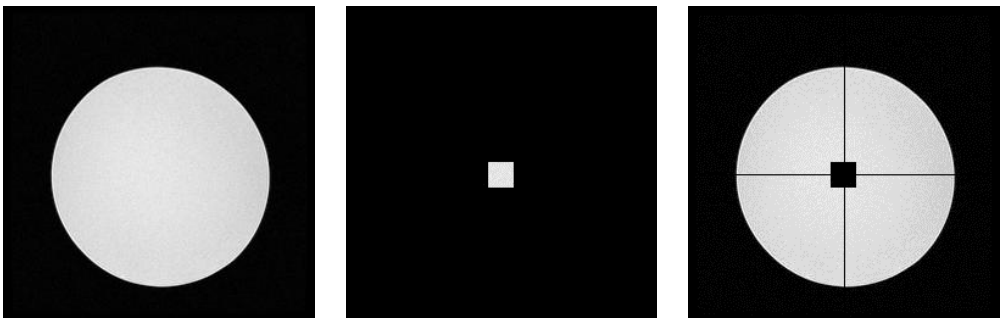

Figure 4.2: Images of the whole phantom, the selected ROI and the localization of the ROI within the phantom.

4.2.2 SNR measurements in the images

Signal-to-noise ratio (SNR) is a parameter of utmost importance to evaluate the overall performance of the acquisition system. It is a simple index of stability of the apparatus. The assessment of SNR can be obtained both from the spin-echo image which guides spectroscopic sequences and the acquired peaks in the spectrum.

Changes in the magnetic field strength over time can affect the SNR of conventional imaging and spectroscopy data. In superconducting magnets this effects are due to small resistive losses in the superconducting wire and temperature fluctuations in the examination room [52].

Typically, SNR is affected by instrumental factors such as field strength, characteristics of coils, coil loading and bandwidth. SNR measurements in MRI QAs are obtained by the quantification of values in a uniform or "flood field" phantom. SNR has been evaluated taking into account two different

methods:

- the **signal-background method** computes the average signal as the mean grey level intensity from an extended ROI within the phantom, whereas the noise is measured from the standard deviation of the pixel values of smaller ROIs in the background area outside the phantom. A graphical representation of the ROIs is given in Figure 4.3.

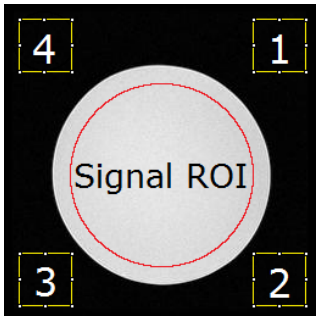

Figure 4.3: ROIs in the signal-background magnitude image.

Therefore, SNR is calculated as:

$$SNR_{sign-back} = 0.655\frac{\bar{S}}{\sigma_n} \tag{4.2}$$

where $\bar{S}$ is the mean signal in the extended ROI, σ_n is the average noise standard deviation of the smaller ROIs and 0.655 is a correction factor for the Rician distribution for the background noise, which will be discussed below.

- the **NEMA method**, developed by the National Electric Manufacturers Association, consists in the acquisition of two identical images consecutively, which will be used in image subtraction. The signal is measured as the mean value of the average grey levels in an extended ROI covering at least 75% of the phantom area defined in both images, while the noise is measured from the standard deviation of pixels within a ROI of the same dimensions in the subtraction image, as depicted in Figure 4.4.

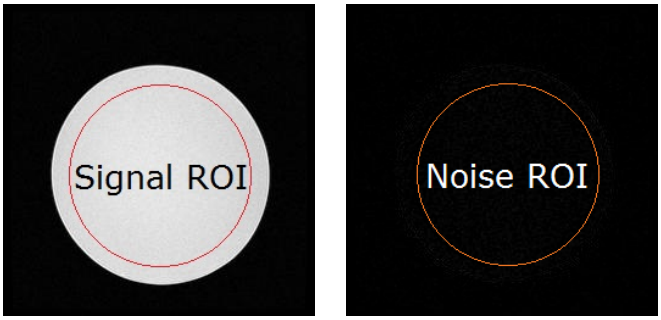

Figure 4.4: Signal and noise ROIs in the spin-echo image and in the subtraction image.

Consequently, SNR is computed as:

$$SNR_{NEMA} = \sqrt{2}\frac{\bar{S}}{\sigma_n} \tag{4.3}$$

where $\sqrt{2}$ is an additional factor to compensate for the greater standard deviation in the subtracted image. It is worth mentioning that the variance of the grey levels follows a Gaussian distribution in the high signal ROI and in the subtracted image for the NEMA method, which is consistent with the absence of the Rician distribution correction factor in the relation.

The assumption of the noise in MRI magnitude images following the Gaussian distribution might lead to an underestimation of the true noise content, unless the SNR is high. Indeed, the noise in MRI image is governed by the **Rician distribution** [53]. This distribution is far from being Gaussian for SNR smaller than two and rather tends to the Rayleigh distribution for SNR closer to zero.

This behaviour is due to the fact that after considering the modulus of the Fourier transform of the signal all the negative values are made positive and the mean is greater than zero. This results in a smaller standard deviation in comparison with the original Gaussian behaviour, which explains the correction factor in the signal-background SNR.

The probability density function $p_M(M)$ of a Rician distribution is given by:

$$p_M(M) = \frac{M}{\sigma^2} e^{-\frac{M^2+A^2}{2\sigma^2}} I_0(\frac{M \cdot A}{\sigma^2}) \tag{4.4}$$

where M is the measured pixel intensity, A is the the pixel intensity in the absence of noise and $I_0(\frac{M \cdot A}{\sigma^2})$ denotes the zeroth order Bessel functions of the first kind. M and A are related by the following equation:

$$E(M^2) = A^2 + 2\sigma^2 \tag{4.5}$$

where $E(M^2)$ stands for the expected value of M. The discrepacy between M and A is due to the nonlinear mapping of pixels in magnitude images which introduces a bias.

As previously mentioned, SNR has been calculated according to both methods. In particular, $SNR_{sign-back}$ has been calculated as the mean of the SNR calculated on both the acquired images to provide an estimate from both of them. The computed values are listed in Table 4.1.

Method	**SNR**
signal-background	118
NEMA	115

Table 4.1: SNR values calculated by signal-background and NEMA methods.

Measured SNR is generally estimated to disagree with the value computed during the acceptance testing if it moves away from it more than 10%. Referring to this point, the SNR measured by the two methods are considered to be in good agreement since their discrepacy falls between 10% in relation to each other.

In conclusion, it is worth mentioning that there is no reason to prefer one SNR measurement method over the other. However, it is common practice to choose the procedure suggested by the vendor to reach acceptable and comparable results in relation to calculations in the acceptance report as

reference. Therefore, acceptance criteria for SNR cannot be in general terms but will always be system specific.

4.2.3 Estimation of image uniformity

Image uniformity is the ability of the MR scanner to produce a constant signal response over the field of view when the imaged object is characterized by homogeneous MR characteristics [54]. This parameter is influenced by factors such as inhomogeneities in the static or in the RF field and eddy currents. Indeed, a badly shimmed magnet will lead to low uniformity values measured in the acquired images.

This quantity has been computed by selecting a ROI about 75% of the phantom area and determining the maximum and the minimum grey-level values S_{max} and S_{min}. The expression for uniformity U in percentages is the following:

$$U = [1 - \frac{S_{max} - S_{min}}{S_{max} + S_{min}}] \times 100\% \tag{4.6}$$

The uniformity values for the two acquired spin-echo images are indicated in Table 4.2.

	Uniformity
Image 1	91.8%
Image 2	92.4%

Table 4.2: Uniformity values for the acquired spin-echo images.

The ideal value for uniformity is 100%. Therefore, the discrepacy from the ideal condition is 8.2% and 7.6% respectively. However, uniformity values above 80% can be approximately regarded as acceptable at 1.5 T.

4.2.4 Dependence of the signal intensity on the excited volume

According to the principles of NMR, the intensity of the detected signal increases proportionally with the increase of the dimensions of the excited volume. This trend is determined by the statistical increase of the signal thanks to the excitement of a larger number of nuclei which contribute to the formation of the NMR signal.

With this assumption in mind, a few measurements of signal intensity have been performed while selecting concentric square ROIs of different dimensions on the axial image, as displayed in Figure 4.5.

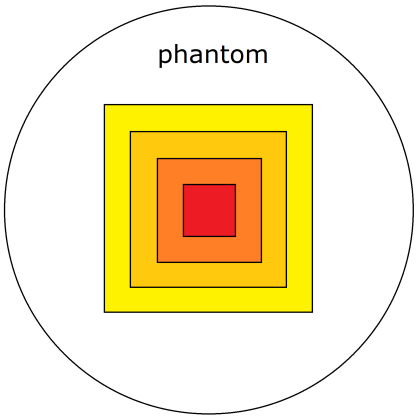

Figure 4.5: Selection of concentric square ROIs at the centre of the phantom.

In fact, if there were malfunctions of any kind in the acquisition system which may contribute to the distortion of the signal, the expected statistical increase of the signal intensity with the selection of larger ROIs would not be observed.

Measurements have been performed using ImageJ functions calculating statistical estimates over the ROIs. Values for the ROI area measured both in pixels $\times$ pixels and in mm^2 and the total signal intensity are reported in

Table 4.3. The total signal intensities have been computed summing the grey level intensities for the pixels contained in the ROIs.

ROI area (pixels × pixels)	**ROI area** (mm^2)	**Signal intensity** ($\times 10^4$)
10 × 10	88	2.29
20 × 20	352	9.18
26 × 26	594	15.51
38 × 38	1269	33.08
42 × 42	1550	40.37
52 × 52	2377	61.76
64 × 64	3600	93.32
74 × 74	4813	124.47
84 × 84	6202	159.90
96 × 96	8100	208.02
106 × 106	9875	252.73
116 × 116	11827	301.51

Table 4.3: ROI area and total signal intensity values.

Additionally, a plot showing the linear trend of signal intensity at varying ROI dimensions is reported in Figure 4.6. The straight fitting line equation for ROI signal S_{ROI} in function of ROI area A_{ROI} obtained by the method of least squares is reported below:

$$S_{ROI} = (2.5195 \cdot A_{ROI} + 0.0238) \text{ greylevels} \tag{4.7}$$

with Pearson's product-moment correlation coefficient equal to

$$R = 0.996 \tag{4.8}$$

indicating good strength of linear relationship between the two variables.

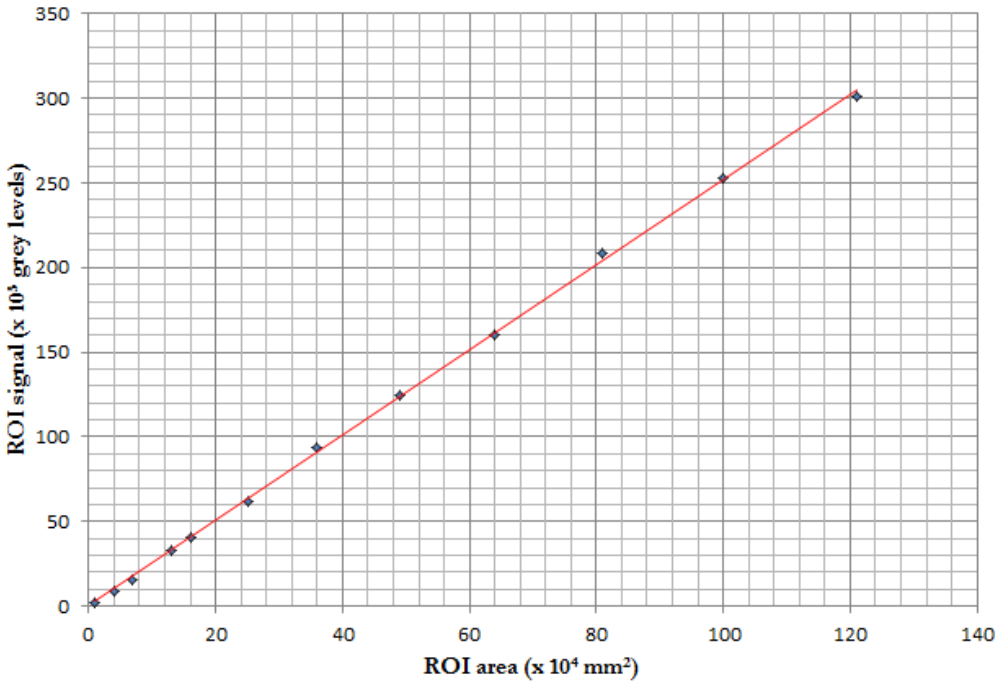

Figure 4.6: Proportionality of the total signal intensity at varying ROI areas.

It is evident from the plot in Figure 4.6 that the expected linear trend of signal intensity in function of the ROI area is confirmed. This is an immediate piece of evidence that the acquisition system is stable and is not affected by clear malfunctions or distortions of any kind.

4.2.5 Evaluation of the homogeneity of the static and the RF magnetic fields

A common procedure to assess the homogeneity of both the static and the RF magnetic fields consists in the evaluation of the constance of the signal along the axes of the principal magnet. Indeed, the signal has been measured within square ROIs along the anterior-posterior (A/P) axis and the right-left (R/L) one in the axial image. In particular, the 20×20 mm^3 ROI has been shifted repeatedly along both axes by steps of 20 mm to take into account the overall behaviour of the signal at different positions within the phantom. A

schematic representation of the voxel displacement along the A/P and R/L axes is reported in Figure 4.7.

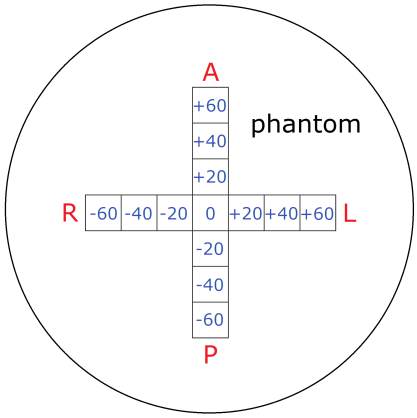

Figure 4.7: Steps in mm in the displacement of the selected ROI along the A/P and R/L axes.

Indeed, the assessment of the homogeneity of the static and the RF magnetic fields over a large region is of fundamental importance for spectroscopic purposes. If the static or the RF field displayed considerable fluctuations, the acquired spectra would be greatly distorted and a reliable identification of metabolites would be compromised. Possible fluctuations of fields are easily detectable over an image of a spherical phantom with a homogenous solution of compounds.

The ROI signal intensities measured in correspondence of each different position along the A/P axis are reported in Table 4.4. These values are also represented graphically in Figure 4.8.

The same procedure has been performed over the R/L axis. The results are listed in Table 4.5 and represented in Figure 4.9 as well.

As it can be inferred both from Figure 4.8 and Figure 4.9, the exhibited trends are approximately constant over both of the considered axes. These are evidence of the good homogeneity of the spatial response, which conse-

ROI displacement (mm)	**Signal intensity** ($\times 10^3$)
+ 60	87.8
+ 40	90.4
+ 20	91.8
0	91.8
- 20	90.6
- 40	88.7
- 60	85.9

Table 4.4: ROI signal intensity values at different locations along the A/P axis.

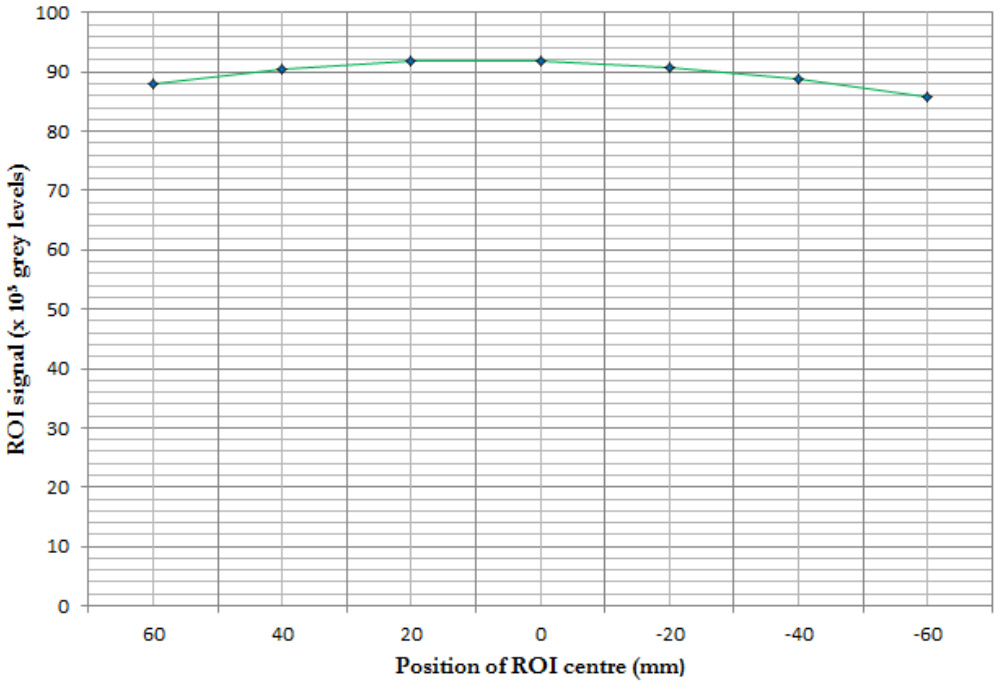

Figure 4.8: ROI signal intensity along the A/P axis.

ROI displacement (mm)	**Signal intensity** ($\times 10^3$)
- 60	87.8
- 40	89.4
- 20	90.9
0	91.8
+ 20	90.9
+ 40	89.6
+ 60	87.8

Table 4.5: ROI signal intensity values at different locations along the R/L axis.

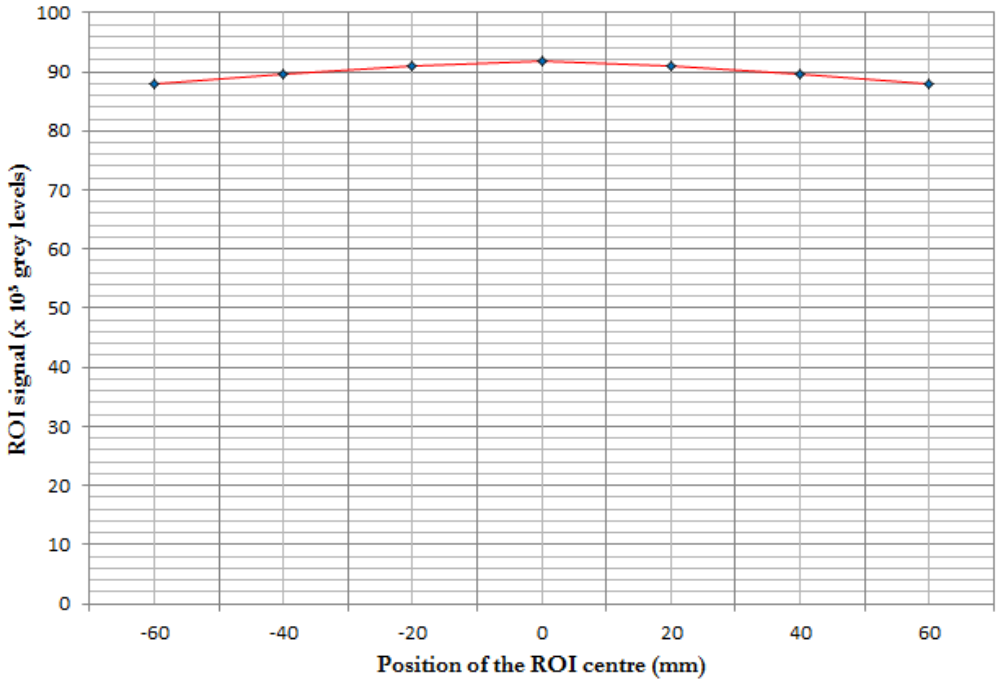

Figure 4.9: ROI signal intensity along the R/L axis.

quently proves the homogeneity of the contribution of both the static and RF magnetic fields and the good performance of the gradient coils and the transmitter-receiver coil.

In addition, examining approximately Figure 4.8, it is deducible that the centre of the spherical phantom does not correspond exactly to the isocentre of the magnet because of a displacement of about 10 mm along the negative A/P half-axis. This is due to an imperfect alignment because of the use of cushions as bearing for the phantom. Anyway, this discrepancy is negligible and the measured results are sufficient to confirm and highlight the homogeneity of the static magnetic field and the correct functioning and stability of the coils of interest.

4.2.6 SNR and concentration measurements in the spectra

It is important to mention that establishing judgement parameters for spectral quality and artifact recognition for clinical applications of MRS is an extremely difficult task. Fluctuations of metabolite concentrations, SNR and RMS noise are some of the relevant parameters for these estimations [55]. However, these calculations are always dependent on the specific algorithm applied to extract this information from the spectra.

The most suitable choice for SNR measurements in the spectrum is the application of single-voxel localization sequences at short TEs and short TRs to successfully exploit the available time for QAs. Shorter TEs will employ higher gradient amplitudes and shorter localization sequences.

The SNR strongly depends on the phantom solute concentrations, T_1 and T_2 values of metabolites, TRs, TEs, the sequence choice and number of excitations. T_1 and T_2 values found in literature of the main biochemical compounds for in vivo MRS are given in Table 4.6 [5]. It should be outlined that these data are only approximate per se, since they might differ significantly with B_0 magnetic field strength and confinement conditions in various tissues.

Molecule	T_1 (ms)	T_2 (ms)
NAA	1368	376
Cr	1424	217
Cho	1369	346
mI	1124	162
H_2O	380-1470	60-130

Table 4.6: Relaxation times for the main brain biochemical compounds at 1.5 T.

Three STEAM and three PRESS sequences with TE = 30 ms and TR = 2000 ms have been applied on the phantom (at 22°C temperature), which had been previously centred within the head coil and placed at the isocentre of the magnet. The dimensions of the selected volume are $20 \times 20 \times 20 mm^3$. Water is suppressed by the three CHESS pulses embedded in the GE ProbeS and ProbeP sequences in order to view the metabolite resonances, although the water peak is acquired anyway at a certain point in the sequence. The NEX is set to 2 in order to acquire the spectra in low SNR conditions.

The concentrations of some compounds (NAA, Cr, Cho, mI and water) have been automatically computed by the workstation software. Their values for each acquisition and their computed mean are reported in Table 4.7. Also the ratios of the compound mean value over Cr concentrations have been computed. Indeed, Cr is taken as reference because of its in vivo relative stability [2].

The ratio between water and Cr concentrations in comparison with the other ratios outlines that water concentration is about 3-4 orders of magnitude greater than metabolite. This evidence confirms the "tissue-mimicking" properties of GE spherical phantom. Furthermore, it is confirmed that the values relative to PRESS are approximately twice as great as the ones relative to STEAM because of the inherent excitation pulses of the two sequences.

In addition, software RMS noise and Cr SNR calculations in STEAM and

STEAM concentrations (a.u.)					
	no. 1	**no. 2**	**no. 3**	**Mean**	**Ratio over Cr**
NAA	43	42	45	43 ± 2	1.54 ± 0.09
Cr	28	29	28	28 ± 1	1.00 ± 0.04
Cho	23	26	25	25 ± 2	0.89 ± 0.08
mI	13	13	14	13 ± 1	0.46 ± 0.04
H_2O	98 $\times 10^3$	98 $\times 10^3$	104 $\times 10^3$	(100 ± 4) $\times 10^3$	3600 ± 200
PRESS concentrations (a.u.)					
	no. 1	**no. 2**	**no. 3**	**Mean**	**Ratio over Cr**
NAA	86	88	85	86 ± 2	1.48 ± 0.04
Cr	59	57	57	58 ± 1	1.00 ± 0.02
Cho	46	49	46	47 ± 2	0.81 ± 004
mI	28	28	29	28 ± 1	0.48 ± 0.02
H_2O	192 $\times 10^3$	192 $\times 10^3$	179 $\times 10^3$	(187 ± 8) $\times 10^3$	3200 ± 200

Table 4.7: Compound concentrations with STEAM and PRESS automatically computed by GE workstation software and their mean values with their ratios over Cr.

PRESS spectra and their mean values are reported in Table 4.8.

STEAM and PRESS RMS noise calculations are practically the same because they are computed over a region of the spectrum where no metabolites are expected. Therefore, the sequence choice does not seem to influence the noise baseline.

On the other hand, it is evident that Cr SNR values approximately double up with PRESS. This is a further confirmation of the different excitation modalities provided by the two sequences, which lead to different signal intensities. The constance of the Cr SNR over time is considered to be an immediate index of the system stability and its performances.

STEAM				
	no. 1	**no. 2**	**no. 3**	**Mean**
RMS noise	1.08	1.06	1.08	1.07
Cr SNR	25.73	27.20	26.28	26.40
PRESS				
	no. 1	**no. 2**	**no. 3**	**Mean**
RMS noise	1.02	1.13	1.11	1.09
Cr SNR	54.48	50.77	51.72	53.32

Table 4.8: GE workstation software RMS noise and Cr SNR calculations in STEAM and PRESS spectra.

In conclusion, two of the acquired STEAM and PRESS spectra are reported in Figure 4.10, where it is possible to observe the lower noise in the PRESS spectrum baseline. Both images are rescaled by the workstation software.

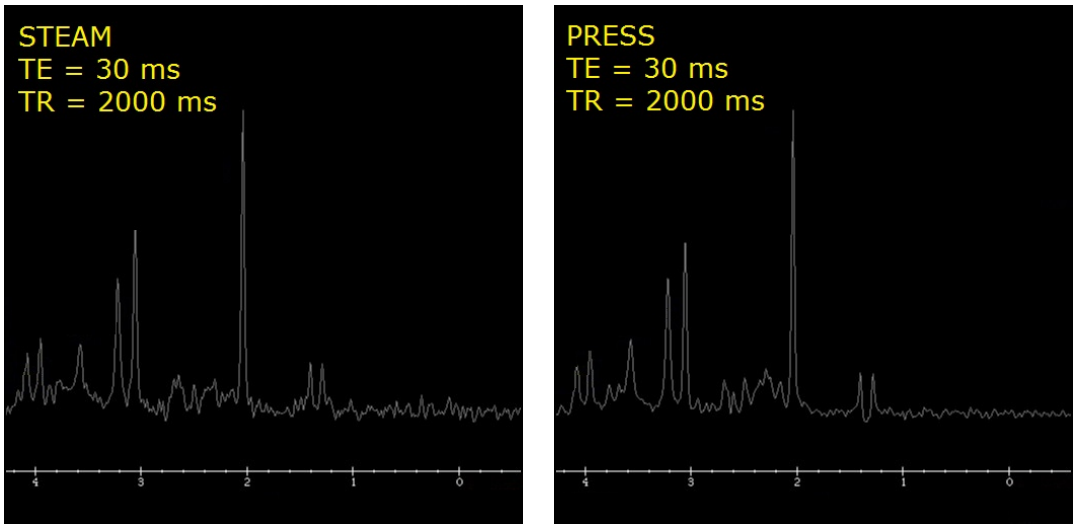

Figure 4.10: STEAM and PRESS spectra acquired during QA.

Chapter 5

Time-domain preprocessing and fitting algorithms

5.1 Time-domain quantification

5.1.1 Comparison of spectral analysis in the time domain and in the frequency domain

According to NMR principles, data analysis and interpretation can be performed both in the time domain and in the frequency domain since Fourier transform of the signal allows to establish a reversible correspondence from either field to the other. This thesis will focus on time-domain spectroscopic analysis, processing and quantification. Indeed, quantification refers to the disentanglement of time-domain signals in terms of relevant physical parameters such as frequency and amplitude. The accuracy and the robustness of the parametric estimation is of vital importance for diagnostic purposes.

Quantification in the frequency domain offers the possibility of selectively limiting the focus of the data analysis to a well-defined portion of the spectrum. Furthermore, no prior assumptions have to be made concerning the lineshape of the signal. Afterwards, quantification is accomplished by the integration of the area under the peaks of interest. This procedure requires no

prior assumption, but the disentanglement of overlapping peaks is prone to leading to unreliable results, especially when SNR is low or evident residual baseline signals appear in the spectrum. The definition of abrupt bounds to separate resonances tends to underestimate the relative area because tails below the peaks are neglected [56].

On the other hand, data quantification in the time domain, i.e. the same domain in which MRS signals are acquired, allows the interpretation of the MRS signal in terms of generic or exponentially decaying functions and its decomposition into its basis components [57]. Analysis in the time domain gives more flexibility to the model function and allows specific time-domain preprocessing in order to enhance the result extraction.

5.1.2 Quantification in the time domain

The interpretation of the MRS signal in the time domain requires the fitting of a mathematical function, i.e. the model function, to the data. There are two possible paths for quantification of MRS signals in the time domain:

- **noniterative methods**: they are based on applying the mathematical properties of the exponential decay model to the signal until convergence is reached. They are advantageous because they require no starting values, but the drawback is that they do not allow the exploitation of available prior knowledge regarding the model parameters. They require minimal human decisions in the process, thus reducing possible bias.

- **iterative methods**: they consist basically in the application of least square methods to the data via a number of iteration steps, which make these algorithms time-consuming. Available prior information can contribute to the signal quantification, although necessarily the starting values for the first iteration step must be provided by the user. Another benefit is that there is no limitation regarding the mathematical

shape of the model functions in principle.

Noniterative fitting methods require necessarily that the model function is replaced by an alternative function containing linear parameters. This is achieved by the Singular Value Decomposition (SVD) of the matrix containing the data points of the MRS time-domain signal.

The data analysis with iterative methods allows to directly manage the data points with the original model function. The objective is to minimize the difference between the data and the model function. Anyway, in general this implies the dealing with nonlinear least square fitting, which might lead to time-consuming calculations. Typically, incorporating prior knowledge provides better accuracy in quantification [56].

5.1.3 Introduction to the jMRUI software

The package used for data analysis is jMRUI (java Magnetic Resonance User Interface), which is a java-based software that allows MR spectroscopists to perform time-domain interpretation and quantification of MRS data. It is not open-source, but licenses are free for academia via registration on the website [58].

The project development was supported by the European Communities project "TMR/Networks ERB-FMRX-CT970160" and is presently supported by the European project "FAST - Research and Training Network, MRTN-CT-2006-035801". The main research contribution is provided by the D. Graveron-Demilly group at the Claude Bernard University Lyon 1 in France and Universitat Autónoma de Barcelona in Spain. The software version used in this thesis is the latest jMRUI-5.1.

The jMRUI package offers a wide range of preprocessing and quantification methods for MRS data analysis by commands defined by the user for the treatment of one or more signals at the same time. As an example, the visualization of spectral data files of a non-water-suppressed spectrum both in the time and frequency domain on jMRUI-5.1 time-series screen is reported in

Figure 5.1. The results of the processing are viewed in the frequency domain for an easier interpretation for the user thanks to Fourier transform.

In general, the jMRUI package provides several choices of computational methods for:

- frequency selective filtering of signals
- correction of eddy-current artifacts
- linear prediction
- nonlinear fitting in the time-domain
- quantum-mechanics simulation of spectra

More specifically, the software offers a wide range of quantification algorithms, the most relevant being [59]:

- **black box quantification algorithms** based on SVD: the most important is HLSVD, which is efficient for quantification of signals with good SNRs and characterized by unknown composition and shape, even though no prior assumption can be made.
- **nonlinear least square quantification algorithms**: the most renowned are AMARES and QUEST, which both enable to impose prior knowledge on the model-function parameters. AMARES demands starting values defined by the user, whereas QUEST uses a phantom or quantum-mechanically simulated metabolite set as a basis for in vivo quantification.

Data file conversion is available for the major medical MR spectrometer manufacturers, e.g. GE, Philips and Siemens, and for most of the biomedical research manufacturers, e.g. Varian and Bruker.

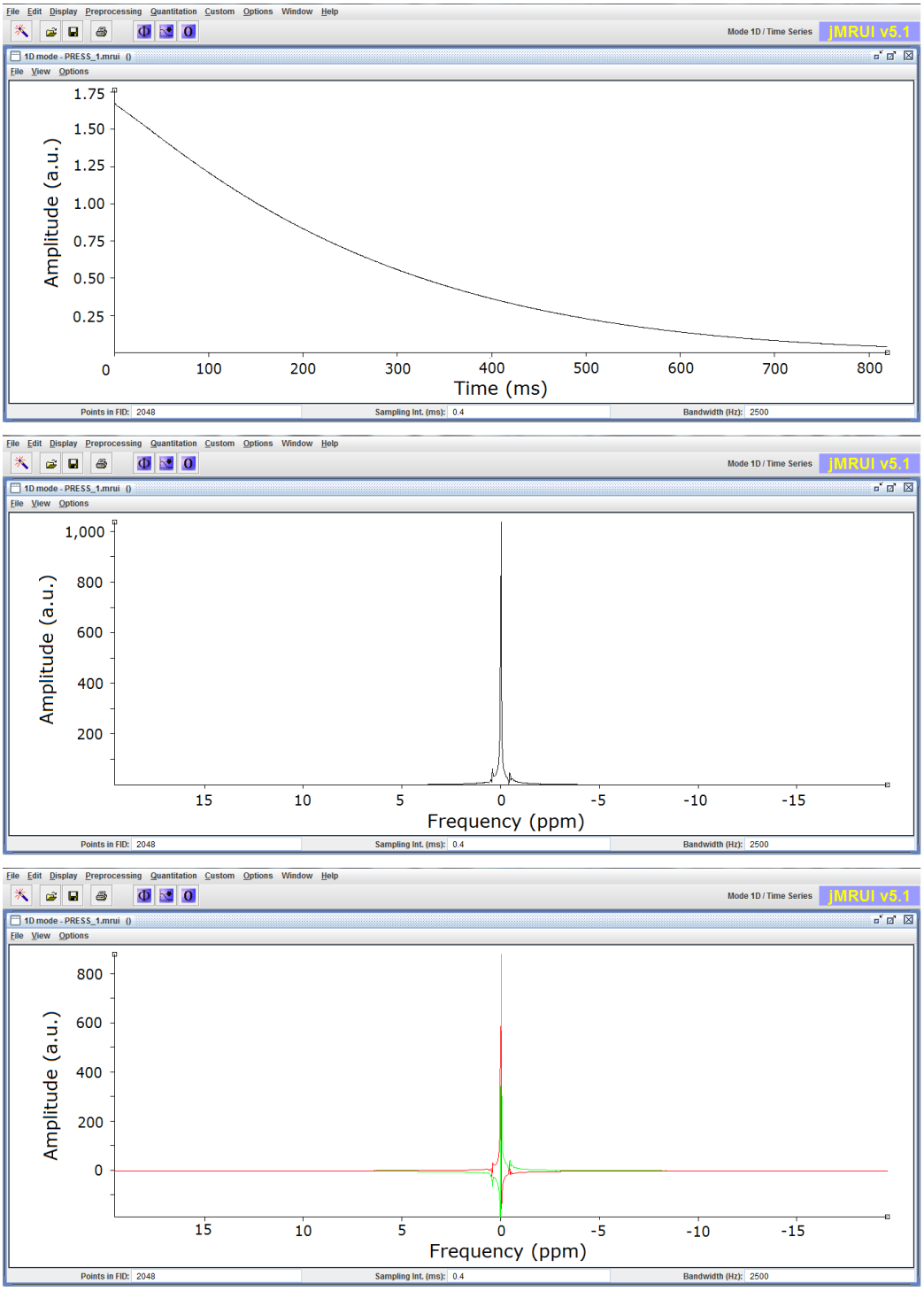

Figure 5.1: A water signal viewed in the time domain (top), in its absolute value (black) (middle)and in its real and imaginary components (red and green) (bottom) in the frequency domain on jMRUI-5.1 time-series screen.

5.2 A noniterative algorithm: HLSVD

5.2.1 Singular value decomposition of a Hankel matrix

HLSVD (Hankel Lanczos Singular Value Decomposition) is a black box quantification method which is based on the **singular value decomposition** of a Hankel matrix by the Lanczos algorithm [60]. It is a noniterative method which models data as following an exponentially damped sinusoidal trend. No starting values are required, but on the other hand no prior information is exploited.

Indeed, the data $\hat{x}_n$ $(n = 1, 2, ...N-1)$ are modelled as a sum of exponentially damped sinusoids:

$$\hat{x}_n = \sum_{k=1}^{K} c_k exp[(-\alpha_k + i\omega_k)t_n + i\phi_k] \tag{5.1}$$

with

$$t_n = n\Delta t \tag{5.2}$$

$$\alpha_k > 0 \tag{5.3}$$

and c_k, α_k, ω_k and ϕ_k $(k = 1, 2, ...K)$ being the intensity, the damping factor, the angular frequency and the phase of the kth sinusoid, respectively. It is worth mentioning that the damping of the acquired signal does not need to be exponential for adequate parametrization in principle, but quantification results are more reliable if the signal damping is approximately exponential.

Then, the points are arranged in a $L \times M$ data matrix X.

$$X = \begin{pmatrix} x_0 & x_1 & x_2 & \cdots & x_{M-1} \\ x_1 & x_2 & \cdots & & \vdots \\ x_2 & \cdots & \ddots & & \vdots \\ \vdots & & & \ddots & \vdots \\ x_{L-1} & \cdots & \cdots & \cdots & x_{N-1} \end{pmatrix} \tag{5.4}$$

with

$$L + M = N + 1 \tag{5.5}$$

All the elements on the antidiagonal of X are equal, a typical simmetry of a **Hankel matrix**. Thus, each matrix element is such that:

$$x_{i,j} = x_{i-1,j+1} \tag{5.6}$$

Consequently, the data matrix is decomposed into the product of three matrices:

$$X = \zeta_{LK} C \tilde{\zeta}_{MK} = \begin{pmatrix} 1 & \cdots & 1 \\ z_1^1 & \cdots & z_K^1 \\ \vdots & \ddots & \vdots \\ z_1^{L-1} & \cdots & z_K^{L-1} \end{pmatrix} \begin{pmatrix} c'_1 & \cdots & 0 \\ \vdots & \ddots & \vdots \\ 0 & \cdots & c'_K \end{pmatrix} \begin{pmatrix} 1 & z_1^1 & \cdots & z_1^{M-1} \\ \vdots & \vdots & \ddots & \vdots \\ 1 & z_K^1 & \cdots & z_K^{M-1} \end{pmatrix} \tag{5.7}$$

where

$$z_k = exp[(-\alpha_k + i\omega_k)t_k] \tag{5.8}$$

$$c'_k = c_k exp(i\phi) \tag{5.9}$$

ζ_{LK} and $\tilde{\zeta}_{MK}$ are **Vandermonde matrices**, i.e. they are matrices whose terms in each row or column are in geometric progression (the ratio of an element over the previous one is constant).

In order to achieve Vandermonde decomposition, the data matrix must be subjected to singular value decomposition (SVD). SVD decomposes the data matrix into the product of two unitary matrices U and V, whose columns are the left and right singular vectors, and a diagonal matrix Λ, whose entries on the diagonal are the singular values, which are exponentially damped sinusoids.

$$X_{L\times M} = U_{L\times L} \Lambda_{L\times M} V^{\dagger}_{M\times M} \tag{5.10}$$

The singular values above a certain threshold are signal-related, whereas the ones below are noise-related (they would be null if the signal were noiseless). Anyway, when noise-related singular values are discernible from the signal-related ones, the first are put to zero. ζ_{LK} must be transformed into U .

Once ζ_{LK} is given, the frequencies and the damping factors are known. The complex-valued amplitudes can be retrieved by fitting Equation to the data, i.e. each spectral component is expanded into a sum of exponentially damped sinusoids.

5.2.2 Application of the Lanczos algorithm to the Hankel matrix

The computational load of the SVD of a matrix is proportional to the third power of the size of the matrix. In order to reach a rapid solution, the **Lanczos algorithm** is applied. It is a method which searches for eigenvalues and eigenvectors of rectangular sparse matrices in SVD. The approach exploits the Hankel simmetry of the data matrix.

The complex-valued $L \times M$ data matrix $X = X' + iX''$ is reformulated as a real-valued square symmetric $2(L+M) \times 2(L+M)$ matrix B, defined as:

$$\begin{pmatrix} & O & & X' & X'' \\ & & & -X'' & X' \\ \tilde{X}' & -\tilde{X}'' & & & \\ \tilde{X}'' & \tilde{X}' & & O & \end{pmatrix} \tag{5.11}$$

The matrix B is converted to a diagonal matrix D by two othogonal matrices R.

$$B = RD\tilde{R} \tag{5.12}$$

The basic concept behind Lanczos algorithm is that B is converted into a tridiagonal matrix, i.e. with not null elements on the main diagonal and the first superior and inferior diagonal lines. The eigenvalue retrieval is restricted on the identification of the main eigenvalues representing the signal part, while discarding the lowest related to noise. This considerably reduces the computational burden of the Hankel matrix.

However, it is important to outline that the algorithms leads to successful results only when SNR is sufficiently high, since otherwise the algorithms

tends to produce erroneous results because of its difficulty in discerning and separating signal eigenvalues from noise content. This is due to the fact that no prior knowledge is provided in advance [57].

In addition, the algorithm might fail to reach an accurate quantification because of rapidly decaying signals, e.g. macromolecules for in vivo data. These signals are characterized by broad spectral lines because of their short T_2s which overlap with metabolite contributions in the frequency domain. Thus, it may be convenient to truncate part of the initial points of the FID to remove fast components despite some loss of information in the registered signal [60].

In conclusion, it is clear that HLSVD is a quantification algorithm suitable for the analysis of prominent peaks above the baseline in the spectrum. Otherwise, i.e. when SNR is low, the algorithm will not be able to adequately discern the signal from the noise.

5.3 An iterative algorithm: AMARES

5.3.1 Fitting of the nonlinear model function by least-mean-square method

AMARES (Advanced Method for Accurate, Robust and Efficient Spectral fitting) is quite a sophisticated method to estimate parameters of noisy MRS signals in the time domain. In fact, simple numerical integration of the area below the resonance peak in the frequency domain is highly likely to lead to erroneous outcomes, especially if SNR of peaks is low. On the contrary, AMARES is a more appropriate choice for spectra characterized by low SNRs, strong overlapping components or large background signals.

The algorithm fits the data to the nonlinear model function by the least-mean-square method for **maximum likelihood parameter estimation**. Therefore, it basically consists in a function optimization problem. The accuracy and robustness of the algorithm are determined by the possibility

of imposing prior knowledge [61].

The robustness is increased by imposing lower and upper bounds on the parameters. Additionally, prior knowledge leads to a more accurate estimation because all available information and flexibility for the user are included in the quantification.

5.3.2 Maximum likelihood estimates

The initial assumption of the maximum likelihood (ML) method is that a joint probability density function (pdf) for all data points in the time domain can be defined for an accurate modeling [57]. For instance, supposing that the data do not considerably deviate from a Gaussian trend, the joint pdf can be expressed as:

$$p(\mathbf{x}, \sigma, \mathbf{p}) = \prod_{n=0}^{N-1} \sqrt{\frac{1}{2\pi\sigma_n^2}} \exp[-\frac{\{x_n - \hat{x}_n(\mathbf{p})\}^2}{2\sigma_n^2}] \tag{5.13}$$

where $\mathbf{s}$ is the vector of the time-domain data points, $\sigma = (\sigma_1, \sigma_2, ...\sigma_n)$ is the vector of the noise standard deviations, $\hat{x}_n(\mathbf{p})$ is the model function value to be fitted and $\mathbf{p}$ is a vector containing the model function parameters.

Indeed, in the AMARES algorithm two functionals must be minimized in order to obtain maximum likelihood estimates for data expressed as a sum of exponentially damped sinusoids. The first one, G is derived using probability theory:

$$G(\mathbf{c}, \alpha, \omega, \phi) = \sum_{n=0}^{N-1} \left| y_n - \sum_{k=1}^{K} c_k exp[(-\alpha_k + i\omega_k)t_n + i\phi_k] \right|^2 = \\ = \|\mathbf{y} - \Psi\mathbf{l}\|^2 \tag{5.14}$$

where $\mathbf{c}$, α, ω, ϕ are the vectors of amplitudes, dampings, frequencies and phases, respectively, and

$$\mathbf{y} = [y_0, \cdots, y_{N-1}]^T \tag{5.15}$$

is the signal vector,

$$\mathbf{l} = [a_1 e^{i\phi_1}, \cdots, a_K e^{i\phi_K}]^T \tag{5.16}$$

is the vextor containg phase-modulated amplitudes and

$$\Psi = \begin{pmatrix} e^{(-\alpha_1+i\omega_1)t_0} & \dots & e^{(-\alpha_K+i\omega_K)t_0} \\ \vdots & \ddots & \vdots \\ e^{(-\alpha_1+i\omega_1)t_{N-1}} & \dots & e^{(-\alpha_K+i\omega_K)t_{N-1}} \end{pmatrix} \tag{5.17}$$

is a $N \times K$ full-rank matrix.

The second functional V is derived under the assumption that nonlinear parameters ω and α are known. Then, the estimate for the linear parameters $\mathbf{l}$ can be obtained by solving a linear least-square (LS) problem:

$$\hat{\mathbf{l}} = \Psi^{\dagger}\mathbf{y} \tag{5.18}$$

with

$$\Psi^{\dagger} = (\Psi^T\Psi)^{-1}\Psi^T \tag{5.19}$$

being the pseudo-inverse of Ψ. Substituting Equation 5.18 into the expression of the first functional 5.14 leads to:

$$V(\alpha, \omega, t_0) = \left\|\mathbf{y} - \Psi\Psi^{\dagger}\mathbf{y}\right\|^2 \tag{5.20}$$

which is the variable projection functional. The dependence on $\mathbf{c}$ and ϕ is eliminated, thus reducing the number of variables involved in the minimization problem.

It is clear that both functionals G and V consist of the sum of squared residuals within a nonlinear LS problem. The main disadvantage of formulating the calculation in these terms is the poor computational efficiency of global optimization, which inevitably makes the algorithm time-consuming.

5.3.3 Prior knowledge in AMARES

The basic stratagem to reach convergence in a reasonable amount of time is to operatively choose the starting values by **peak picking** for local optimization purposes. This selection implies that prior knowledge on amplitudes and phases is provided by the user. This step is fundamental in the resolution of LS problem in 5.18 with the starting values being inserted in $\Psi^{\dagger}$.

However, it should be outlined that peak peaking might fail when several peaks are overlapping. This may be a problem for quantification of complex short echo-time spectra.

Peaks referring to the same biomolecule multiplet are separately picked at first (according to a singlet approach), but they can be put into one group afterwards imposing constraints on their relative ratios. Amplitudes cannot become negative (i.e. corresponding to a 180° phase shift), while the upper and lower bounds on frequencies are determined by the spectral width. AMARES is able to fit both FIDs and echoes, which is modeled as two FIDs, one of which is considered as reflected backwards.

By imposing such user definition for the estimate of peak-related parameters, it is possible to accurately quantify resonances within a low-noise spectrum, which would be erroneously interpreted by noniterative methods such as HLSVD. Furthermore, by defining a second functional V, which takes into account prior knowledge while discarding some linear parameters, the optimization problem is less time-consuming and results in increased accuracy and user flexibility.

Chapter 6

Analyses of the water peak

6.1 Quantification of the water peak and experimental settings

6.1.1 The usefulness of non-water-suppressed spectra

Metabolite peaks of interest in clinical routines would not be detectable in the spectrum, if the prominent water peak had not been suppressed in advance because of its overall distortion of the baseline. Hence, water suppression becomes a fundamental preliminary step for an accurate and reliable observation of the metabolite peaks.

Anyway, the analysis of the water resonance is of utmost importance as a reference for evaluations such as concentration calculations, monitoring of the overall magnetic field homogeneity in the area under examination and the detection of possible eddy currents.

For instance, when multi-channel coils are used, the unsuppressed water peak is a reference for aligning the phases and the weighting of the signals originating from different coil elements. Indeed, if one of the metabolite peaks were used as reference for phase alignment, the results would be unreliable because of its relative low SNR in comparison with the water resonance. Phase alignment based on the residual water in water-suppressed spectra

would lead to inaccurate results, too [62].

Consequently, the best conditions for evaluation of these parameters are provided by non-water-suppressed spectra. The high SNR of the water peak guarantees the most reliable quantification parameters to assess the suited operative conditions in which MRS can be performed.

6.1.2 Experimental settings and parameters

Single-voxel spectra have been acquired using GE classic quad head coil no.2384268 and GE spherical phantom. The phantom has been centred within the coil by laser focusing on its base guidelines for an accurate positioning at the isocentre of the scanner. The phantom had been left in advance in the magnet room to ensure that it would have been at the thermal equilibrium with the environment. The recorded temperature of was 22°C and therefore the water peak is expected to be centred around 4.85 ppm.

Spectra have been acquired using voxels of varying dimensions, at different locations and at varying TEs. The experimental parameters listed in Table 6.1 have been kept fixed for all the acquisitions.

Parameter	
TR	4000 ms
Number of averages	32
Phase cycling	8
R1	13
R2	30
TG	182
Number of samples	2048
Sampling rate	0.4 ms
Bandwidth	2.5 kHz

Table 6.1: Fixed parameters for single-voxel acquisitions of water spectra.

It should be outlined that the TR selection allows only partial T_1 relaxation recovery. However, this particular choice is coherent with TR values used in clinical routines. The receiver gains R1 and R2 are tuned to their maximum values in order to obtain the maximum amplification of the signal, bearing in mind that the receiver dynamic range is wide enough to avoid signal saturation in the electronic components. The bandwidth is automatically adjusted by the workstation software.

6.1.3 Quantification operations and error estimation

Non-water-suppressed spectral quantifications have been computed by HLSVD algorithm, which has been discussed in Chapter 5. This choice is coherent with the suitability of the algorithm for parameter extraction for prominent peaks in the spectrum easily distinguishable from the noise baseline.

Preprocessing steps include phase correction in relation to the water peak to remove possible distortion due to inhomogeneities induced by eddy currents and normalization to a reference value.

HLSVD quantification has been launched by choosing one component to be found. The results provided measurements of peak centre frequency, amplitude, linewidth, phase and noise. The original and the estimated spectra together with the searched component and the residue calculated as the difference between the original and the estimated signals are reported in the HLSVD result window (as depicted in Figure 6.1). The noise in the residue is calculated over the last 204 sample points of the FID, corresponding to 10% of the sampled signal duration.

The algorithm provided errors in the measured parameters relating to the degree of accuracy of a certain component. Precisely, they consist in the **Cramer-Rao Lower Bounds** (CRLBs) on the statical errors of the estimated model function parameters [63]. According to the Minimum Variance Bound (MVB) theory, these are lower bounds on the precision and accuracy of spectral parameters which cannot be superseded.

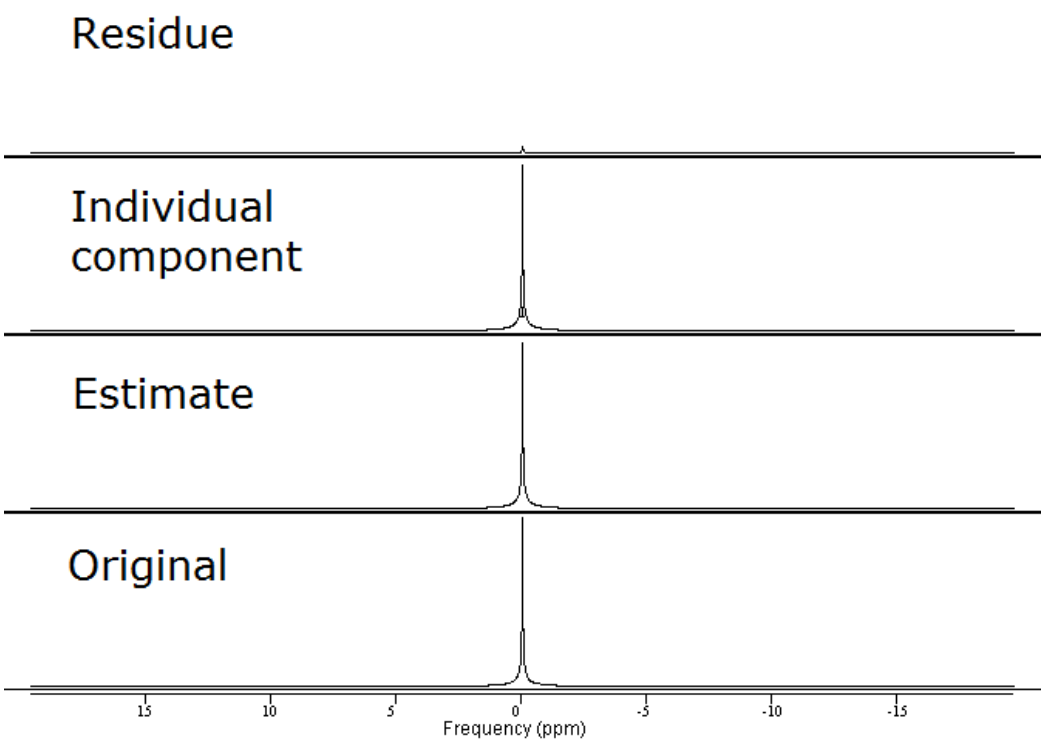

Figure 6.1: From bottom to top: Original, estimated, individual components and residue spectra viewed on the HLSVD result window over a non-water-suppressed spectrum.

It is worth mentioning that these outcomes are regardless of the specific quantification method being used, with the nontrivial assumption that it is unbiased. Then, CRLBs become a standard of precision for comparison. More importantly, they are independent on whether time-domain or frequency-domain algorithms are applied, allowing the possibility of comparing results computed in the two domains in terms of accuracy. The determining factors which influnce CRLBs are the noise level, the number of data points and the sampling rate, which are inherently related to the quality of the acquired data [57].

For CRLB estimation, the data x_n are modeled as sums of exponential factors containing amplitudes c_k, damping factor α_k, frequency ω_k, phase ϕ_k

and a complex Gaussian distributed noise component ϵ_n:

$$x_n = \sum_{k=1}^{K} c_k \cos[(-\alpha_k+\omega_k)t_n+\phi_k]+\Re\epsilon_n+i(\sum_{k=1}^{K} c_k \sin[(-\alpha_k+\omega_k)t_n+\phi_k]+\Im\epsilon_n) \tag{6.1}$$

Then, assuming that the model function can describe the signal in absence of noise, the noise-free signal becomes:

$$g_n = x_n - \epsilon_n \tag{6.2}$$

Therefore, the following step is the definition of the Gaussian pdf for a vector $\Theta = (\theta_1, \theta_2, ..., \theta_i)$ containing the parameters for each data point:

$$p(x, \Theta) = \prod_{n=1}^{N} \frac{1}{\sqrt{2\pi\sigma_n^2}} e^{-\frac{1}{2\sigma_n^2}\{[\Re(x_n)-\Re(g_n)]^2+[\Im(x_n)-\Im(g_n)]^2\}} \tag{6.3}$$

The pdf is included in the **Fischer information matrix** $F(\Theta)$ defined as the expectation value E of the partial second derivative of the log-like pdf over the parameter vectors Θ_i and Θ_j.

$$F(\Theta) = -E[\frac{\partial^2 \ln p(x, \Theta)}{\partial\Theta_i \partial\Theta_j}] \tag{6.4}$$

In conclusion, CRLBs of parameter θ_i are computed as the inverse of the corresponding Fischer matrix element [64]:

$$CRLB(\theta_i) = \sqrt{F(\Theta)^{-1}_{i,i}} \tag{6.5}$$

This is the lower achievable bound for the error estimation accuracy for the specific parameter.

Precisely, assuming the correctness of the model function and given the noise level, this defines a minimum for the variance for the estimated parameter:

$$\sigma^2(\theta_i) \geq CRLB(\theta_i) \tag{6.6}$$

Therefore, the theoretical lowest standard deviation of a particular parameter becomes:

$$\sigma(\theta_i) \geq \sqrt{CRLB(\theta_i)} \tag{6.7}$$

The latter is the expression used for the error assignment to the parameters quantified by the HLSVD algorithm over the water peaks [65]. However, it is important to stress that this is only a lower bound for errors.

6.2 Results of quantification of spectra without water suppression

6.2.1 Signal response for VOIs at different positions

MRS acquisitions using PRESS sequence without CHESS water suppression have been performed to evaluate the results moving the VOI position within the phantom. A VOI with $20 \times 20 \times 20$ mm^3 has been placed at the centre of the phantom and a PRESS sequence with TE = 30 ms has been applied.

Subsequently, PRESS has been performed with the same parameters but the position. The VOI has been moved 4 cm along the right half-axis and along the posterior half-axis in the axial image. The three selected VOIs are depicted in Figure 6.2. These measurements have been performed to evaluate the spectra acquired along the magnet axes with the assumption of the overall simmetry of the field homogeneity along the two directions, which had been suggested by the QA measurements reported in Chapter 4.

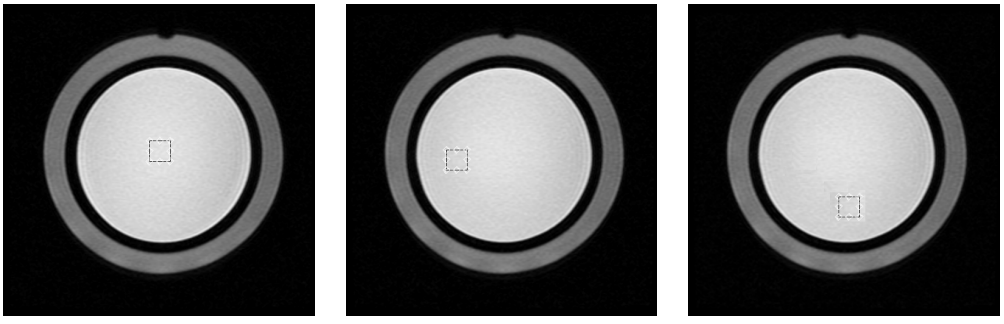

Figure 6.2: VOIs selected at different locations in the axial image.

The results of HLSDV quantifications contain CRLB values that are min-

imum values for errors. Therefore, it is recommendable to take into account greater uncertainties regarding the parameters because of the noniterative calculations by HLSVD (as it is expressed by Equation 6.7). The results of HLSVD calculations are listed in Table 6.2. The errors are deduced from the software calculations and not from repeated measurements.

VOI location	**Amplitude (a.u.)**	**Linewidth (Hz)**	**Phase (°)**
centre	1.75 ± 0.02	1.33 ± 0.02	40.8 ± 0.2
+ 4 cm right half-axis	1.78 ± 0.01	4.56 ± 0.01	18.1 ± 0.1
+ 4 cm posterior half-axis	1.80 ± 0.01	4.55 ± 0.01	19.0 ± 0.1

Table 6.2: HLSVD results for spectra acquired at different VOI positions.

The heights of the peaks are not relevant for HLSVD quantitation, however they are reported in Table 6.3 because of an interesting decrease when moving from the centre.

VOI location	**Peak height (a.u.)**
centre	1.032×10^3
+ 4 cm right half-axis	2.763×10^2
+ 4 cm posterior half-axis	2.807×10^2

Table 6.3: Peak heights for spectra at different VOI position.

The outcomes listed in Table 6.2 display greater values for linewidths of spectra acquired along the axes of about a factor of 4 because of the broadening of the area below the peak. Taking into account values in Table 6.3, a reduction in the height of the peak of a factor of 4 is parallel to the previous increment.

These effects might be caused by slight inhomogeneities in the sensitive volume, which go undetected in the MRI images acquired during QA measurements. This is because MRS acquisitions are particularly sensitive to

fluctuations in the homogeneity of the magnetic field, which may hamper the optimal slice selection needed for spectral quality. **High frequency resolution** is essential in MRS since chemical shifts between peaks and J coupling constants are small and strongly overlapping peaks lead to inaccurate quantification results. Therefore, the scanner shimming might be sufficient to provide the homogeneity needed for MRI but not as adequate as for MRS, implying the manual adjustment of shimming [66].

While this is not a problem for the water peak because of its high SNR in relation to metabolites, it might be an issue in clinical practice when considering low signals from metabolites not easily distinguishable from the noise baseline. In addition, line broadening also implies that water suppression is even more difficult to achieve successfully.

Considering the difference between the linewidth at the central VOI, located at the isocentre of the magnet, and the values of the VOIs 4 cm shifted along the axes, both reported in Table 6.2, and Equation 1.31, it is possible to approximately estimate that there is a discrepacy of 3.22 Hz, corresponding to an inhomogeneity of about 0.05 ppm in the magnetic field.

Another possible reason may be the unwanted signal contribution from regions outside the VOI. Anyway, the first hypothesis is more likely since this behaviour would be observed in regions where other strong signals, e.g. lipids, absent in the phantom, compete with water. This would lead to spurious signals detected in the spectrum and no reliable identification would be allowed.

Considering the phase, ideally MRS spectra should have zero-phase. However, phase displacements between the signal phase and the receiver phase are present because of the time delay between excitation and detection. The phase values reported in Table 6.2 correspond to water signal phase. It is possible to correct them by methods based on the multiplication of the FID for an exponential phase factor. However, the phase of the spectra has not been modified in order not to alter the begin time of the acquired signal. In fact, while it is essential that signals are zero-phased for quantification by

peak integration in the frequency domain, the spectrum does not need to have null phase to retrieve accurate quantities in the time domain thanks to the inherent robustness of the algorithms.

6.2.2 Quantification of the water peak at increasing VOI dimensions

Water peak spectra have been acquired with selection of VOIs of greater dimensions located at the centre of the phantom while keeping TE fixed to 30 ms. The selected sides of the VOIs have been varied from 10 mm to 30 mm by 5 mm steps. The expected behaviour is the linear increase of the amplitude below the peak coherently with NMR principles regarding the statistical increase of the signal when exciting a greater number of protons.

Therefore, HLSVD algorithm has been applied to the acquired spectra with varying volume dimensions. The measured results of HLSVD are reported in Table 6.4. However, once again the uncertainty regarding the computed quantities needs to take into account the errors from the other parameters which are involved in SVD decomposition.

Additionally, the HLSVD quantification results have been plotted in Figure 6.3.

The trend in Figure 6.3 is coherent with the expected linear increase of the peak amplitude at increasing VOI dimensions. This implies that spectra acquired with greater selected voxels will be characterized by greater areas below the peaks.

Then, the fitted equation for amplitude in function of the selected volume V has been fitted by the method of the weighted least squares [67]:

$$A(V) = (2.22 \times 10^{-4} V + 0.12) \text{ a.u.} \tag{6.8}$$

with the interpolated amplitude $A(0)$ and the slope m being:

$$A(0) = (0.12 \pm 0.01) \text{ a.u.} \tag{6.9}$$

$$m = (2.22 \pm 0.01) \times \ 10^{-4} \tag{6.10}$$

VOI dimensions (mm^3)	**Amplitude (a.u.)**	**Linewidth (Hz)**	**Phase** (°)
10 × 10 × 10	0.45 ± 0.02	1.19 ± 0.02	14.4 ± 0.2
15 × 15 × 15	0.75 ± 0.03	1.23 ± 0.03	33.1 ± 0.3
20 × 20 × 20	1.75 ± 0.02	1.33 ± 0.02	40.8 ± 0.2
25 × 25 × 25	3.59 ± 0.02	1.55 ± 0.02	54.3 ± 0.2
30 × 30 × 30	6.19 ± 0.03	1.83 ± 0.03	21.5 ± 0.2

Table 6.4: HLSVD results for spectra with greater dimensions for VOIs.

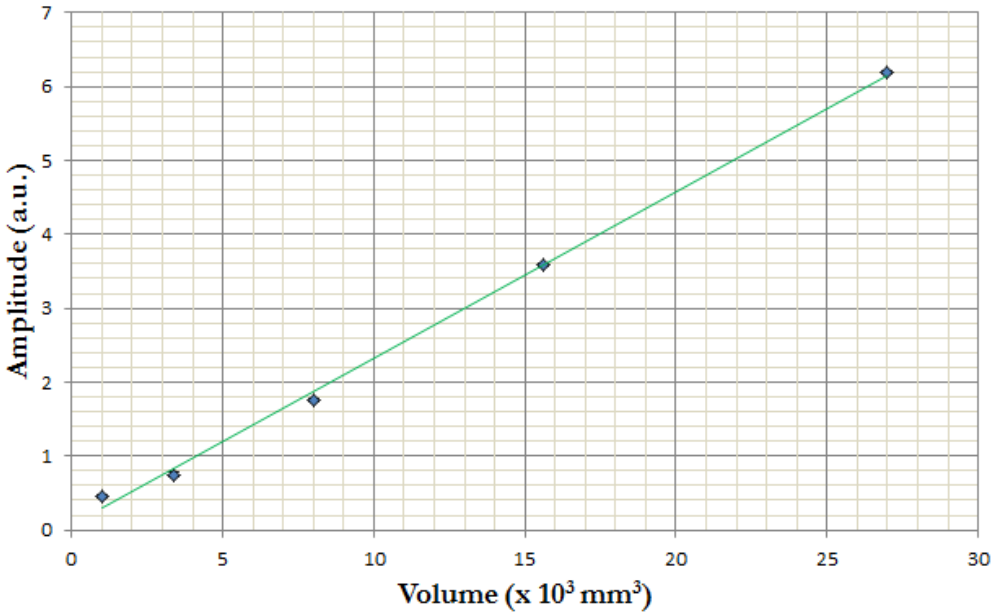

Figure 6.3: Amplitude linear trend at increasing VOI dimensions.

The calculated Pearson's product-moment correlation coefficient is the following:

$$R = 0.998 \tag{6.11}$$

thus indicating good linear correlation between two variables.

Because of the statistical increase of the signal when exciting a greater VOI, the increase in the water peak linewidth l is expected, too. The values for linewidth listed in Table 6.4 are plotted against volume in Figure 6.4.

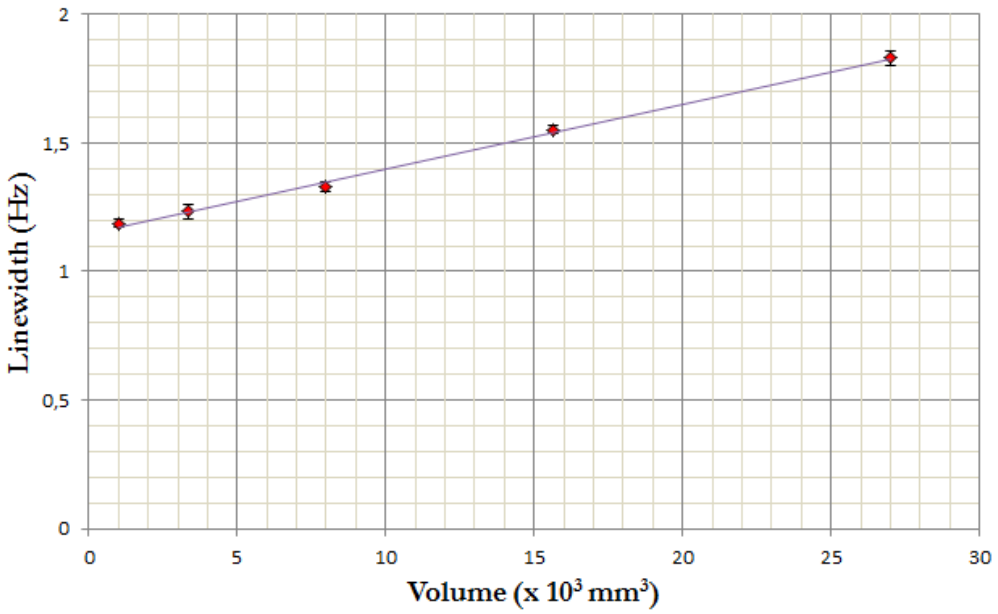

Figure 6.4: Linear trend of the water peak linewidth at increasing VOI dimensions.

The interpolated linewidth is expressed as a function of the volume by the following equation:

$$l(V) = (1.15 + 2.5 \times 10^{-5} V) \text{ Hz} \tag{6.12}$$

The intercept $l(0)$ and the slope m calculated by the method of the weighted least square are:

$$l(0) = (1.15 \pm 0.01) \text{ Hz} \tag{6.13}$$

$$m = (2.5 \pm 0.1) \times \ 10^{-5} \tag{6.14}$$

where $l(0)$ is the interpolated linewidth of the water peak at TE = 0 and m is an indicative factor of the slow increase of the linewidth in function of the selected VOI dimensions. The Pearson's correlation coefficient is:

$$R = 0.998 \tag{6.15}$$

thus indicating good linear dependence between the two variables.

In conclusion, it is worth mentioning that the selected volume dimensions for this study are the ones which are typically used in single-voxel spectroscopy. Selection of considerably greater VOIs is not performed in brain MRS because the examination results would lack specificity and accuracy since different tissues would be included within the voxel.

6.2.3 Quantification of the water peak at varying TEs and T_2 relaxation time extrapolation

The registered intensity of MRS signals is expected to decay exponentially or more often multi-exponentially when greater values for TEs are selected. Therefore, spectra have been acquired at varying TEs while keeping a 20 × 20 × 20 VOI at the centre of the phantom. Selected values for TEs are 30 ms, 100 ms, 150 ms, 300 ms and 400 ms.

HLSVD quantification has been performed over the acquired spectra. The results of this algorithm are listed in Table 6.5.

The results for HLSVD amplitude calculations have been fitted to an exponential curve in Figure 6.5 modeled upon the spin-echo sequence.

As it is observable in Figure 6.5, the amplitude of the water peak decays with the increase of TE, since the signal is given more time to progressively decay before its detection. The gradual coherence loss of spin due to fluctuations in the magnetic field would imply that the signal decays according to

TE (ms)	**Amplitude (a.u.)**	**Linewidth (Hz)**	**Phase (°)**
30	1.75 ± 0.02	1.33 ± 0.02	40.8 ± 0.2
100	1.43 ± 0.03	1.48 ± 0.03	22.2 ± 0.3
150	1.25 ± 0.03	1.28 ± 0.03	24.6 ± 0.3
300	0.73 ± 0.03	1.51 ± 0.03	16.3 ± 0.4
400	0.58 ± 0.02	1.37 ± 0.02	25.8 ± 0.2

Table 6.5: HLSVD results for spectra acquired at different TE values.

T_2^* constant. Indeed, considering that the relaxation time is measured from the echo, in principle it is possible to remove the coherence loss from the signal that can be approximately defined as:

$$S(t) \simeq S(0)e^{-\frac{t}{T_2}} \tag{6.16}$$

The fitted equation for amplitude dependent on TE is modeled accordingly (TE in ms):

$$A(\mathrm{TE}) = (1.93e^{-0.0031\cdot \mathrm{TE}}) \text{ a.u.} \tag{6.17}$$

with

$$R = -0.996 \tag{6.18}$$

indicating good statistical agreement of the data with the negative linear correlation.

The intercept of the line corresponds to the amplitude of the water peak at TE = 0. The result obtained by fitting the data by the method of the weighted least squares is the following:

$$A(0) = (1.93 \pm 0.09) \text{ a.u.} \tag{6.19}$$

The coefficient in the exponential is assumed to be the reciprocal of T_2 of the water signal. Consequently, the expression for T_2 becomes:

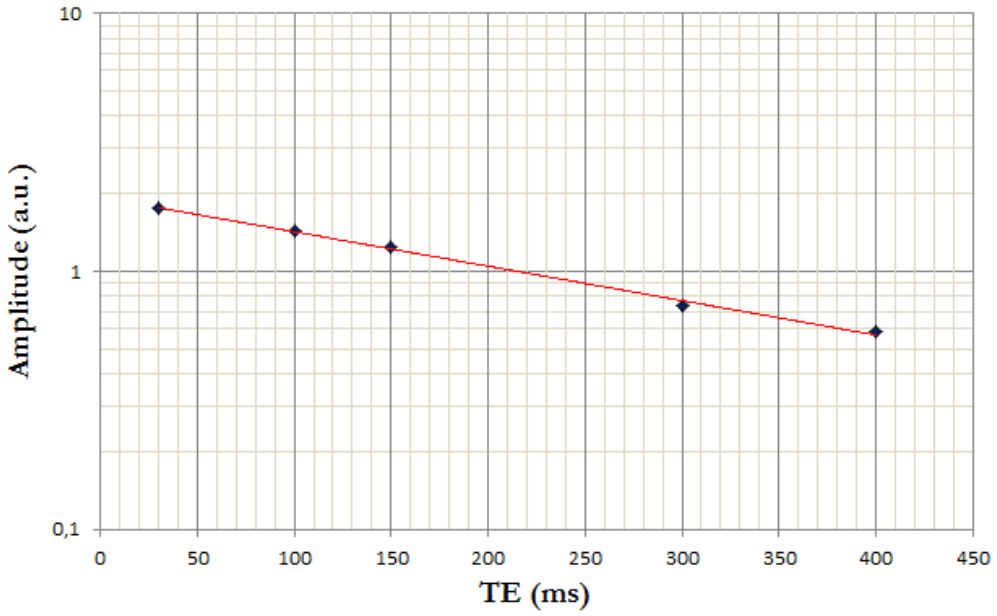

Figure 6.5: Amplitude exponential decay of the water peak in function of TE.

$$T_2 = TE \ln \frac{A(TE)}{A(0)} \tag{6.20}$$

The fitted value for T_2 of water is:

$$T_2 = (320 \pm 30)\text{ms} \tag{6.21}$$

Such a short T_2 value for water is caused by the influence of the paramagnetic agents which the phantom is filled with to emulate the magnetic susceptibility discontinuities and confinement conditions for water in tissues. Indeed, these effects cause the damping of the relaxation times because spin dephasing is enhanced. However, it should be mentioned that this is only an approximate calculation because signal effects due to partial T_1 recovery for water are not taken into account.

Chapter 7

Quantification of metabolite spectra

7.1 Residual water peak removal from the metabolite spectrum

7.1.1 HLSVD peak remover

A major concern for the quality of the acquired spectra is the presence of prominent and broad resonance peaks originated by strong signals from water, macromolecules or lipids which shadow the metabolites of interest and may alter the baseline. It is a preliminary requisite for the identification of the main metabolites to suppress these overbearing signals from the spectrum. However, it should be mentioned that the achievable accuracy of suppression methods do not permit the complete elimination of such strong contibutions from the signal. Therefore, several algorithms have been proposed to remove residual signals.

HLSVD peak remover is an algorithm based on SVD which processes the signal in order to remove the unwanted residual components [68]. The key parameters involved in HLSVD peak remover are the number of exponentially damped sinusoids and the size of data sets for fitting the signal without

residual water.

Indeed, the elimination of the residual water resonance is a complex task since it is not easy to suppress it without altering the low-noise metabolite peaks. Most of the postacquisition removal methods are based on bandpass filtering or on the subtraction of the signal from the FID by decomposition computations. Frequency-domain techniques do remove the water peak from the spectrum. Anyway, they might cause further distortion for the closest metabolite peaks.

Being based on single-value decomposition, HLSVD peak remover moves from the modeling of the signal as a sum of exponentially damped sinusoids. In particular, the model FID is described as a linear combination of signals of water, metabolites and Gaussian distributed noise ϵ:

$$FID_{model} = \alpha \times FID_{water} + \beta \times FID_{metabolite} + \epsilon \tag{7.1}$$

where α and β are amplitude factors for the residual water and the metabolite contributions respectively.

HLSVD peak remover eliminates the residual water signal by selecting the exponentially damped sinusoids whose frequencies are located in the water region and subtracting them from the original FID. Afterwards, the reconstructed FID is processed by Fourier transform and is ready for quantitative analysis.

$$FID_{reconstructed} = FID_{model} - FID_{water/HLSVD} \tag{7.2}$$

where $FID_{water/HLSVD}$ indicates the residual water signal reconstructed by the HLSVD method. Indeed, even though the residual water is still a prominent peak in the spectrum, HLSVD is an algorithm which is robust enough to distinguish it from the noise baseline.

7.1.2 Effects of the removal of the water peak from the metabolite spectrum

The main residual peak in proton MRS distorts the metabolites signals and alters the spectral baseline because of its long tails. It should be mentioned that its removal is a compromise between the reduction of the amplitudes of the metabolites close to water and the permanence of further residual water.

HLSVD peak remover has been applied on the metabolite spectra acquired during QA, which have been already presented in Chapter 4. The region boundaries selected for residual water peak removal have been located at 0.5 ppm from the water peak centre on both sides. Therefore, the 1 ppm frequency region approximately corresponds to the elimination of a window of 63.4 Hz. The residual water amplitude contained within this region is about 2 orders of magnitude greater than metabolite amplitudes.

The effects of the preprocessing steps on the spectrum are depicted In Figure 7.1. The spectrum before the residual removal and after the processing together with the selected frequency region are depicted. Since jMRUI automatically sets the zero frequency at the location of the highest peak, this value has been shifted to the reference resonance frequency of TMS to guarantee the easy identification of the resonance frequencies of the metabolites and comparison with the workstation screen. The setted shift value is 4.85 ppm, which is the water resonance position at 22°C, i.e. the temperature of the phantom at thermal equilibrium with the magnet room when the experiments have been carried out. This permits the correct alignment of the metabolites referring to the experimental conditions.

Considering the effects of HLSVD peak remover on the spectrum, depicted in Figure 5.1, no distortion of the baseline nor the alteration of the close metabolite peaks are evident. Anyway, water residual components are still present in the region between the 6 ppm and 4 ppm frequencies in the spectrum. Metabolite peaks belonging to this region cannot be used for quantification.

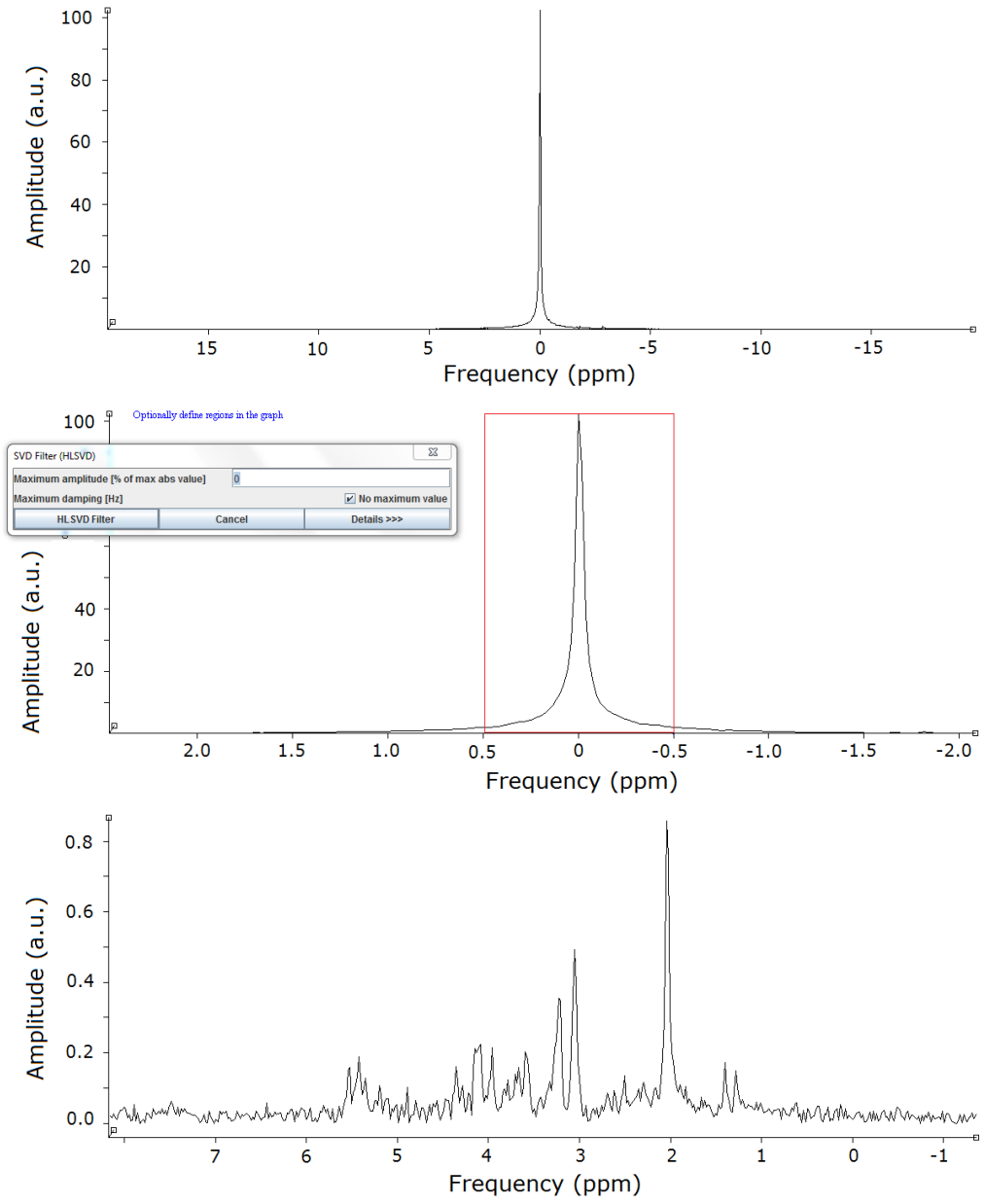

Figure 7.1: jMRUI screen views of the spectrum before the application of HLSVD peak remover (top), the zoomed selected frequency region for elimination (middle) and the spectrum after the processing and the shifting of the reference zero frequency (bottom).

7.2 Quantification of metabolite amplitudes by AMARES

7.2.1 Peak picking on the spectrum

Probably the main obstacles to overcome in proton spectroscopy performed at short TEs on humans are the identification and the quantification of individual metabolites in the spectra. This difficulty is caused by the presence of several unresolved multiplets characterized by complex lineshapes and remarkable spectral overlap, especially when acquisitions are performed at the lower static field strengths which are available for clinical examinations. Selecting greater TE values would lead to the disappearance of interesting peaks with short relaxation times and to a considerable reduction in SNR, although also unwanted peaks disappear in the spectrum.

In comparison to black-box quantification methods, AMARES is a more suitable choice for parameter estimation in metabolite spectra, since its iterative calculations permit to disentangle peaks comparable to noise in spectra with strong overlapping components and large background signal [63].

Therefore, it is of utmost importance to include a priori information regarding the compounds of interest to facilitate quantification of parameters. Chemical shift information alone is insufficient for accurate metabolite detection. Further prior knowledge of the multiplicity, the coupling constants and the chemical group associated with the peaks enable to clearly identify the metabolites whose resonances are observed in the spectrum [69]. These pieces of information allow the retrieval of reliable quantification parameters despite possible fluctuations in the chemical shifts due to pH of the surroundings and temperature.

This is of particular importance in chemical groups giving rise to multiple resonances, which are characterized by fixed frequency separation and relative amplitude ratios among peaks thanks to J coupling. Indeed, it is possible to accurately quantify peaks belonging to multiplets by imposing

their relative amplitude ratios before the application of the algorithm.

7.2.2 Metabolite amplitude quantification settings and operations

It is an interesting approach for the evaluation of the good performance of the quantification operations to compare the ratios of the metabolite amplitudes over the creatine calculated by the workstation software over the processed QA spectra and by the fitting algorithm. The quantification of metabolite amplitudes has been performed by the AMARES algorithm, which is capable of retrieving information in low-SNR spectra.

It is important to point out that quantification results from not zero-phased spectra, e.g. by peak integration in the frequency domain, would not be reliable nor accurate. On the other hand, this is not a matter of issue for fitting algorithms in the time domain.

The experimental parameters for acquisitions of metabolite spectra are reported in Table 7.1. It is worth mentioning that embedded within GE ProbeP and ProbeS sequences there are default non-water-suppressed excitations acquired with the same parameters as metabolite spectra but the number of averageres, which is 16. These are needed for the workstation quantification of the water content within the selected VOI.

The metabolite spectra acquired during Qa are affected by a great amount of noise in the baseline. This is due to the low number of averages and the short TR value used for acquisition. Consequently, they have been submitted to **Gaussian apodization** in order to broaden the peak linewidth and reduce the amount of noise in the baseline.

The software tool for apodization consists in the multiplication of the acquired FID by an exponentially decaying function which makes the signal decay faster to zero. The jMRUI Gaussian apodization function w_{Gauss} for the FID has the following expression:

$$w_{Gauss} = e^{-i\frac{g^2(\Delta t)^2}{2}} \tag{7.3}$$

Parameter	
TE	30 ms
TR	2000 ms
Number of averages	32
Phase cycling	2
R1	13
R2	30
TG	185
Number of samples	2048
Sampling rate	0.4 ms
Bandwidth	2.5 kHz

Table 7.1: Fixed parameters for single-voxel acquisitions of metabolite spectra during QA.

where g is the apodization constant selected by the user in Hz and Δt is the sampling time interval.

The QA spectra have been submitted to a Gaussian apodization function with $g = 1$ Hz. No higher values for g have been selected to prevent peaks from overlapping because of the consequent linewidth broadening. The effects of the apodization in the frequency domain can be viewed in Figure 7.2 and consist in a substantial reduction of noise in the baseline.

Afterwards, the spectra have been submitted to quantification by the AMARES algorithm. Peak picking is a critical prior step because it provides the starting values for AMARES. It is essential to select peaks in a greater quantity than what is of interest in order to prevent AMARES from reaching wrong conclusions for the optimization during the consecutive iterations in the processing.

The outcomes presented by AMARES consist in the computed quantities together with their standard deviations and the graphical screen view of the estimated components, the ones found in the spectrum and the residue

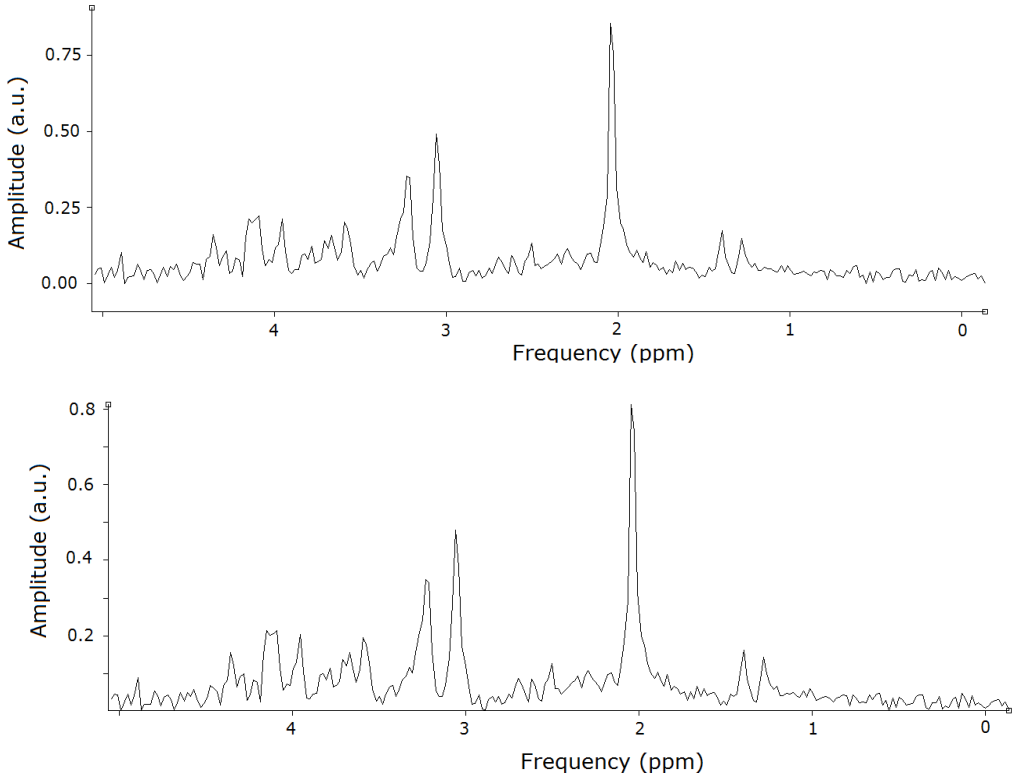

Figure 7.2: jMRUI screen views of a metabolite spectrum acquired by PRESS before (top) and after the Gaussian apodization (bottom).

obtained by the removal of the identified signals from the original spectrum. The screen views for peak peaking selections in the spectrum and the quantification graphical results are reported in Figure 7.3.

The key for the interpretation of the reported label numbers of the selected peaks is reported in Table 7.2. The peaks of interest for quantification purposes are the ones labelled with the numbers 3, 4, 5 and 6. More peaks have been selected in order to provide additional prior knowledge to AMARES and reach a more accurate solution. Furthermore, this particular selection leads to a flat residual spectrum characterized by an approximately flat noise baseline in the metabolite spectral region, which can be viewed at the top of Figure 7.3. This suggests that AMARES has led to successful results in the disentanglement of the peaks from the noise content in the

spectrum.

no.	Metabolite	Centre frequency (ppm)
1	Lac	1.26
2	Lac	1.38
3	NAA	2.01
4	Cr	3.03
5	Cho	3.19
6	mI	3.52
7	mI	3.61
8	Cr	3.93

Table 7.2: Key for the label numbers associated to the metabolite peaks in Figure 7.3.

7.2.3 Results of the quantification of metabolite peaks

Results of the quantification of peak amplitudes by AMARES have been compared to the values provided by the workstation software for NAA, Cr, Cho and mI during QA. As it has been explained in Chapter 2, these metabolites may have multiple resonances in the spectrum. However, the quantification has been conducted only over the main peaks located at the frequencies listed in Table 7.3 [69], coherently with the modus operandi of the workstation software.

Actually, mI should be identified by a doublet of doublets at 3.52 ppm. However, these peaks are unresolvable at 1.5 T and a single peak appears in the spectrum. Among other minor resonances originated by the metabolites listed in Table 7.3 the most important comes from the $-^2CH_2$ group of Cr at 3.91 ppm, whose peak is not included in the quantification because of its closeness to the residal water located on the left of 4 ppm threshold.

Further resonances present in the spectrum arise from Lac and Glu, the

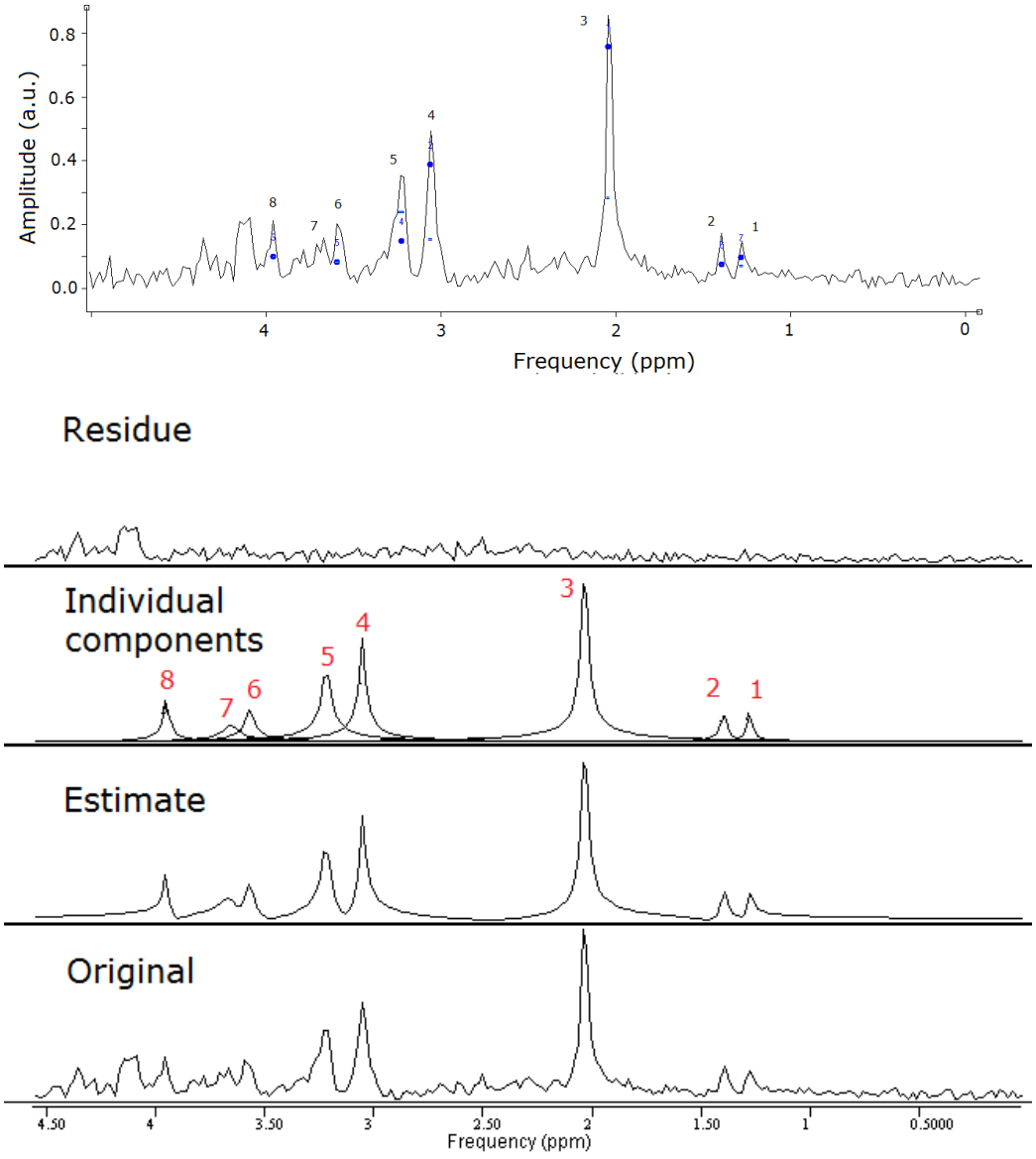

Figure 7.3: jMRUI screen views of the peaks picked on a QA spectrum (top) and the graphical results by AMARES (bottom).

Metabolite	Chemical group	Centre frequency (ppm)
NAA	$-^2CH_3$	2.01
Cr	$-CH_3$	3.03
Cho	$-(CH_3)_3$	3.19
mI	$-^1CH$	3.52

Table 7.3: Centre frequencies for the peaks of interest for AMARES quantification in QA spectra.

latter of which displays several minor peaks overlapping the mI peak (between the Cho and the $-^2CH_2$ group of Cr peaks) and the tail of the NAA peak between 2 ppm and 3 ppm. However, in vivo disturbances coming from macromolecules and lipids are absent in the phantom spectra.

The quantification results by AMARES for the amplitude of NAA, Cr, Cho and mI for QA spectra using STEAM and PRESS sequences are reported in Table 7.4. The quantifications for water have been computed by HLSVD over the apodized non-water-suppressed spectra. Also the mean values for amplitude from the three trials are reported.

The errors for metabolites correspond to the standard deviations computed by AMARES, whereas the errors for water correspond to the square root of the standard deviations estimated by HLSVD because its calculations are noniterative and account for greater uncertainty regarding the parameters, as it has been mentioned in Chapter 5.

Considering the results listed in Table 7.4, it is evident that amplitude values obtained by STEAM are approximately half the ones given by PRESS. These values are coherent with the fact that STEAM excites only half of the equilibrium magnetization because of the formation of the stimulated echo. This results in a reduction of the signal by a factor of 2, as it has been discussed in Chapter 1.

Considering the values for amplitudes listed in Table 7.4, the relative ratio of metabolite and water amplitudes over Cr have been computed. These

STEAM amplitudes ($\times 10^{-4}$ a.u.)				
	no. 1	**no. 2**	**no. 3**	**Mean**
NAA	7.4 ± 0.1	7.4 ± 0.1	7.1 ± 0.1	7.3 ± 0.2
Cr	4.8 ± 0.1	6.3 ± 0.2	4.4 ± 0.1	5.1 ± 0.2
Cho	4.7 ± 0.2	5.3 ± 0.2	4.1 ± 0.2	4.7 ± 0.3
mI	2.3 ± 0.2	2.1 ± 0.1	2.0 ± 0.2	2.1 ± 0.3
H_2O	1,790 ± 10	1,790 ± 10	1,790 ± 10	1,790 ± 20
PRESS amplitudes ($\times 10^{-4}$ a.u.)				
	no. 1	**no. 2**	**no. 3**	**Mean**
NAA	16.5 ± 0.1	16.3 ± 0.1	17.0 ± 0.1	16.6 ± 0.2
Cr	10.9 ± 0.1	11.1 ± 0.1	11.2 ± 0.1	11.1 ± 0.2
Cho	9.4 ± 0.2	9.3 ± 0.2	9.8 ± 0.2	9.5 ± 0.3
mI	5.2 ± 0.1	4.5 ± 0.1	4.8 ± 0.2	4.8 ± 0.3
H_2O	900 ± 10	900 ± 10	900 ± 10	900 ± 20

Table 7.4: AMARES an HLSVD amplitude calculations and mean values for metabolites and water in the QA spectra.

calculations are an useful means to compare the results provided by jMRUI time-domain fitting algorithms with peak integration performed by the GE workstation software in the frequency domain. These values are listed in Table 4.7.

The ratios computed by the two software are reported together in Table 7.5 for a comprehensive overview. The ratios for water over Cr are multiplied by a factor of 2 to consider that water spectra have been acquired with a half number of averages.

The results listed in Table 7.5 for ratios computed by the two softwares are in agreement with each other within experimental uncertainties. The errors for the workstation ratios are computed from the standard deviation from the three trials since the software does not calculate them.

Considering the errors for STEAM and PRESS ratios computed by jM-

	Ratios over Cr in STEAM		**Ratios over Cr in PRESS**	
	GE workstation	**jMRUI**	**GE workstation**	**jMRUI**
NAA	1.54 ± 0.09	1.42 ± 0.08	1.48 ± 0.04	1.50 ± 0.04
Cr	1.00 ± 0.04	1.00 ± 0.07	1.00 ± 0.02	1.00 ± 0.03
Cho	0.89 ± 0.08	0.91 ± 0.07	0.81 ± 0.04	0.86 ± 0.03
mI	0.46 ± 0.04	0.41 ± 0.06	0.48 ± 0.02	0.44 ± 0.03
H_2O	3600 ± 200	3500 ± 200	3200 ± 200	3240 ± 80

Table 7.5: Comparison of the results for ratios over Cr for metabolites and water computed by GE workstation software and jMRUI.

RUI, it is worth noticing that in general the accuracy in the uncertainty determination by the algorithms is more refined for PRESS. This is due to the fact that peaks are more easily discernible from the noise by the algorithms thanks to the higher SNR than STEAM.

With regards to this matter of fact, the Cr SNR has been evaluated as the ratio of the Cr amplitude over the noise computed by AMARES. The values are reported in Table 7.6.

	STEAM	**PRESS**
Noise	2.63 $\times 10^{-5}$ a.u.	2.56 $\times 10^{-5}$ a.u.
Cr SNR	19.5	43.1

Table 7.6: Noise and Cr SNR over the STEAM and PRESS QA spectra using the results of AMARES.

Considering the results reported in Table 4.8 with the values listed in Table 7.6, it is deducible that they are of the same order of magnitude, thus indicating a general reasonable agreement. However, it should be mentioned that noise is computed from an area in the spectrum lacking metabolites by the GE workstation software (frequency-domain approach), whereas noise is computed over the last 204 points of the FID, corresponding to 10 % of the

sampled signal, by jMRUI (time-domain approach).

Chapter 8

Characterization of the in-house phantom

8.1 Spectral analyses

8.1.1 Identification of the phantom content by MRS

The in-house phantom provided by the "Interconfronto di spettroscopia in RM" group consists in an aqueous solution in a spherical phantom. Its content has to be accurately determined by performing dedicated MRS acquisitions. Each group from the Medical Physics units from the hospitals participating in the project is given a different phantom containing metabolites with nonspecified concentrations.

The purpose of the investigations is to build a database of metabolites to provide a common ground for comparison of results between the groups and build a robust protocol effective for in vivo examinations. It will be possible to retrieve information regarding the accuracy of metabolite detection from the data collected at each hospital unit by comparing results obtained with different clinical scanners at different static fields.

The phantom data will provide a basis for the reliability of MRS in the diagnostic routine. Indeed, often phantoms are used as concentration refer-

ence for accurate quantification of in vivo spectra. By calibrating the patient protocols on phantoms, it is possible to detect and possibly correct for systematic errors or artifacts which might make the examination inaccurate.

8.1.2 Quantification of the solvent

Water is the compound used as concentration reference for the absolute quantification of metabolites because of its natural abundance in the human brain. Therefore, non-water-suppressed spectra have been acquired as the first step for quantification.

The major issue for the detection of the water signal is caused by its long relaxation times. If the TR of a spectroscopic sequence is shorter than four to five time the T_1 of water, the perturbed magnetization will not be able to recover before the following excitation pulse is applied, thus leading to a reduction of the longitudial component, a phenomenon which is commonly referred to as partial saturation.

To assess the amplitude of the water peak for absolute quantification, a set of spectra acquired at different TEs have been acquired using PRESS as spectroscopic sequence. The result is the relaxation curve for water, which has been estimated for the GE phantom as well. The TR has been kept fixed for all the acquisition to 15000 ms to ensure that the longitudinal magnetization has completely recovered to equilibrium. The complete list of the fixed parameters is reported in Table 8.1.

Water and metabolite spectra have been acquired using a $20\times20\times20$ mm^3 VOI located at the centre of the phantom since the absolute concentration is directly proportional to the dimensions of the localized volume, coherently with the analyses discussed in Chapter 6. The centre does correspond to the isocentre of the magnet because of the spout of the magnet, as it is depicted in Figure 8.1.

Afterwards, ten water peaks have been acquired at varying TEs in order to build up the T_2 relaxation curve. The spectral quantification has been performed by HLSVD after the apodization of the FID with a 2 Hz Gaussian

Parameter	
TR	15000 ms
Number of averages	4
Phase cycling	2
R1	13
R2	30
TG	162
Number of samples	2048
Sampling rate	0.4 ms
Bandwidth	2.5 kHz

Table 8.1: Fixed parameters for single-voxel acquisitions of the water peaks of the in-house phantom.

weighting function. Actually, apodization would not be necessary for the accurate quantification of the water peak, while it will be for more refined calculations of the metabolite peaks. This preprocessing step is performed on the water signal for coherence with the other acquisitions. The HLSVD computed values for water amplitudes at varying TEs are reported in Table 8.2.

The results listed in Table 8.2 for amplitudes have been plotted in Figure 8.2.

The equation for the fitting line has been obtained by the method of the weighted least squares for exponential trends (TE in ms).

$$A(\mathrm{TE}) = (0.65e^{-0.00081\cdot \mathrm{TE}})\ \text{a.u.} \tag{8.1}$$

with

$$R = -\ 0.999 \tag{8.2}$$

$$A(0) = (0.65 \pm 0.02)\ \text{a.u.} \tag{8.3}$$

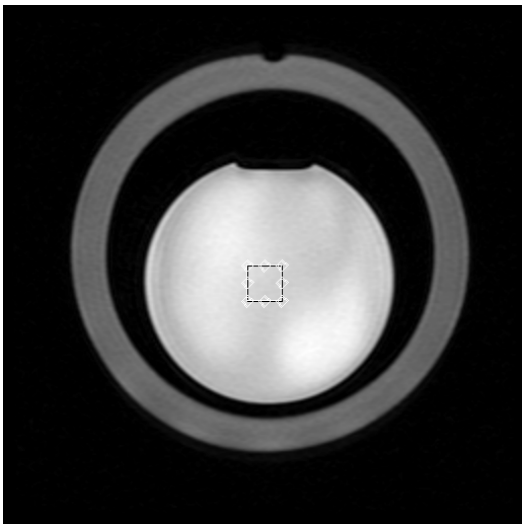

Figure 8.1: VOI positioning in the axial image of the in-house phantom.

TE (ms)	**Amplitude ($\times 10^{-1}$ a.u.)**
30	6.4 ± 0.1
50	6.3 ± 0.1
70	6.2 ± 0.1
100	6.0 ± 0.1
200	5.5 ± 0.1
300	5.1 ± 0.1
400	4.7 ± 0.1
600	4.1 ± 0.1
800	3.4 ± 0.1
1000	2.9 ± 0.1

Table 8.2: HLSVD results for water peak amplitudes at varying TEs.

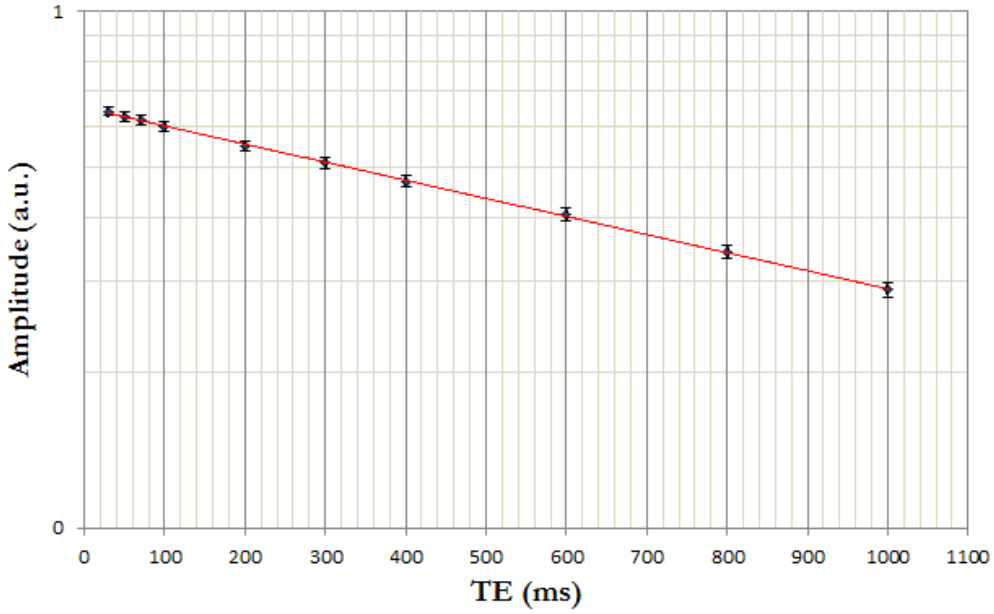

Figure 8.2: Water peak amplitude in function of TE values.

which is the fitted amplitude of the water peak at null TE. The value for T_2 is directly calculated from the fitted parameter:

$$T_2 = (1240 \pm 60) \text{ ms} \tag{8.4}$$

This accurate value for T_2 is very close to the relaxation times displayed by water in unconfined conditions at room-temperatures. This estimate suggests that the phantom is devoid of paramagnetic agents or it contains them in negligible concentrations.

A qualitative estimate supporting this assumption is given by the comparison of the spin-echo scout image of in-house phantom image reported in Figure 8.1 with images of the GE test phantom in Figure 4.1, both acquired with the same sequence parameters. There is an evident difference in the grey level intensities, suggesting that the signal, which is mainly due to water, has decayed faster in the images of the GE test phantom.

Furthermore, it is important to mention that this result for water T_2 is not

biased by partial recovery of the longitudinal magnetization thanks to the imposition of TR = 15000 ms, which is five times greater than T_1 = 3000ms, which is approximately the longitudinal relaxation time constant for water in bulk conditions.

8.1.3 Quantification of the solutes

Water-suppressed spectra have been acquired in order to assess the metabolite content of the phantom. The PRESS sequences have been performed with the fixed parameters listed in Table 8.3 while varying TE values from 35 ms to 288 ms for each acquisition.

Parameter	
TR	4000 ms
Number of averages	32
Phase cycling	8
R1	13
R2	30
TG	162
Number of samples	2048
Sampling rate	0.4 ms
Bandwidth	2.5 kHz

Table 8.3: Fixed parameters for single-voxel acquisitions of the metabolite peaks of the in-house phantom.

As it can be viewes in Table 8.3, TR has been shortened to 4000 ms in relation to the values used for the water peak. This is because metabolite relaxation times are shorter than water, which is suppressed by the CHESS pulses. The ratio of the number of averages N_{avg} over the phase cycling NEX gives the number of effective acquired frames N_f. The only constraint is that N_{avg} be a multiple of NEX.

$$N_f = \frac{N_{avg}}{NEX} = 4 \tag{8.5}$$

Comparing this result with the values listed in Table 8.1 for the water peak, giving a N_f equal to 2, the value for metabolites is set to 4 to obtain a better SNR. The high value for NEX is needed to remove spurious FIDs and echoes present in the spectroscopic sequence which may degrade the quality of the sampled FID. This outcome is achieved by maximizing the FID of interest by the sum and subtraction of the signals for phase cycling. A lower value for NEX is sufficient for water thanks to its high SNR value.

PRESS with water suppression has been performed at TEs equal to 35 ms, 70 ms, 100 ms, 144 ms and 288 ms. The screen views of the spectra on the GE workstation and on jMRUI are displayed in Figure 8.3. The raw spectra have been submitted to preprocessing jMRUI operations such as residual water removal in the 1 ppm frequency region centred at 4.85 ppm and apodization.

From the observation of Figure 8.3, it is deducible that the contained metabolites are Creatine, whose peaks at 3.03 ppm and at 3.93 are distinguishable, and Lactate, whose doublet is centred at 1.31 ppm. Residual water peaks are recognizable in the spectral region below 4.00 ppm on the jMRUI screen view.

Quantification of the metabolite peak amplitude has been obtained by performing AMARES over the spectra after Gaussian apodization with apodization constant equal to 2 Hz. The broadening of the peak linewidth because of apodization is not a disadvantage because of the gain in SNR and the absence of several peaks commonly present in ^{1}H MRS.

The AMARES results for peak amplitude calculations are reported in Table 8.4. Data for the $-CH_2$ peak of Cr have not been taken into account because of its closeness to the residual water (the results given by AMARES are unrealistic).

Comparing the results reported in Table 8.4 for Cr and Lac, it is evident that greater uncertainties regarding Lac are estimated by AMARES because

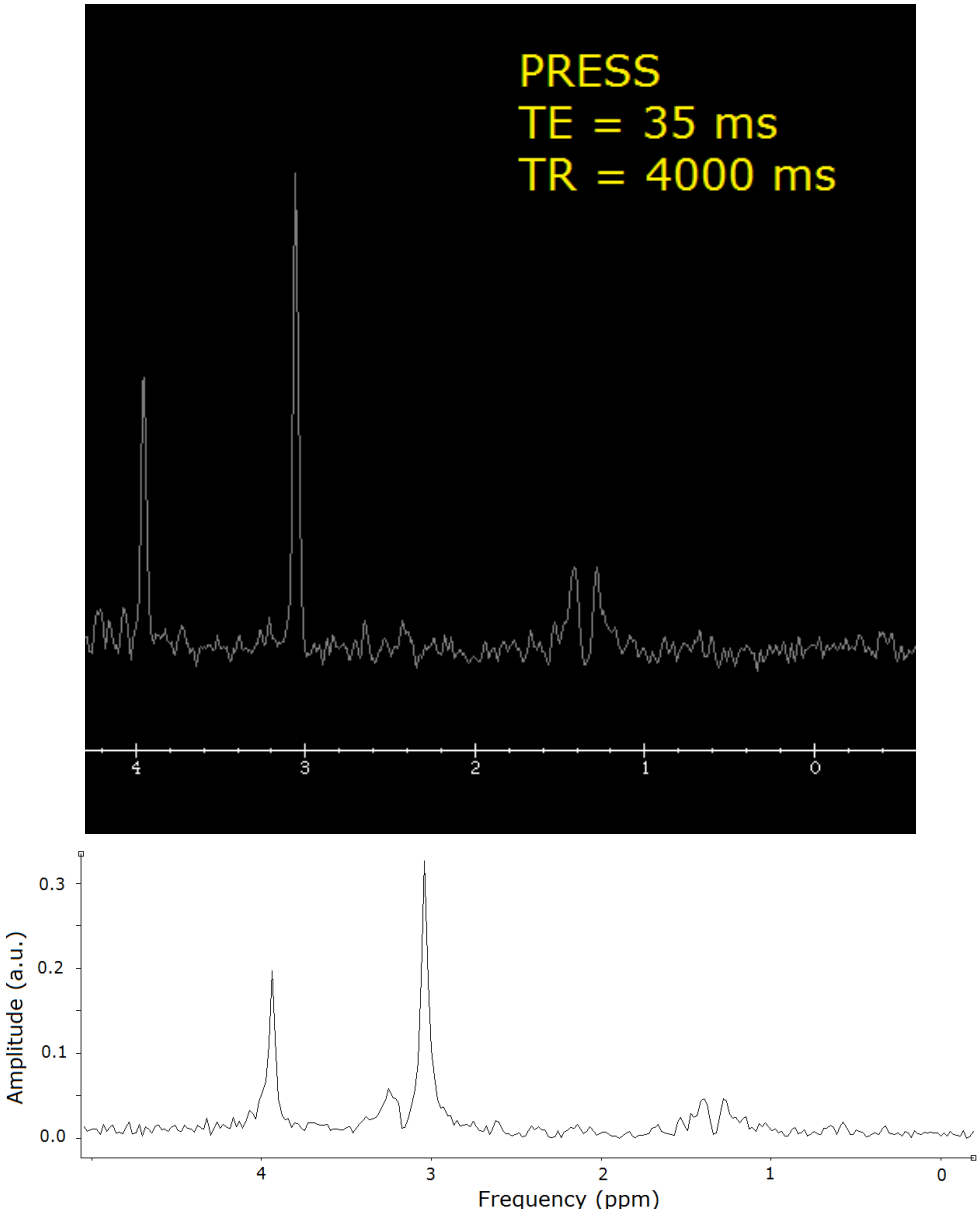

Figure 8.3: GE workstation (top) and jMRUI screen views (bottom) of the metabolite spectrum acquired at TE = 35 ms.

	$-CH_3$ **peak of Creatine**	**Lactate doublet**
TE (ms)	**Amplitude** ($\times 10^{-5}$ **a.u.**)	**Amplitude** ($\times 10^{-5}$ **a.u.**)
35	62.5 ± 0.3	38.0 ± 0.7
70	55.4 ± 0.4	21.7 ± 0.6
100	49.2 ± 0.3	18 ± 1
144	47.8 ± 0.4	12.9 ± 0.6
288	39.9 ± 0.4	6 ± 1

Table 8.4: AMARES results for peak amplitudes for Cr and Lac at varying TEs.

of its lower SNR, especially at greater TE values when the signal is lower. The AMARES results for Cr amplitude are graphed in Figure 8.4.

The exponential fitting is expressed by the following equation (TE in ms):

$$A(\mathrm{TE}) = (6.1 \times \ 10^{-4} e^{-0.00158 \cdot \mathrm{TE}}) \text{ a.u.} \tag{8.6}$$

with

$$R = -\ 0.961 \tag{8.7}$$

The intercept $A(0)$ corresponds to the Cr amplitude at null TE.

$$A(0) = (6.1 \pm 0.1) \times \ 10^{-4} \text{ a.u.} \tag{8.8}$$

The interpolated value for T_2 for Creatine is the following:

$$T_2 = (630 \pm 40) \text{ ms} \tag{8.9}$$

The computed value is considerably different from the one found in literature for in vivo MRS, as listed in Table 4.6, suggesting again the absence of paramagnetic agents in the phantom. The value is close to the weighted average of the values found for Creatine and Phosphocreatine (PCr) in bulk conditions [70], reported in Table 8.5.

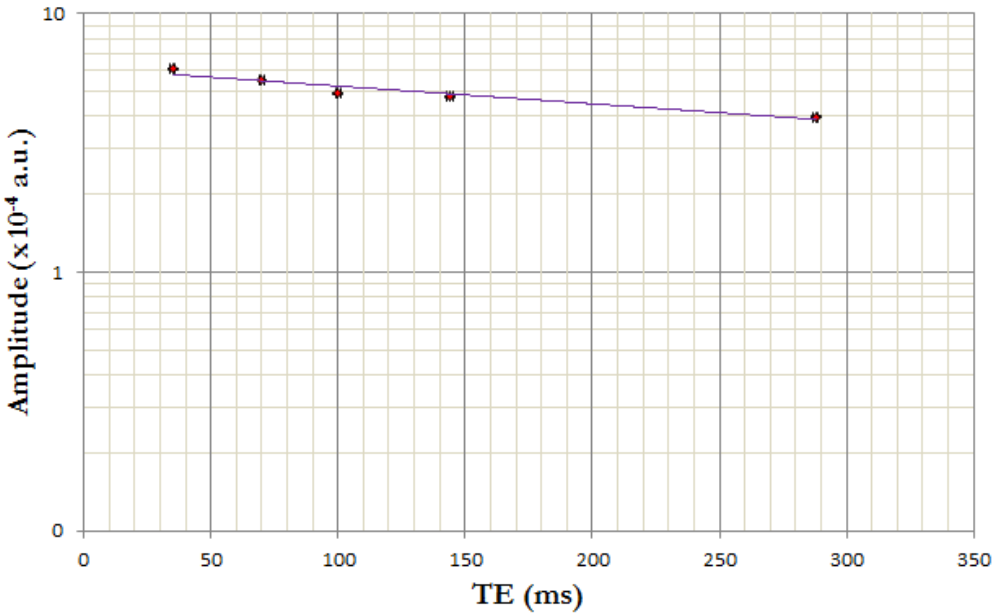

Figure 8.4: Creatine peak amplitude in function of TE values.

	T_2 (ms)
Cr	909
PCr	555

Table 8.5: Relaxation times constants for Cr and PCr in bulk conditions [70].

These two metabolites contribute to the formation of the same peak at 3.03 ppm at 1.5 T and at 3 T. They can be separated only at higher fields, which are not used in clinical practice. Typically, Cr is present in greater concentrations than PCr in the human brain when metabolism is significantly accelerated. Their relative ratio is variable, however, it a good approximation that PCr contributes for the 55% to the Creatine peak.

It is often neglected the fact that these two molecules lead to a **biexponential relaxation component** in the signal. Therefore, the value for T_2 reported in Equation 8.9 is an effective value given by both contributions. Considering the T_2 values listed in Table 8.5 and the approximate percentages

of these two compounds, it is possible to estimate the theoretical effective value for the comprehensive peak:

$$T_{2eff} = (\frac{0.45}{T_{2Cr}} + \frac{0.55}{T_{2PCr}})^{-1} \simeq 670 \text{ ms} \tag{8.10}$$

The computed value for T_{2eff} is compatible with the fitted value for T_2 for Creatine within experimental errors. This estimate suggests the fact that both solutes are present in the phantom.

The exponential fitting for the amplitude values of the Lac doublet is depicted in Figure 8.5.

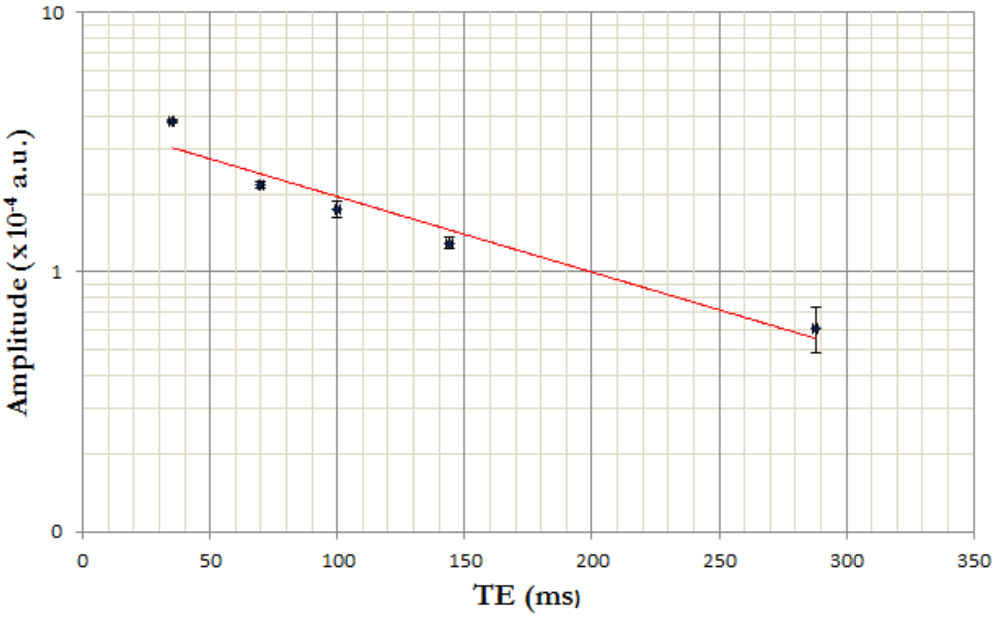

Figure 8.5: Lactate doublet amplitude in function of TE values.

The fitted equation is the following (TE in ms):

$$A(\text{TE}) = (3.9 \times \ 10^{-4} e^{-0.00694 \cdot \text{TE}}) \text{ a.u.} \tag{8.11}$$

with

$$R = -\ 0.947 \tag{8.12}$$

The interpolated amplitude at null TE for Lac is:

$$A(0) = (3.9 \pm 0.3) \times \ 10^{-4} \text{ a.u.} \tag{8.13}$$

The reciprocal of the fitted factor in the exponential for Lac is the following:

$$\frac{1}{\mathrm{R}_2} = (144 \pm 9) \text{ ms} \tag{8.14}$$

The interpolated $\frac{1}{R_2}$ does not correspond neither to the in vivo T_2, i.e. 240 ms, nor to the bulk value for Lac, i.e. 1030 ms [71]. Apparently, this value corresponds to the inversion time $\mathrm{TE}_{\mathrm{inv}}$, at which the Lac doublet is out of phase because of its coupling constant J, equal to 7 Hz, as it has been discussed in Chapter 2. The signal is out of phase at

$$\mathrm{TE}_{\mathrm{inv}} = \frac{1}{J} = 144 \text{ ms} \tag{8.15}$$

when the doublet is inverted, while it returns in-phase at

$$\mathrm{TE}_{\mathrm{in-phase}} = \frac{2}{J} = \ 288\text{ms} \tag{8.16}$$

giving rise to a positive doublet.

The observed phenomenon is the **signal cancellation due to anomalous J modulation**, which causes the Lac phase to be strongly dependent on the echo time [39]. Therefore, the Lac signal decay is modulated by its J coupling constant. This modulation occurs regardless of the static magnetic field strength and causes the signal to decay. This effect seem to be considerably dominating over the transverse relaxation time, which is not deducible from the relaxation curve. Lac is rephased at 288 ms, but the signal has decayed so fast that the doublet is identified by AMARES in competition with the noise baseline (the Lac signal has almost completely decayed).

8.2 Internal concentration reference method

8.2.1 Water content estimation

The **internal concentration reference method** is based on the comparison of the resonance amplitudes below the peaks with that of a relatively stable endogenous reference compound in the brain. NAA, Cr and water have been proposed as reference. Anyway, it should be mentioned that their concentration might considerably fluctuate depending on the pathologies.

Water is a basis for ^{1}H MRS studies, however, it is important to remind that its concentration is not the same in different compartments of the brain, as it is described in Table 2.1. In principle, the water molar concentration of water should be known in advance to adequately quantify metabolite concentration. The values found in literature are used for this purpose for in vivo analyses.

Phantoms are used for the phantom replacement external concentration reference method. Basically, it consists in the use of the phantom as a basis for the simulation of the human brain. Systematic errors affect the tissues and the phantom approximately in the same proportion. The only complication is the different coil loading between the tissue and the phantom because of different electrical conductivities.

An approach similar to the internal concentration reference method will be applied in order to achieve the phantom characterization. However, since the water content of the phantom is unknown, it has to be experimentally determined.

The basic experimental assumption is that metabolite concentrations are negligible compared with water. The first step is to measure the volume of the spherical phantom whose radius has been measured as:

$$r = 0.75 \pm 0.01 \text{ dm} \tag{8.17}$$

Therefore, the volume of the phantom becomes:

$$V = 1.770 \pm 0.07 \text{ dm}^3 \tag{8.18}$$

The number of moles for water is determined by taking into account literature values for the density ρ of water at 22°C [72] to determine the mass m(g) and its molar mass m_{molar} [73], reported in Table 8.6. The mass

Quantity	**value**
ρ(22°C)	0.9977735 g/cm^3
m_{molar}	18.01528 g/mol

Table 8.6: Density at 22°C and molar mass values of water.

is estimated as:

$$m(\text{g}) = \rho V = (1760 \pm 70) \text{ g} \tag{8.19}$$

Consequently, the number of moles n_{moles} is calculated as:

$$n_{moles} = \frac{m(\text{g})}{m_{molar}} = (97.9 \pm 0.2) \text{ mol} \tag{8.20}$$

In conclusion, it is possible to estimate the molar concentration of water as the ratio of the number of moles over the volume expressed in dm^3.

$$C_{H_2O} = \frac{n_{moles}}{V(\text{dm}^3)} = (55 \pm 2) \text{ M} \tag{8.21}$$

Considering the concentration values for water in different human brain compartments listed in Table 2.1, the water concentration of the in-house phantom is coherent with the value reported for the Cerebrospinal Fluid. The experimental value will be the reference for the assessment of the metabolite concentrations of the phantom.

8.2.2 Determination of metabolite concentrations

The metabolite concentrations are estimated using the internal concentration reference method which consist in the intepolation of the metabolite

and water amplitude at TE = 0 [2]. These values have been fitted by the T_2 relaxation curves for the in-house phantom, build up in the previous section from PRESS spectra with and without suppression of the water signal [74].

It is important to stress that this particular method is based upon the nontrivial assumption that quantifications are coherent with pathological conditions in which the water concentration in the brain compartment under investigation is not influenced by the disease progression. Other factors which are assumed to be relatively constant include the TE of water and the percentage of free water, i.e. the portion of the water contained in body tissues which is not bound by macromolecules or organelles.

According to the internal concentration reference method, the absolute concentrations of metabolites can be computed referring to the following expression:

$$C_{metabolite} = \frac{A(0)_{metabolite}}{A(0)_{H_2O}} \frac{N_{H_2O}}{N_{metabolite}} C_{H_2O} R_{avg} \tag{8.22}$$

where $C_{metabolite}$ is expressed as a function of the ratio of the interpolated metabolite peak amplitude at TE = 0 over the water amplitude, the number of protons of the water molecule N_{H_2O} over the number of protons in the chemical group giving rise to the peak in the spectrum $N_{metabolite}$, the water molar concentration C_{H_2O} and a corrective factor R_{avg}, i.e. the squared ratio of number of frames used to acquire the water peaks over the number used for the metabolite spectra to take into account the application of a twofold RF power, proportional to B_1^2, contributing to the overall signal formation.

The errors for the absolute concentrations has been calculated considering the square root of the sum of the relative errors for amplitudes and water absolute concentration, as the following expression indicates:

$$\Delta C_{metabolite} = \sqrt{(\frac{\Delta A(0)_{metabolite}}{A(0)_{metabolite}})^2 + (\frac{\Delta A(0)_{H_2O}}{A(0)_{H_2O}})^2 + (\frac{\Delta C_{H_2O}}{C_{H_2O}})^2} \cdot C_{metabolite} \tag{8.23}$$

Since both the Cr peak at 3.03 ppm and the Lac doublet at 1.31 ppm are

generated by the $-CH_3$ group, $N_{metabolite} = 3$ for both solutes. Considering the amplitude values at TE = 0 for water, Cr and Lac in Equations 8.3, 8.8 and 8.13, the absolute concentration of Cr and Lac have been estimated to be:

$$C_{Cr} = (8.6 \pm 0.5) \text{ mM} \tag{8.24}$$

$$C_{Lac} = (5.5 \pm 0.4) \text{ mM} \tag{8.25}$$

The absolute concentration values for Cr and Lac are characterized by relative uncertainties of 5.8% and 7.2% respectively, which guarantee a satisfactory accuracy in the characterization of the phantom content.

Conclusions

The results of the quantification in the time domain of single-voxel spectroscopic acquisitions performed on the GE Signa HDxt 1.5 T clinical scanner at the Pavillion no.11 of the S.Orsola-Malpighi hospital in Bologna have been presented. Fitting algorithms provided by jMRUI have proved their feasibility and accuracy in the determination of parameters of interest in the spectra. This is of utmost importance for the contribution to a common database for the "Interconfronto di spettroscopia in RM" working group of Associazione Italiana di Fisica Medica (AIFM) to compile a robust and unbiased protocol for clinical examinations by MRS.

After the quality assurance on the GE Signa HDxt 1.5 T with standard and innovative methods, both spectra with and without suppression of the water peak have been acquired on the dedicated GE spectroscopic test phantom. These acquisitions have enabled an accurate quality assurance with innovative methods. For instance, the outcomes of the analyses of non-water-suppressed spectra are coherent with the NMR principle of the statistical increase of the signal when exciting greater VOIs. From the fitting of the relaxation curve of the water peak at varying TEs a reliable T_2 has been deduced.

Spectra of the metabolite content of the GE test phantom have been acquired by the application of short TE STEAM and PRESS sequences during quality assurance. The comparison of the ratios of the metabolite amplitudes over Creatine computed by the workstation software, which works on the frequencies, and jMRUI, which works in the time domain, shows good

agreement within experimental errors. This correspondence suggests that quantifications in the time and in the frequency domain may lead to consistent results.

The characterization of the in-house phantom provided by the working group has achieved its goal of assessing the solution content and the metabolite concentrations with good accuracy. The molar concentrations of water, Creatine and Lactate have been determined with experimental accuracies of 3.6%, 5.8% and 7.2% respectively. Higher accuracy could have been obtained if there had not been the constraint to work in conditions as close as possible to the clinical routine, the most important being the reduction in the exam duration. Notwithstanding these constraints, the goodness of the experimental procedure and data analysis has been demonstrated by the correct estimation of the T_2 of water, the observed biexponential relaxation curve of Creatine and the correct TE value at which the modulation by J coupling causes the Lactate doublet to be inverted in the spectrum.

For diagnostic uses in specific pathologies more accurate MRS clinical protocols are needed. This work has been developed in this context. It is expectable that progress in MRS will provide promising results for biochemical and metabolic studies of a wide range of pathologies, making this technique more frequently employed in the clinical practice.

The work of this thesis has demonstrated that it is possible to perform measurements and establish protocols for data analysis, based on the physical principles of NMR, which are able to provide robust values for the spectral parameters of clinical use.

Bibliography

[1] Fayed N., Olmos S., Morales H. and Modrego P.J., *Physical basis of magnetic resonance spectroscopy and its application to central nervous system diseases*, American Journal of Applied sciences 3(5):1836-1845, 2006

[2] De Graaf R.A., *In vivo NMR spectroscopy- 2nd edition: principles and techniques*, John Wiley & sons, 2007

[3] Boesch C., *Molecular aspects of magnetic resonance imaging and spectroscopy*, Molecular aspects of medicine 20:185-318, 1999

[4] http://nmrcentral.com/2011/08/chemical-shift/

[5] Drost D.J., Riddle W.R. and Clarke G.D., *Proton magnetic resonance spectroscopy in the brain: report of AAPM MR task group no.9*, Medical physics 29(9):2177-2197, 2002

[6] Callaghan P.T., *Principles of nuclear magnetic resonance microscopy*, Oxford University press, 1991

[7] Keeler J., *Understanding NMR spectroscopy- 2nd edition*, John Wiley & sons, 2010

[8] Brown T.R., Stoyanova R., Greenbeg T., Srinivasan R. and Murphy-Boesch J., *NOE enhancements and T_1 relaxation times of phosphorylated metabolites in human calf muscle at 1.5 Tesla*, Magnetic resonance in medicine 33:417-421, 1995

[9] http://www.cis.rit.edu/htbooks/mri/inside.htm

[10] http://www.scs.illinois.edu/nmr/handouts/general_pdf/ugi034.pdf

[11] Oppenheim A.V. and Schafer R.V., *Discrete-time signal processing- 3rd edition*, Pearson Education, 2009

[12] McRobbie D.W., Moore E.A., Graves M.J. and Prince M.R., *MRI: from picture to proton- 2nd edition*, Cambridge University press, 2006

[13] Bushberg J.T., Seibert J.A., Leidholdt E.M. and Boone J.M., *The essential physics of medical imaging- 3rd edition*, Lippincott William & Wilkins, 2011

[14] Mansfield P., *Imaging by nuclear magnetic resonance*, Journal of Physics E: scientific instruments 21:18-30, 1988

[15] Barker P.B., Hearshen D.O. and Boska M.D., *Single-voxel proton MRS of the human brain at 1.5 T and 3.0 T*, Magnetic resonance in medicine 45:765-769, 2001

[16] Di Costanzo A., Trojsi F., Tosetti M., Giannatempo B.M., Nemore F., Piccirillo M., Bonavita S., Tedeschi G. and Scarabino T., *High-field proton MRS of human brain*, European journal of radiology 48:146-153, 2003

[17] Tkac I., Andersen P., Adriany G., Merkle H., Ugurbil K. and Gruetter R., *In vivo* ^1H *NMR spectroscopy of human brain at 7 T*, Magnetic resonance in medicine 46:451-456, 2001

[18] Atkinson I.C., Lu A. and Thulborn K.R., *Characterization and correction of system delays and eddy currents for MR imaging with ultrashort echo-time and time-varying gradients*, Magnetic resonance in medicine 62:532-537, 2009

[19] Terpstra I., Andersen P. and Gruetter R., *Localized eddy current compensation using quantitative field mapping*, Journal of magnetic resonance 131:139-143, 1998

[20] Bernstein M.A., King K.F. and Zhou X.J., *Handbook of MRI pulse sequences*, Elsevier, 2004

[21] Barker P.B., Bizzi A., De Stefano N., Gullapalli R. and Lin D.D.M., *Clinical MR spectroscopy: techniques and applications*, Cambridge University Press, 2010

[22] Ordidge R.J., Connelly A. and Lohman J.A., *Image-selected in vivo spectroscopy (ISIS). A new technique for spatially selective NMR spectroscopy*, Journal of magnetic resonance 66:283-294, 1986

[23] Burger C., Buchli R., McKinnon G., Meier D. and Boesiger P., *The impact of the ISIS experiment order on spatial contamination*, Magnetic resonance in medicine 26:218-230, 1992

[24] Tkac I., Starcuk Z., Choi I.Y. and Gruetter R., *In vivo* ^1H *NMR spectroscopy of rat brain at 1 ms echo time*, Magnetic resonance in medicine 41:649-656, 1999

[25] Hamilton G., Middleton M.S., Bydder M., Yokoo T., Schwimmer J.B., Kono Y., Patton H.M., Lavine J.E. and Sirlin C.B., *The effect of PRESS and STEAM sequences on magnetic resonance spectroscopic liver fat quantification*, Journal of magnetic resonance imaging 30(1):145-152, 2009

[26] Thompson R.B. and Allen P.S., *Response of metabolites with coupled spins to the STEAM sequence*, Magnetic resonance in medicine 41:649-656, 1999

[27] https://irc.cchmc.org/research/spect.php

[28] Van der Veen J.W., Weinberg D.R., Tedeschi G., Frank J.A. and Duyn J.H., *Proton MR spectroscopic imaging without water suppression*, Radiology 217:296-300, 2000

[29] Hurd R.E., Gurr D. and Sailasuta N., *Proton spectroscopy without water suppression: the oversampled J-resolved experiment*, Magnetic resonance in medicine 40:343-347, 1998

[30] Soher B.J., Young K., Govindaraju V. and Maudsley A.A., *Quantitative proton MR spectroscopy and spectroscopic imaging of the human brain*, Magnetic resonance in medicine 35:356-363, 1996

[31] Koch K.M., Sacolick L.I., Nixon T.W., Rothman D.L. and De Graaf R.A., *Dynamically-shimmed multi-voxel* ^{1}H *magnetic resonance spectroscopy and multi-slice magnetic resonance spectroscopic imaging of the human brain*, Magnetic resonance in medicine 57:587-591, 2007

[32] Star-Lack J.M., Adalsteinsson E., Adam M.F., Terris D.J., Pinto H.A., Brown J.B. and Spielman D.M., *In vivo* ^{1}H *MR spectroscopy of human head and neck lymph node metastasis and comparison with oxygen tension measurements*, American journal of Neuroradiology 21:183-193, 2000

[33] Smith J.K., Kwock L. and Castillo M., *Effects of contrast material on single volume proton MR spectroscopy*, American journal of Neuroradiology 21:1084-1089, 2000

[34] http://en.wikipedia.org/wiki/N-Acetylaspartic_acid

[35] Hsu Y.Y., Du A.T., Schuff N. and Weiner M.W., *Magnetic resonance imaging and magnetic resonance spectroscopy in dementias*, Journal of Geriatric Psychiatry and Neurology 14:145-166, 2001

[36] http://it.wikipedia.org/wiki/Colina

[37] http://en.wikipedia.org/wiki/Creatine_kinase

[38] http://it.wikipedia.org/wiki/Acido_lattico

[39] Lange T., Dydak U., Roberts T.P.L., Rowley H.A., Bjeljac M. and Boesiger P., *Pitfalls in Lactate measurements at 3T*, American journal of Neuroradiology 27:895-901, 2006

[40] http://en.wikipedia.org/wiki/Inositol

[41] Kruse B., Hanefeld F., Christen H.J., Bruhn H., Michaelis T., Hanicke W. and Frahm J., *Alterations of brain metabolites in metachromatic leukodystrophy as detected by localized proton megnetic resonance spectroscopy in vivo*, Journal of Neurology 241:68-74, 1993

[42] http://en.wikipedia.org/wiki/Glutamic_acid

[43] http://en.wikipedia.org/wiki/Glutamine

[44] Lagemaat M.W., Maas M.C., Vos E.K., Bitz A.K., Orzada S., Weiland E., van Uden M.J., Kobus T., Heerschap A. and Scheenen T.W.J., ^{31}P *MR spectroscopic imaging of the human prostate at 7 T:* T_1 *relaxation times, nuclear Overhauser effect and spectral characterization*, Magnetic resonance in medicine 00:00-00, 2014

[45] Wolf C., Boesch S., Metzler B., Weirich-Schwaiger H., Trieb T. and Schocke M.F.H., *Phosphorous-31 two-dimensional Chemical Shift Imaging in the myocardium of patients with late onset of Freidreich ataxia*, Molecular imaging and biology 10:24-29, 2008

[46] http://en.wikipedia.org/wiki/Adenosine_triphosphate

[47] http://repository.unm.edu/bitstream/handle/1928/6886/Sanchez_Wenner%20Scholarly%20Paper.pdf?sequence=1

[48] Hartwig V., Giovannetti G., Vanello N., Lombardi M., Landini L. and Simi S., *Biological effects and safety in Magnetic Resonance Imaging: a review*, International Journal of Environmental Research and Public Health 6:1778-1798, 2009

[49] http://www.revisemri.com/questions/safety/fringe_field

[50] http://www3.gehealthcare.com/en/products/categories/magnetic_resonance_imaging/signa_hdxt_1-5t#tabs

[51] http://ric.uthscsa.edu/personalpages/lancaster/DI2_Projects_2006/RF_Coils.pdf

[52] https://www.aapm.org/pubs/reports/RPT_100.pdf

[53] Gudbjartsson H. and Patz S., *The Rician distribution of noisy MRI data*, Magnetic resonance in medicine 34:910-914, 1995

[54] https://www.aapm.org/pubs/reports/RPT_28.pdf

[55] Kreis R., *Issues of spectral quality in clinical* ^{1}H*-magnetic resonance spectroscopy and a gallery of artifacts*, NMR in biomedicine 17:361-381, 2004

[56] Poullet j.B., Sima D.M., Van Huffel S., *MRS signal quantitation: a review of time- and frequency-domain methods*, Journal of Magnetic Resonance 195:134-144, 2008

[57] De Beer R., *Quantitative in vivo NMR*, Tech. Rep. c59, Technische Universiteit Delft, 1994

[58] Stefan D., Di Cesare F., Andrasescu A., Popa E., Lazariev A., Vescovo E., Strbak O., Williams S., Starcuk Z., Cabanas M., Van Ormondt D. and Graveron-Demilly D., *Quantitation of magnetic resonance spectroscopy signals: the jMRUI software package*, Measurement Science and Technology 20:104035, 2009

[59] http://www.mrui.uab.es/mrui/mrui_homePage.shtml

[60] Pijnappel W.W.F., Van den Boogaart A., De Beer R. and Van Ormondt D., *SVD-based quantification of Magnetic Resonance signals*, Journal of Magnetic Resonance 97:122-134, 1992

[61] Vanhamme L., Van den Boogaart and Van Huffel S., *Improved method for accurate and efficient quantification of MRS data with use of prior knowledge*, Journal of Magnetic Resonance 129:35-43, 1997

[62] Dong Z. and Peterson B., *The rapid and automatic combination of proton MRSI data using multi-channel coils without water suppression*, Magnetic Resonance Imaging 25(8):1148-1154, 2007

[63] jMRUI-5.1 user help manual

[64] Ober R.J., *Achievable accuracy of parameter estimation for multidimensional NMR experiments*, Journal of Magnetic Resonance 157:1-16, 2002

[65] Barkhuijsen H., De Beer R. and Van Ormondt D., *Error theory for time-domain signal analysis with linear prediction and singular value decomposition*, Journal of Magnetic Resonance 67:371-375, 1986

[66] Cohen-Adad and Vheeler-Kingshott C., *Quantitative MRI of the spinal cord*, Academic Press, 2014

[67] Taylor J.R., *An introduction to error analysis. The study of uncertainties in physical environments- 2nd editions*, University science books, 1997

[68] Cabanes E., Confort-Gouny S., Le Fur Y., Simond G. and Cozzone P.J., *Optimization of residual water signal removal by HLSVD on simulated short echo time proton MR spectra of the human brain*, Journal of Magnetic Resonance 150:116-125, 2001

[69] Govindaraju V., Young K. and Maudsley A.A., *Proton NMR chemical shifts and coupling constants for brain metabolites*, NMR in biomedicine 13:129-153, 2000

[70] Ke Y., Cohen B.M., Lowen S., Hirashima F., Nassar L. and Renshaw P.F., *Bi-exponential transverse relaxation (T_2) of the proton MRS Creatine resonance in human brain*, Magnetic Resonance in Medicine 47:232-238, 2002

[71] Madan A., Ganji S.K., An Z., Choe Z.S., Pinho M.C., Bachoo R.M., Maher E.M. and Choi C., *Proton T_2 measurement and quantification of Lactate in brain tumors by MRS at 3 Tesla in vivo*, Magnetic Resonance in Medicine 00:00-00, 2014

[72] http://en.wikipedia.org/wiki/Density

[73] http://en.wikipedia.org/wiki/Molar_mass

[74] Malucelli E., Manners D.N., Testa C., Tonon C., Lodi R., Barbiroli B., and Iotti S., *Pitfalls and advantages of different strategies for the absolute quantification of N-acetyl aspartate, creatine and choline in white and grey matter by* ^{1}H-*MRS*, NMR in biomedicine 22:1003-1013, 2009

Ringraziamenti

Desidero ricordare tutti coloro che mi hanno aiutato nella stesura della tesi con suggerimenti, critiche ed osservazioni.

Ringrazio la Prof.ssa Fantazzini per aver condiviso con me la propria saggezza derivata da una solida esperienza nel campo NMR. La sua passione per la disciplina che ho visto durante le lezioni universitarie é stata presente anche nel periodo di tesi. Ringrazio la Dott.ssa Berardi per aver accompagnato e integrato il realizzarsi del progetto di tesi in maniera efficace. Ringrazio la Dott.ssa Fabbri per avermi seguito nel corso delle acquisizioni in RM, per avermi introdotto alle procedure sperimentali e per avermi sempre mostrato cortesia e disponibilitá.

Un sentito ringraziamento va anche al gruppo di ricerca della RM funzionale: al Prof. Lodi, alla Dott.ssa Testa, al Dott. Bianchini, al Dott. Manners e Stefania per avermi aiutato nello svolgimento della tesi e del progetto.

Ringrazio anche il mio caro "coinquilino" Leonardo per avermi aiutato sia praticamente che moralmente nel percorso della tesi. A lui auguro un brillante futuro. Un grazie anche a Filippo per averci letteralmente aperto la porta.

Ringrazio anche coloro che mi hanno aiutato nel mio percorso fino a qui: le maestre Emanuela, Maria Angiola, Paola (sempre ricordata con affetto), Rita Giovannini e in particolar modo Rita Marchi per la gentilezza, la sinceritá e il continuo supporto mostratomi durante gli anni. Un caloroso grazie va al mio stimato Prof. di Storia e Filosofia, Mario Davalle, per le motivanti parole condivise tramite il nostro "epistolario".

Ringrazio mia mamma per il suo cuore grande e forte, che mi ha consentito di mantenere la rotta anche nei momenti piú delicati. Ringrazio mio babbo per la tenacia e la costanza con la quale ha affrontato tutte le sfide della vita. Ringrazio mia sorella Bea per la sua straordinaria capacitá di portare avanti tanti sogni ed

essere sempre stata la mia piú grande ispirazione. Un grazie anche a Sofia e Milena per la gioia che avete portato nella nostra casa.

Un grazie gigantesco va anche a mia zia Marisa, mio zio Piero, mio zio Moreno e mia zia Mirella per avermi assistito in tantissimi momenti, per il supporto e l'aiuto inestimabili. Ringrazio anche mia nonna Flora, baluardo del Poggio, per l'incredibile forza d'animo.

Ringrazio anche tutti gli altri membri della mia famiglia: Davide, Valeria, Cristina, Daniele, Valentina, Lorenza, Barbara, Alessandro (Titti per capirci), Flavio, Alberto, Ginevra, Mia, zia Sara, zio Tarquinio, zio Sandro, zio Beppe, zia Franca (sempre ricordata con grande affetto), Piero, Anna, Tiziana, Alfiero, Graziana, Luciano, Simonetta, Laura, Bruna, Marco, zio Natale, zia Maria, Elisa, Serena, Daniela, Gianfranco, Daniele, Giuseppe, Aurora, Olga, Beppe, Marco, Massimo, Valerio, Alessandro, la mitica Elia, Maurizio, Mara, Manuela, Carla, Lorenzo, Daniele, Sara, Giampiero, Margherita. La lista potrebbe continuare all'infinito, ma diventerebbe un altro capitolo! Ringrazio tutti coloro che mi sono scordato.

Ringrazio i miei amici del liceo per gli steps back in time e le fatiche comuni su Seneca, Demostene et similia: Giulia, Attila, Eleonora, Dacia, Luca, la Tozzi, Cigno, la Marghe e gli altri miei compagni del Rambaldi.

Ringrazio i miei amici top, made in Firenzuola e dintorni: Chiara, Claudia, Nadia, Pascal, Macu, Valerio, Quercia e last, but not the least, la Cami.

Ringrazio le signore dell'ufficio PR di piazza D'Agnolo con annessa succursale di via Villani per la tifoseria: Betta, Paola, zia Gió, Claudina, Marzia, Manuela, Barbara, Caterina e Antonella. Un grazie speciale a Millo e Gino. Un mitico grazie anche alla zia di Monzuno, Marta.

Ringrazio gli amici della triennale: Alessando, Monti, Carlo, Fabio, Betta, Linda, Ivan, Enrico, Diego, Riccardo, Annalisa, Federica, Santiago, Samanta.

Ringrazio gli amici di Fisica applicata: Alice Z.B., Celeste, Mariagrazia, Arianna, Luigi, Marta, Diana, Samanta, Fosca, Laura, Riccardo, Francesca, Giulia, Manami, Valentina, Lorenzo, Luca "Boccio" e Luca "the mayor".

Un ricordo speciale va a Nonna Pellegra e zio Renato per il bene che mi hanno voluto.